CHARACTERISTICS AND ORIGIN OF AN EROSIONALLY RESISTANT UNIT IN THE MARS SCIENCE LABORATORY LANDING ELLIPSE (GALE CRATER, MARS), BASED ON ANALYSES OF SURFACE DATA AND ORBITAL IMAGES

A THESIS SUBMITTED TO THE GRADUATE DIVISION OF THE UNIVERSITY OF HAWAIʻI AT MĀNOA IN PARTIAL FULFILLMENT OF THE REQUIREMENTS FOR THE DEGREE OF

MASTER OF SCIENCE

IN

GEOLOGY AND GEOPHYSICS

MAY 2015

By

Samantha R. Jacob

Thesis Committee:

Scott Rowland, Chairperson
Sarah Fagents
Craig Glenn

Dedications

Along with all the ups and downs of graduate school, there are still all the ups and downs of life outside of school. Two of the greatest moments of my time in Hawaii were when I met Kristina Wynkoop Taylor and Haley Jayne Tyrrell. Two of the worst moments of my life were when I lost these two amazing friends. I first met Kristina in our undergraduate volcanology course. She was sitting in the front row of the classroom and there was one chair left next to her. From the moment I sat in that chair, Kristina and I were best friends. We spent the next year and a half doing homework, pulling all night lab sessions, and occasionally making it outside to soak up some sun. Sadly, 10 weeks before our graduation, Kristina passed away. It is because of her strength, desire to learn, and love of geology that I went forward and finished my undergraduate degree without her. Now as a graduate student with an office, I've hung several pictures of Kristina and I to help me remember the memories that we made and to hang on to her strength to keep going.

Kristina and I both had the honor of taking classes alongside Wendy Cockshell. Wendy is the mom of two young children, going back to school for her second bachelor degree. After finding out that I play piano, Wendy asked me to teach her children. Wendy's daughter Haley (10) needed physical and musical therapy and Zachary (9) needed an outlet for all of his crazy boy energy. Before I met Wendy and her family, Haley has diagnosed with childhood cancer. During the time I've known this incredible family, Haley had a brief few months of being cancer free. When it was discovered that Haley had relapsed Medullablastoma, we knew our time with her was getting short. Haley somehow found the strength to battle cancer for another two years; a strength that will always astound me. Every time I would come over for lessons, she always gave me a hug and her smile would melt away any worries that the day had brought. In the precious moments I had with Haley, she taught me so much about loving life and having the strength to move forward with a smile no matter what the circumstances are. This is a lesson that I have remembered during the hard times of graduate school. I will forever be grateful for the fun times I had with Haley. I know that Kristina and Haley are now using their beautiful angel wings to explore together.

Their lives were a blessing, their memories will be a treasure, they are loved beyond words and will be missed beyond measure!

Kristina Wynkoop-Taylor
Jan 15, 1985 - Feb 23, 2012

Haley Jayne Tyrrell
Oct 2, 2002 - July 8, 2014

Acknowledgements

As I walked across the stage at my undergraduate commencement ceremony, I never would have dreamt that I would be a part of the Mars Science Laboratory “Curiosity” science team. However, just three months later as I sat in my parent’s living room, holding my breath and watching Curiosity safely land in Gale Crater, I did so as part of the incredible team who would analyze the enormous amount of data that would soon come streaming down from Curiosity. I will forever be grateful for the opportunity to be at the forefront of Mars exploration.

There are far too many people to count who have made this thesis possible. However, there are a few people whose contributions were too great not to be personally recognized. To my family who listened to countless presentations, encouraged me during the hard times, and celebrated with me when my results finally came together, you are my lifeline. I would especially like to thank my sister/roommate Jessica, who listened to the most presentations and dealt with me during my best and worst moments. She put up with my alarm clock going off at 5am so I could participate in the tactical and science meetings. I’m sure there were times it was not easy for her to be so supportive, but yet she always was. She is my best friend and the most amazing sister ever! I would also like to thank my aunt Jacquie, who was the first one to critique my writing, including my college application letters, and helped mold me into the young scientist that I am today.

To my ohana here in Hawaii, I would like to say a kind aloha. In particular, my Asian sister Hannah, office-mate Maria, and office-neighbor Kendra, these amazing ladies/fellow scientists have all been incredibly supportive. They always made sure I had an endless supply of chocolate to get me through the frustrating times, laughed at me when I danced around the office after finishing my results, and learned to ignore me while I ranted to myself and my computer. They are truly some of the best friends I have ever had.

Last, but certainly not least, I would like to thank my fellow Curiosity science team members, especially John Grotzinger, Katie Stack, Kevin Lewis, Marisa Palucis, Ken Edgett,

Roger Wiens, Ryan Anderson, Lauren Edgar, Mackenzie Day, and Fred Calef. Through emails and teleconferences, these people and countless others taught me the necessary background that I was lacking and gave me kind criticism that ultimately strengthened my results. It has been a real pleasure to work alongside this incredible team. It is because of these people and so many others that I have grown from a geology student into a professional planetary geologist.

Abstract

The data coming from the multitude of orbiters and landed missions exploring the surface of Mars has proven that Mars had a very geologically active past. Almost every geologic process that is known to have occurred on Earth has also been identified in the deposits on the surface of Mars. The big picture scientists are now asking is, was Mars habitable? The Mars Science Laboratory (MSL) mission was sent to Gale Crater to investigate the answer to this resounding question. In August 2012, the MSL rover Curiosity safely landed in Gale Crater armed with the scientific instruments necessary to help verify whether or not Gale Crater could have ever hosted a habitable environment. Prior to landing, the Curiosity landing ellipse was mapped into six geomorphic units based on their geomorphic characteristics as seen in orbital images.

The goal of this research is to understand the extent and geologic origin of the Cratered Surface (CS), one of the six geomorphic units identified in the Curiosity landing ellipse. The CS is a nearly horizontal, erosionally resistant unit that covers ~24% of the surface within the landing ellipse. In HiRISE images, the CS exposures are identified by their high crater density and meter scale erosional scarps. Variations in morphological and topographical characteristics, and crater density of the CS exposures highlighted natural subdivisions. The five CS sub-units identified in this study are CS_Flat, CS_Infill1, CS_Infill2, CS_Bedded1, and CS_Bedded2.

Curiosity has imaged and analyzed four out of five sub-units with the Mastcam and ChemCam instruments, CS_Infill2 will not be visited by Curiosity. The various CS sub-units appear to be made of similar fine-grained, erosionally resistant material. Most of the CS float rocks chosen to be analyzed by the ChemCam instrument have grain sizes smaller than the resolution limit of the camera, which indicates that the grains are ~45 μm or smaller. The in situ outcrops of the CS sub-units have a range of lithologies, from massive to very fine bedding. Chemically, the CS targets show concentrations of Na, K, and Al indicative of an alkaline phase in the mineralogy of the CS.

The physical characteristics of the CS, as seen in the orbital HiRISE images and the Curiosity Mastcam images, are not distinct to one depositional environment. Additionally, the physical variations of the CS sub-units would suggest that there are multiple depositional environments represented by the CS exposures. The commonly observed erosional scarp and the ability to retain large numbers of sub-km craters indicate that the CS has either undergone lithification after deposition or is composed of an innately erosionally resistant material. Comparisons of the physical characteristics of the CS material to terrestrial outcrops have illuminated fluvial, lacustrine, aeolian, and volcanic flow processes that could have deposited the CS material. While a sedimentary origin is the most likely scenario, a volcanic origin cannot be conclusively ruled out. The geochemical signature of the CS material allow for the mineralogy and composition to be understood, however, it provides little support in narrowing down the possibilities of the geologic origin of the CS sub-units.

Table of Contents

List of Figures

List of Tables

List of Acronyms

AF	Alluvial Fan Unit
APXS	Alpha-Particle X-ray Spectrometer
BF	Bedded, Fractured Unit
CRISM	Compact Reconnaissance Imaging Spectrometer for Mars
CS	Cratered Surface
CTX	Context Camera
DEM	Digital Elevation Model
HiRISE	High Resolution Imaging Science Experiment
HP	Hummocky Plains Unit
HRSC	High Resolution Stereo Camera
LIBS	Laser-induced breakdown spectrometer
MAHLI	Mars Hand Lens Imager
MGS	Mars Global Surveyor
MOC	Mars Orbiter Camera
MOLA	Mars Orbiter Laser Altimeter
MRO	Mars Reconnaissance Orbiter
MSL	Mars Science Laboratory
ODY	Mars Odyssey
RMI	Remote-micro imager
RT	Rugged Unit
SR	Striated Unit
TES	Thermal Emission Spectrometer

THEMIS Thermal Emission Infrared Spectrometer

Chapter 1

Introduction

1.1 Thesis Objectives and Chapter Overview

This thesis focuses on the Cratered Surface (CS), which is a geomorphic unit found throughout the Curiosity landing ellipse. The primary goal is to describe its physical characteristics, as seen in both HiRISE and Curiosity images. Prior to landing in August, 2012 all heavily cratered terrain within the Curiosity landing ellipse was lumped into one geomorphic unit (i.e., the CS). However, there are subtle differences among the various CS exposures that have highlighted natural subdivisions of the CS. For this project, the CS has been divided into five sub-units. Indeed, there is no reason to expect all surfaces that preserve craters in the same way to necessarily consist of one rock type. Some of the characteristics used to subdivide the CS in the HiRISE images include albedo, surface roughness, crater density, and the erosional state of crater rims. The names given to the CS sub-units are based on the morphological and topographical expressions of the sub-units as seen in HiRISE images. The main goal of this thesis is to characterize the CS sub-units in terms of geomorphic properties, as seen in both HiRISE and Curiosity images.

The secondary objective of this thesis is to identify possible geological depositional environments for the origin of the CS sub-units. The geologic origin will be investigated by comparing the physical characteristics of the CS sub-units to terrestrial analogs. The last goal is to show how crater counting can be used as a mapping tool to understand the erosional history of various units in the Curiosity landing ellipse. Crater counts of the entire CS were compared to crater counts of the Hummocky Plains (HP) and Bedded, Fractured (BF) units to determine the erosional resistance and stratigraphic position of the CS as compared to other landing ellipse units. The crater counts of the various CS sub-units were

also compared as further evidence that the sub-units may represent different geologic environments.

This introduction chapter will discuss the history of the Martian surface and specifically the landing site of Curiosity, Gale Crater. Later there will be an introduction to the Mars Science Laboratory (MSL) mission and an overview of the instruments and datasets used in this project. Lastly, this chapter will present terrestrial analogs that will be discussed in chapter 3 as possible origins of the various CS sub-units. The second and third goal of this thesis will be thoroughly discussed in chapters 2 and 3.

1.2 Geologic Setting

1.2.1 Mars Global Topography

The most striking global topographic feature on the Martian surface is a sharp, physical geologic boundary between the southern highlands and northern plains (Fig. 1.1; Soderblom and Bell, 2008). This is known as the Martian crater dichotomy. The southern highlands are heavily cratered and host large impact basins and some of the oldest Martian terrains. The northern plains are topographically lower and younger than the southern highlands and consist of smooth volcanic and sedimentary terrains, as well as some of the well-known volcanoes on Mars including the Tharsis volcanic region and Olympus Mons (the tallest mountain in the solar system; Soderblom and Bell, 2008; Beyer et al., 2012). The origin of the dichotomy is still unknown. Since the development of the dichotomy, numerous erosional and depositional features have shaped the Martian surface. These features are evidence of volcanic, fluvial, lacustrine, glacial, and aeolian processes have occurred throughout Mars' geologic history.

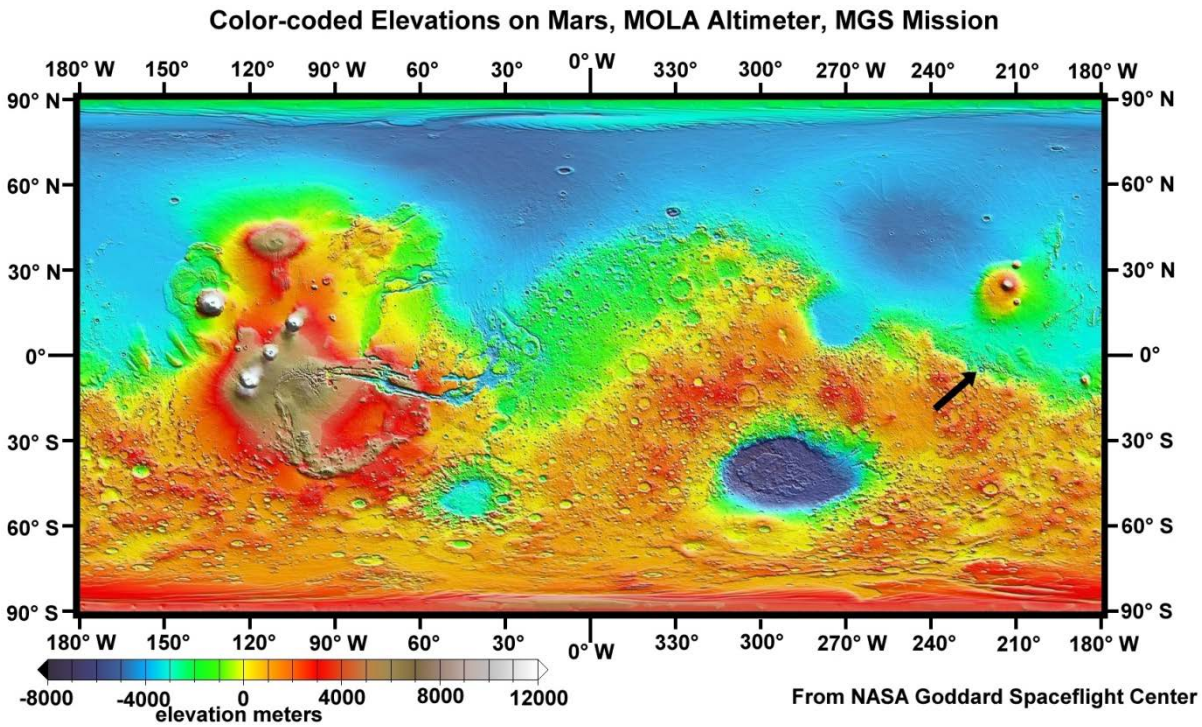

Figure 1.1: Global elevation map of Mars, using topographic data from the Mars Orbiter Laser Altimeter (MOLA; Smith et al., 1999). Black arrow shows the location of Gale Crater. Image from Anderson and Bell, 2010.

The present day surface of Mars has geologic evidence that liquid water once flowed across equatorial and mid-latitude areas. However, the polar regions are the only present day locations known to have perennial and seasonal liquid water (Malin and Edgett, 2000; Soderblom and Bell, 2008; Beyer et al., 2012; Grotzinger et al., 2014). The polar regions also have geologically young sequences of water ice, carbon dioxide ice, and dust that sit stratigraphically and topographically beneath the liquid water and carbon dioxide ice caps (Soderblom and Bell, 2008). Scott and Carr (1978) were the first to map the global distribution and sequence of the Martian geologic units. From this map, the Martian geologic timeline was defined (Fig. 1.2). From oldest to youngest the Mars' geologic periods are: Noachian, Hesperian, and Amazonian. Most of the units from the Noachian are located in the southern highlands. Hesperian units appear as small exposures, scattered along the margins of the Noachian and Amazonian units across the Martian surface. Lastly, the Amazonian units are primarily found in the lower northern plains, the Tharsis and Elysium volcanic plateaus, and the layered polar strata.

Figure 1.2: Martian geologic timeline with ages defined by (Hartmann and Neukum, 2001).

1.2.2 Sedimentary Rock Record of Early, Wet Mars

The idea that Mars could have a sedimentary rock record was first introduced by Carpenter (1948). Then, in the 1970s images from the Mariner 9 and Viking orbiters showed strong evidence for layered, potentially sedimentary, rocks on Mars (Blasius and Cutts, 1977; Grotzinger and Milliken, 2012). Sedimentary rocks are important because their composition and surface characteristics can help decipher variations in the climatic, tectonic, and biological environments of a planet. This is the main reason why space agencies around the world have spent the last 40 years exploring the surface of Mars. Since the 1970s, layered deposits have been found in numerous locations across the surface of Mars, with some deposits dating back to the Noachian (Malin and Edgett, 2000; Grotzinger and Milliken, 2012).

Viking images show cliffs of layered materials that weather without producing talus (Malin, 1976; Grotzinger and Milliken, 2012). This was the first observation made that indicated variations in the degree of lithification among the deposits on the surface of Mars. Indurated deposits typically form slopes of talus and float rocks as they weather. However, poorly lithified deposits weather into finer particles and do not produce slopes of talus. This observation therefore ruled out volcanic lava flows and ignimbrites as possible origins for the layered material (Grotzinger and Milliken, 2012). This was a turning point in the interpretations of these layered deposits; a sedimentary origin became less of a provocative idea and slowly became the consensus among the Mars science community. Mariner 9 and Viking images were used to identify the first channels and valley networks on Mars (Sharp and Malin, 1975; Grotzinger and Milliken, 2012). These hypotheses were later confirmed by images from the Mars Orbiter Camera (MOC) onboard the Mars Global Surveyor (MGS) and the High Resolution Imaging Science Experiment (HiRISE) onboard the Mars

Reconnaissance Orbiter (MRO). As the exploration of Mars continued and resolution improved, new fluvial features such as alluvial fans and deltas were identified on the surface. This added to the evidence that the geologic processes that occurred during the early history of Mars were much different than the processes occurring on the surface today (Moore and Howard, 2005; Wood, 2006; Grotzinger and Milliken, 2012).

The layered material found by Malin and Edgett (2000) are often at the base of stratified outcrops. These stratified outcrops have been divided into three units: layered, massive, and thin mesa. The units were divided based on albedo, thickness, texture, and configuration. The layered unit exposures have a medium to high albedo and range from a few meters to 2000 m in thickness. Within the layered deposits, there can be one to hundreds of thin, tabular beds (Malin and Edgett, 2000). The massive unit exposures also have a medium to high albedo, but are thicker than the layered unit. The massive unit thickness ranges from 100s of meters to a few kilometers. The base of the massive unit is a transition zone between the layered and massive units. Here, the massive unit has poor bedding, whereas the rest of the massive unit does not typically display bedding. Lastly, the thin mesa unit typically has a low albedo. This unit consists of resistant caprock-forming material.

All three units are interpreted to be fine grained, indurated, sedimentary rock (Malin and Edgett, 2000). The evidence for fine grained texture comes from how the units erode. The lack of boulders at the base of escarpments formed by the units suggests that the units eroded into smaller clasts and individual grains. The presence of yardangs also confirms that the units are fine grained and well indurated. Both the fine grained texture and the indurated nature of these units are strong indicators for a sedimentary depositional environment. A pyroclastic origin has been ruled out mainly due to the thickness of the units. Pyroclastic air fall deposits that are meters to kilometers thick, similar to the stratified outcrops, are only found within a few hundred meters of the source vent. Therefore, if these outcrops were pyroclastic fall deposits, Mars would have had to produce explosive volcanic eruptions with volumes greater than has been seen on Earth, and yet not retained any evidence of the source vent (Malin and Edgett, 2000).

Whereas these stratified outcrops are found throughout the surface of Mars, there is substantial variation among the different exposures of each unit. Additionally, there is no reason to assume that these stratified outcrops are laterally or stratigraphically continuous across the entire equatorial region of Mars. Whereas the origin of the units was relatively easy to determine, the ages of these units are not. Some of the stratified outcrops have few to no impact craters, thus making it hard to determine age from traditional crater counting techniques. However, based on the geologic context and stratigraphic placement of a stratified outcrop in Valles Marineris, a Noachian age has been applied to all layered and massive units of the stratified outcrops. There appears to be a time lag between the deposition of the massive and thin mesa unit. The thin mesa unit is always found sitting unconformably on the massive or layered units (Malin and Edgett, 2000). It is not yet understood how much time passed before the deposition of the thin mesa unit.

1.2.3 Gale Crater and Mt. Sharp

Gale Crater (Fig. 1.3) has a diameter of 154 km and is located at 5.3°S, 222.3°W, on the margin of the Martian crater dichotomy. The northern rim of Gale Crater sits ~2 km lower than the southern rim. The highest point on the crater rim is 1448 m (Anderson and Bell, 2010). The deepest point in Gale Crater is -4400 m. The northern portion of the crater rim sits ~2 km above the northern crater floor, whereas the southern crater rim sits 3 – 4 km above the southern crater floor. The topographic relationships of the northern and southern portions of Gale Crater rim are the result of two different events in Gale Crater's history. One, whereas the regional slope of the Martian crater dichotomy is thought to be partially responsible for the elevation differences of Gale Crater's rim, it is possible that differential erosion has affected the northern crater rim much more than the southern rim (Pelkey and Jakosky, 2002; Anderson and Bell, 2010). The second possibility is the deposition of more sediment onto the northern crater floor relative to the southern crater floor (Anderson and Bell, 2010).

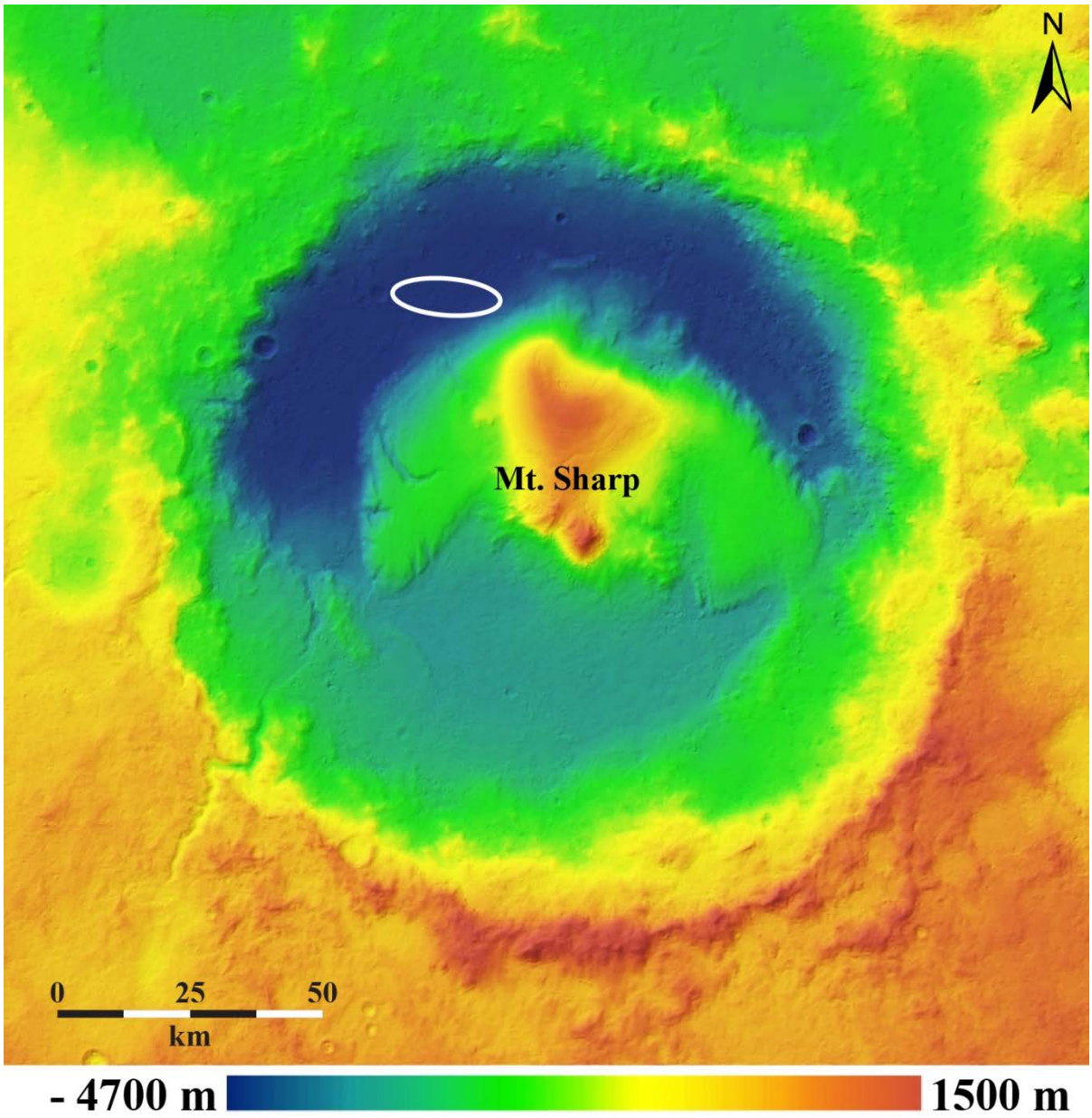

Figure 1.3: Elevation map of Gale Crater based on topographic data from the High Resolution Stereo Camera (HRSC). White ellipse is the final Curiosity landing ellipse.

The ultimate destination of the MSL mission is Aeolis Mons, known informally and now popularly as Mt. Sharp (named in honor of the pioneering planetary scientist Robert Sharp). Mt. Sharp rises 5.2 km above the crater floor and has numerous geologic features such as erosion-resistant ridges, layered deposits, and a large erosional unconformity (Malin and Edgett, 2000; Anderson and Bell, 2010). The peak of Mt. Sharp is topographically higher

than the northern rim of Gale Crater and slightly lower than the southern rim. CRISM data detected the presence of Fe-rich smectites and sulfate minerals interbedded in the lower layers of Mt. Sharp. The erosional unconformity divides the lower and upper sections of Mt. Sharp. The mineralogy of the upper layers is hard to determine because of the thick dust cover and incomplete CRISM data. The variations in the mineralogy of the Mt. Sharp layers indicate changes in depositional and environmental conditions and the possibility of liquid water in the geologic history of Gale Crater (Milliken et al., 2009).

Gale Crater has sparked the interest of many planetary scientists over the past several decades. Scott et al. (1978) first used Viking images to map the material in Gale Crater and interpreted the units to have a volcanic and aeolian origin. A fluvial origin for the units in Gale Crater first came from Greeley and Guest (1987) who interpreted the Gale Crater units as volcanic, aeolian, or fluvial in nature. Cabrol et al. (1999) used Viking images and early data from the Mars Orbiter Laser Altimeter (MOLA) to interpret the units as the result of hydrothermal activity in Gale Crater. Pelkey and Jakosky (2002) used MOLA, Thermal Emission Spectrometer (TES), Viking, and MOC data to conclude that the floor of Gale Crater is likely the result of multiple processes and that aeolian processes have been very important in shaping the surface into what we see today. Analyses of the TES and THEMIS data have determined that the dunes surrounding Mt. Sharp have a composition similar to olivine basalt (Hamilton et al., 2007; Rogers and Bandfield, 2009). Analyses of OMEGA and CRISM data by Milliken et al. (2009) confirmed the presence of olivine and pyroxene in the aeolian dunes. The terrain within the Curiosity landing ellipse has a composition that represents a mixture of olivine basalt and martian surface dust (Rogers and Bandfield, 2009).

Gale Crater has been identified by Malin and Edgett (2000) as a member of a family of craters that were once completely filled with sedimentary material. Malin and Edgett (2000) found numerous occurrences of layered, sedimentary rock located in large (~150 km diameter) craters throughout the equatorial regions of Mars. These craters appear to represent different stages of exhumation and erosion, from completely filled to almost completely exhumed (Fig. 1.4). Craters in the early stage of exhumation have an erosional moat just inside of the crater wall. It appears that as exhumation progresses, the moat gets

wider at the expense of the crater fill material, until all that is left is a mound of the original infill material (e.g. Mt. Sharp). The process by which the exhumation occurs and the material is removed from the crater is not yet understood, Malin and Edgett (2000) suggested that it may no longer occur on Mars. Gale Crater has experienced enough exhumation to form an isolated mound of material (i.e. Mt. Sharp), but has not experienced total erosion of the infilling material.

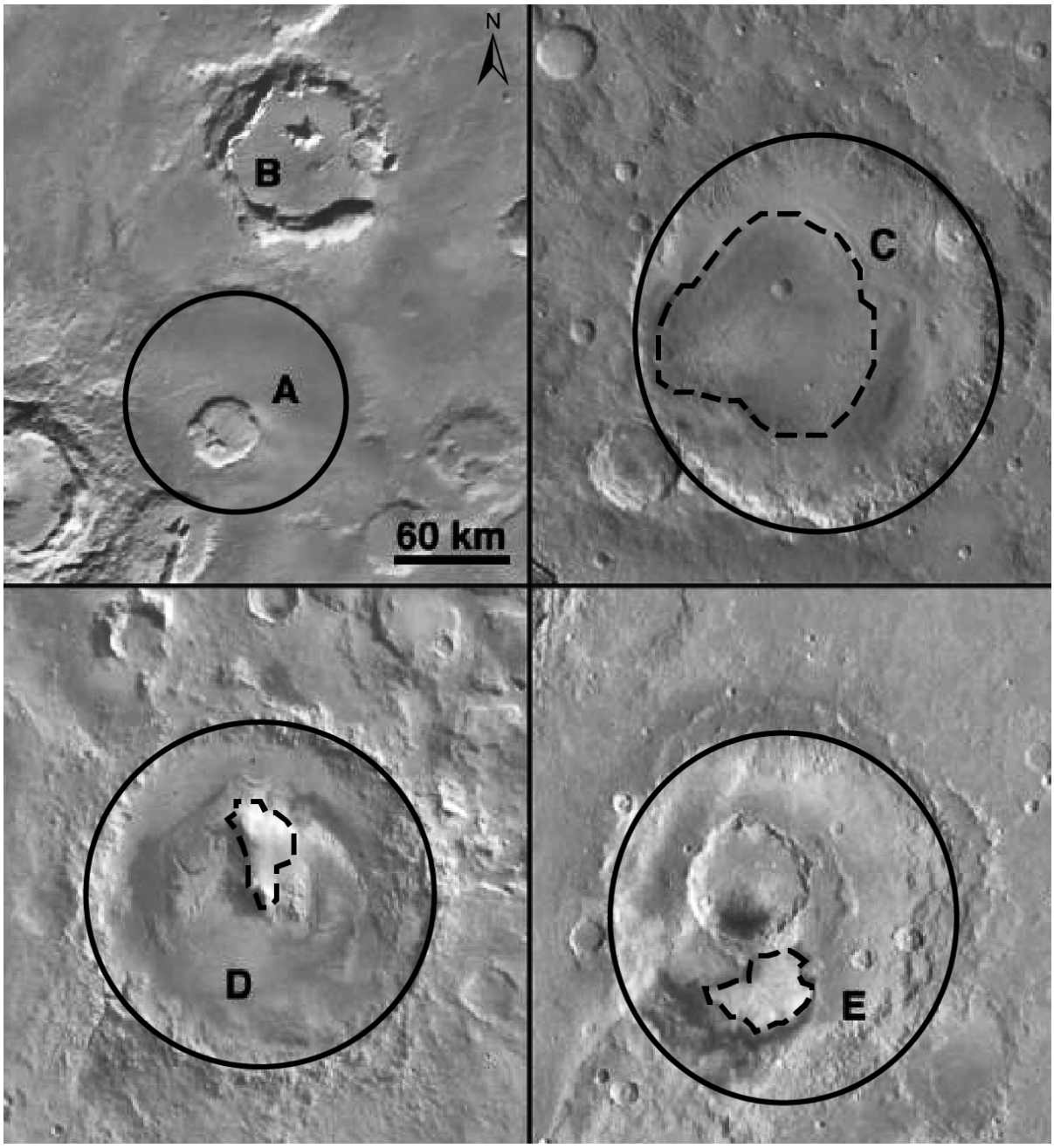

Figure 1.4: Craters (solid black circles) showing different stages of exhumation. Images are subsections of U.S. Geological Survey Viking orbiter image mosaics. A) An unnamed, filled crater. B) An unnamed crater showing the initial stages of exhumation. Erosion has created a moat just inside of the crater wall. C) Henry Crater and D) Gale Crater show the intermediate stages of exhumation. As erosion continued the layered material forms an isolated mound (dashed black lines) of material near the center of the crater. E) Becquerel Crater shows the end stages of the exhumation process. All that remains is a small, isolated mound of the layered material [Modified from Malin and Edgett, 2000 figure 11].

Assuming the hypothesis of Malin and Edgett (2000) is correct for Gale Crater, Mt. Sharp is an erosional remnant of sediment that once completely filled the crater. The majority of the sediment would have originated outside of Gale Crater and been deposited onto the crater floor under subaerial or subaqueous conditions. This hypothesis requires that the depositional environment be able to mobilize massive amounts of sediment and operate over extensive timespans in order to completely fill Gale Crater (Malin and Edgett, 2000). Possible depositional environments that are consistent with this hypothesis include evaporitic, lacustrine, deltaic, and aeolian.

An alternative hypothesis to the formation of Mt. Sharp is that it originated from material already inside Gale Crater and is a depositional feature. Work done by Kite et al. (2013) shows that the orientation of the Mt. Sharp layers is consistent with a predominantly aeolian depositional environment and limited fluvial activity. Measurements of the Mt. Sharp layers show that they dip away from the center of Mt. Sharp, which is inconsistent with most fluvial depositional environments (Kite et al., 2013).

While Mt. Sharp is the ultimate destination for Curiosity, there are many other geologically interesting features in Gale Crater that Curiosity will investigate along its traverse. These features suggest that Gale Crater had a very geologically active past and although the environment has changed, is still geologically active. Using topographic and visible data many channels and sinuous ridges have been identified breaching the crater rim (Fig. 1.5; Anderson and Bell, 2010). The largest channel breaches the southwestern rim and the valley extends for ~40 km across the western crater floor. Another distinct channel breaches the northern portion of the crater rim and culminates in the Peace Vallis fan complex in the NW portion of the Curiosity landing ellipse. These channel networks and fans suggest that an extensive fluvial drainage environment was active in Gale Crater's past (Anderson and Bell, 2010; Palucis et al., 2014). Farther to the south near the center of Gale Crater is an extensive sheet of dark-toned aeolian sand dunes (Fig. 1.6; Anderson and Bell, 2010; Minitti et al., 2013). Orbital images have proven that these dunes are active (Hobbs et al., 2010; Minitti et al., 2013) and suggest an active aeolian environment in Gale Crater. The dunes are currently being deposited up the slopes of Mt. Sharp.

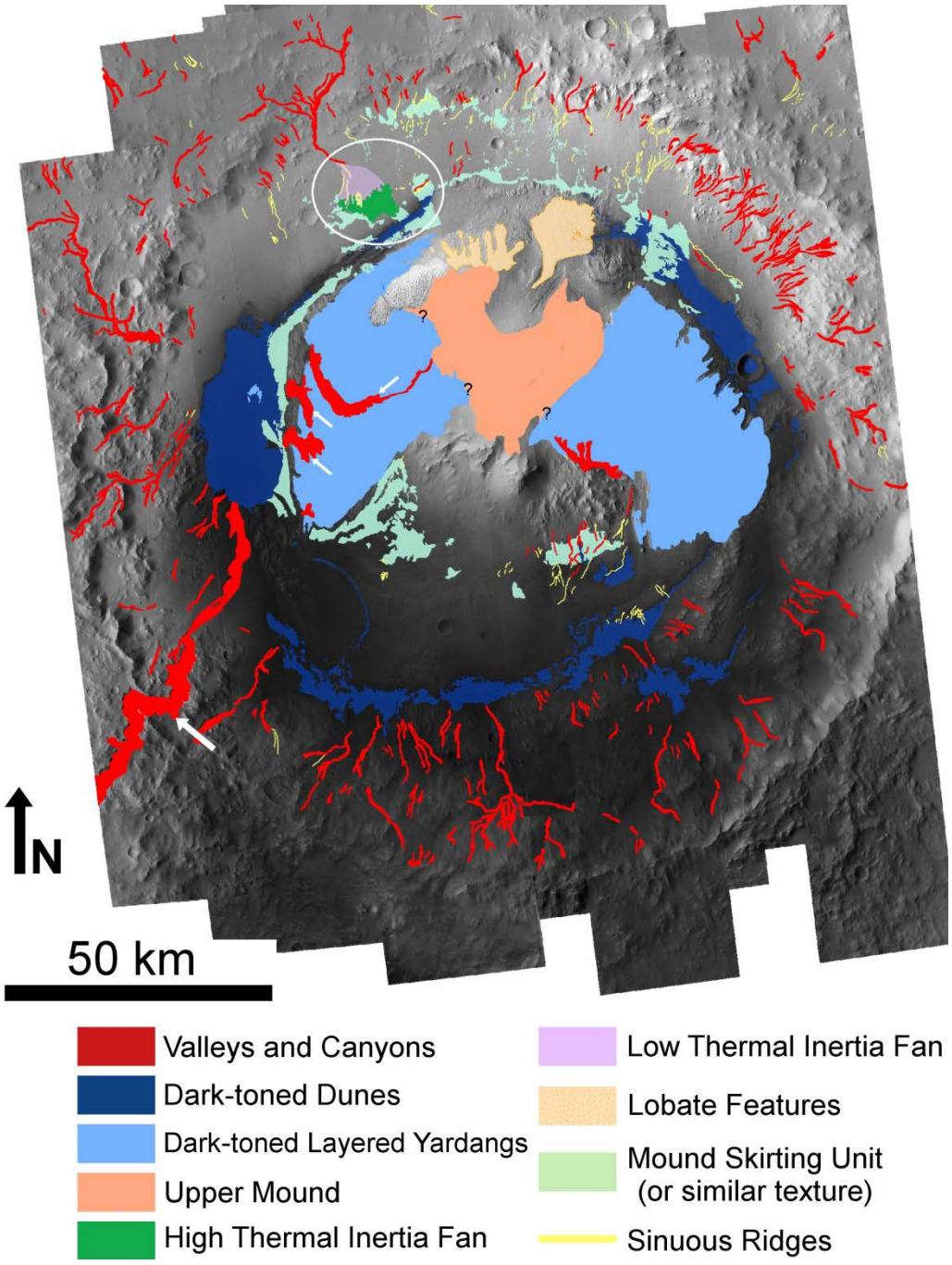

Figure 1.5: Map of surface units and features of Gale Crater, based on analysis of HiRISE, CTX, MOC, thermal inertia data from THEMIS and infrared data from CRISM and OMEGA. The Curiosity landing ellipse is outlined by the white oval. Located within the white oval are the geomorphic fan deposits, mapped in purple and green. The dark sand dunes are shown in dark blue. Note the landing ellipse shown here is larger than the final MSL landing ellipse shown in figures 1.3 and 1.6. [Modified from Anderson and Bell, 2010 figure 7].

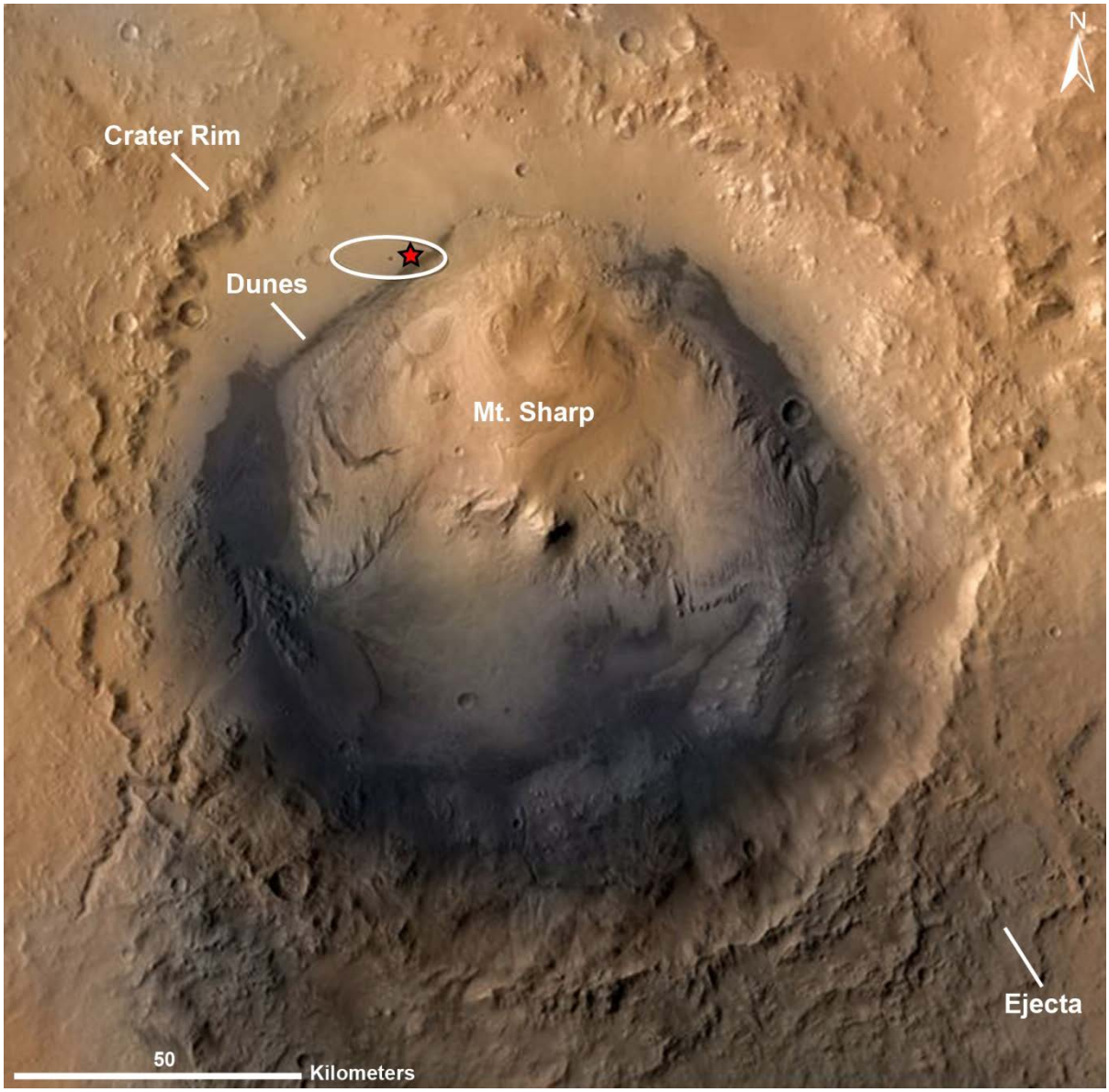

Figure 1.6: This image of Gale Crater is composed of 3D topographic data from the HRSC on the European Space Agency's Mars Express orbiter, panchromatic image data from the CTX, and color information from Viking Orbiter images. Gale Crater is 154 km in diameter and is the landing site for the MSL mission. The red star indicates the Curiosity landing site. The landing ellipse (white ellipse) is 20 km long by 7 km wide.

Before landing, the landing ellipse was divided into 140, 1.2 km x 1.2 km quadrants, of which 104 were mapped by many contributing scientists. The mapped quadrants were compiled into a single map consisting of six geomorphic units (Figs. 1.7 and 1.8; Grotzinger et al., 2014). The map consists of the Alluvial Fan (AF) Unit, Bedded Fractured (BF) Unit,

Cratered Surface (CS) Unit, Hummocky Plains (HP) Unit, Rugged (RT) Unit, and the Striated (SR) Unit. As their names imply, the units were mapped and named almost exclusively because of their textural and albedo characteristics. The AF unit, characterized by smooth, mottled surfaces, is the upper unit of the Peace Vallis alluvial fan (Sumner et al., 2013). The BF unit is distinguished by its relatively high albedo and by the occurrence of numerous fractures that vary in length and spacing distance (Rice et al., 2013). The CS has a high crater density and is relatively planar. The HP unit has a uniform surface roughness and a uniform albedo. The RT unit has a rough surface texture and variable relief. Lastly, the SR unit is light-toned with striations that trend northeast to southwest (Rice et al., 2013). Note that the outcrops of the SR unit, located in the southern portion of the landing ellipse, are so limited that they are not easily visible at the scale of figure 1.7.

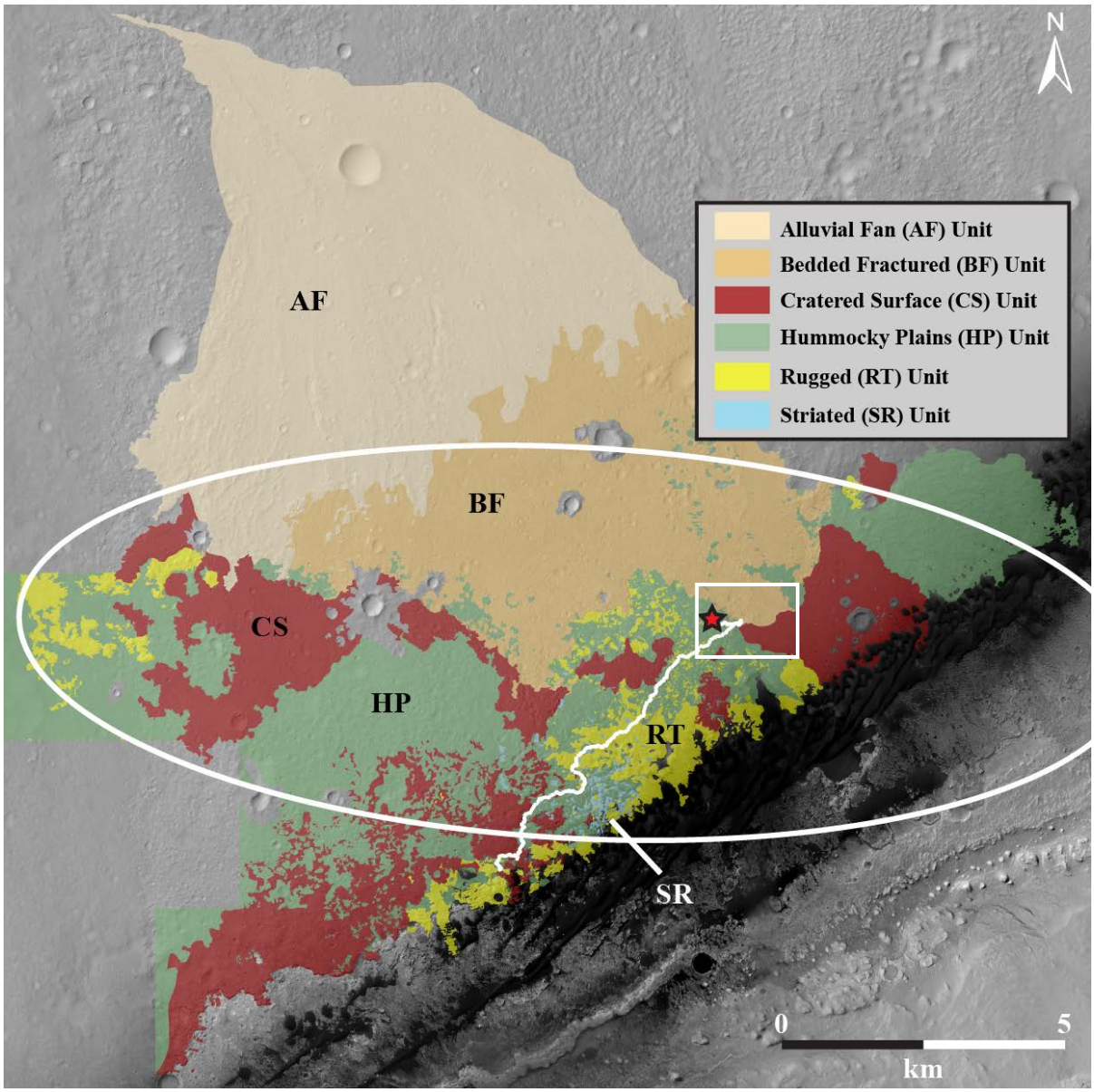

Figure 1.7: Geomorphic map of the Curiosity landing ellipse (white oval). Red outlined star indicates the actual landing location. The white rectangle shows the location of figure 1.8.

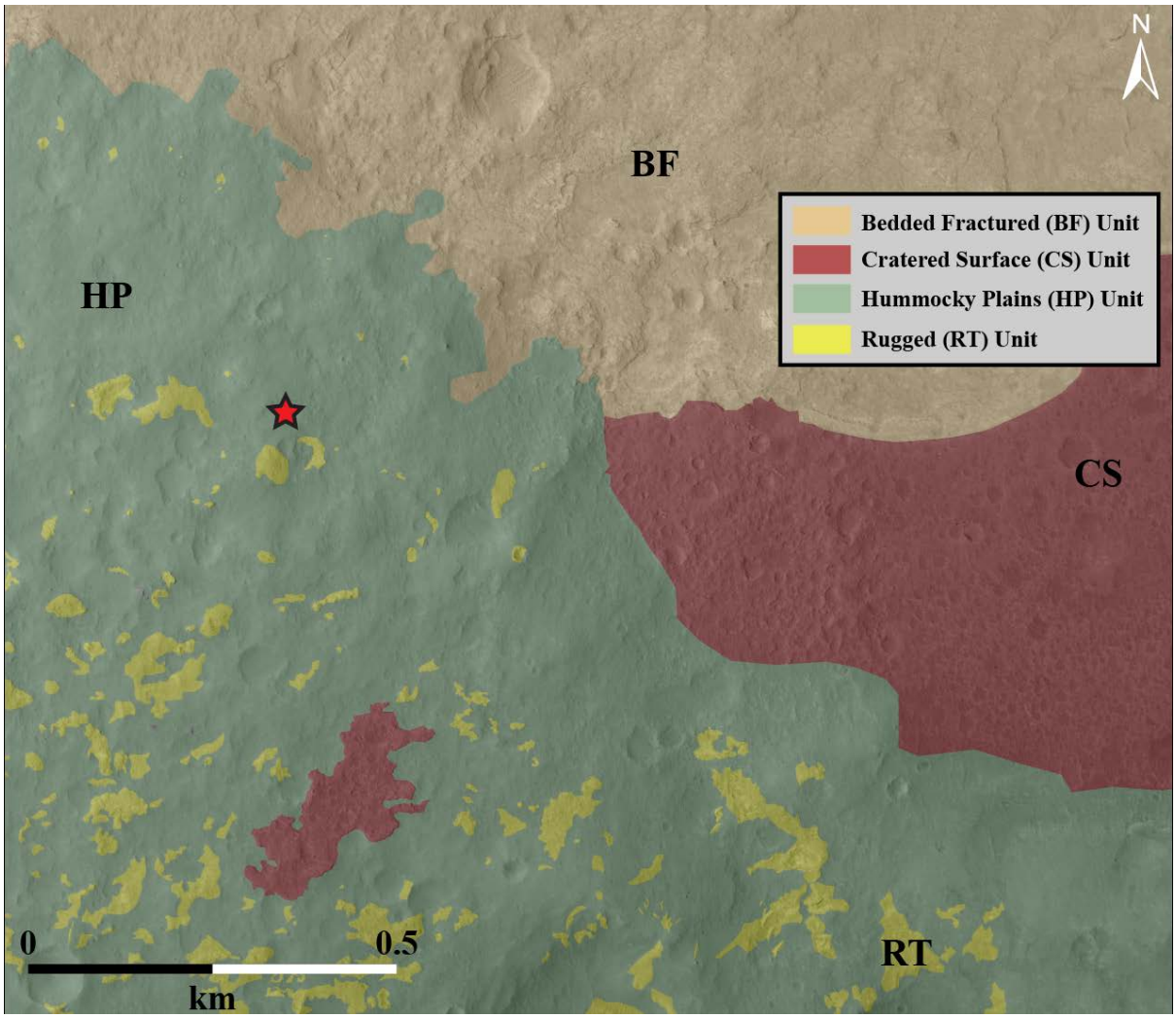

Figure 1.8: A portion of the map from figure 1.7 showing the physical characteristics that were used to define the CS, BF, RT, and HP units.

1.3 MSL Mission Overview and Objectives

In August 2012, the MSL rover, Curiosity, landed in Gale Crater in the northwest section of the moat that isolates Mt. Sharp from the crater rim (Fig. 1.3 and 1.6). The primary goal of the mission is to quantitatively assess the local Martian surface for the presence of what could have been habitable conditions in the past. Curiosity is studying ancient environments recorded in Gale Crater sediments (Grotzinger et al., 2012), as well as the modern environment for when NASA sends astronauts to Mars. If the stratified outcrops identified in orbital images do represent sedimentary processes, it is possible these outcrops have the right

combination of requirements necessary to show Mars once had a habitable environment. A big picture question scientists hope to answer using stratified outcrops, such as those identified in Mt. Sharp, is, whether or not Mars could have been habitable. Requirements for a habitable environment include liquid water, a source of energy, and elements such as carbon, hydrogen, sulfur, nitrogen, and phosphorous (Grotzinger et al., 2014). Because previous orbital and landed missions have found evidence for liquid water, Curiosity was built with the intent to search for the other requirements of a habitable Martian environment (Rice et al., 2010). Curiosity will search for elements such as carbon, hydrogen, and sulfur in order to validate the possibility of a Martian biosphere.

The primary mission of MSL had a duration of one Mars year (~23 Earth months). The Curiosity rover has a payload of 10 science instruments that together will assess the composition and geologic setting of the rocks, atmosphere, and radiation environment in Gale Crater. The rover is powered by a Multi-Mission Radioisotope Thermoelectric Generator. The primary communication network for data downlink is a relay system from Earth through the Mars Reconnaissance Orbiter (MRO) and Odyssey (ODY) spacecraft to the Curiosity rover (Grotzinger et al., 2012). Image data from these spacecraft, which have been orbiting Mars since 2006 (MRO) and 2002 (ODY) were indispensible for deciding on Gale Crater as the landing site (Saunders et al., 2004; Zurek and Smrekar, 2007). Gale Crater was chosen because of its geologic diversity and potential to record evidence of past habitable environments (Anderson and Bell, 2010; Grotzinger et al., 2012). The ultimate destination for Curiosity is the lower layers of Mt. Sharp, where the geomorphology and mineralogy are good indicators of fluvial deposition and could preserve evidence of past potentially habitable environments (Anderson and Bell, 2010; Milliken et al., 2010).

1.3.1 Overview of the Curiosity Rover

The Curiosity rover was built as a mobile geologic laboratory to explore the Martian geosphere, atmosphere, and potential ancient biosphere. Curiosity has a mass of 899.2 kg (equivalent to a weight of ~1 ton on Earth), with the scientific payload taking up ~8% of that weight (Grotzinger et al., 2012). The 10 science instruments weigh 75 kg (~165 lbs.). The

instruments on Curiosity (Fig. 1.9) are the Alpha-Particle X-ray Spectrometer (APXS), Laser-Induced Remote Sensing for Chemistry (ChemCam), Chemistry and Mineralogy (CheMin), Dynamic Albedo of Neutrons (DAN), Mars Hand Lens Imager (MAHLI), Mars Descent Imager (MARDI), Mast Camera (MastCam), Radiation Assessment Detector (RAD), Rover Environmental Monitoring Station (REMS), and the Sample Analysis at Mars Instrument Suite (SAM). The CheMin, DAN, MARDI, RAD, and SAM instruments are located in the body of the rover, which has a width of 2.8 m and a length of 3 m. Other instruments including ChemCam, Mastcam, and REMS are located on the rover's remote sensing mast (RSM). The rover has a total height of 2.2 m, the wheels and body of the rover have a combined height of 1.1 m and the RSM adds an additional 1.1 m (Grotzinger et al., 2012). The rover also has a robotic arm that can be extended almost 2 m form the rover body. At the end of the robotic arm is a rotating turret which houses the APXS and MAHLI instruments as well as the dust removal tool (DRT; a stainless steel wire brush), a drill, and a scoop (Edgett et al., 2012; Grotzinger et al., 2012). In the following paragraphs I describe in more detail those instruments (MAHLI, Mastcam, and ChemCam) which collected the data used in this study.

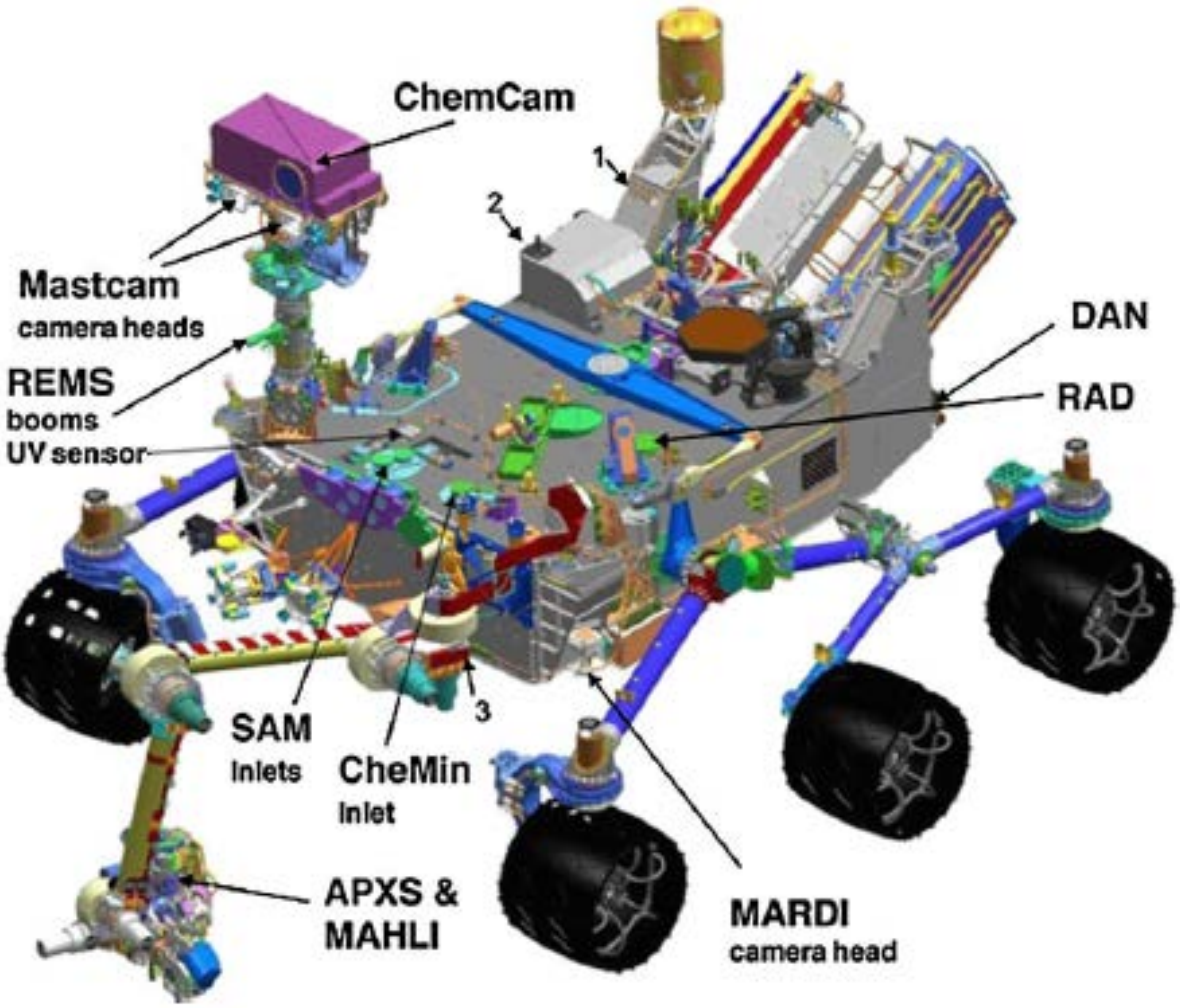

Figure 1.9: Diagram showing the location of the scientific instruments onboard the Curiosity rover (Grotzinger et al., 2012).

1.3.2 MAHLI

MAHLI consists of a 2-megapixel, macro-lens camera that collects images with a spatial resolution as high as ~14 μm in visible and UV wavelengths (Fig. 1.10; Ghaemi, 2009; Edgett et al., 2012; Grotzinger et al., 2012). MAHLI can be manually focused or the autofocus feature can be enabled to capture focused images from as close as 2.1 cm out to infinity. The instrument includes a dust cover that protects the camera lens from accumulating dust and is opened when images are taken. Being that MAHLI is located at the end of Curiosity's robotic arm allows it to be placed as close as 2 cm from an outcrop (Edgett, 2012). At each distance and focus, a single MAHLI image will have areas that are

out of focus. To acquire an image of a distant target that is entirely in focus requires a z-stack. A z-stack is a merge product of multiple MAHLI images taken of the same target focused at different distances. The final product is an image of the target that is completely in focus at all distances. MAHLI is also equipped with UV LEDs that enable the search for fluorescent or phosphorescent material. MAHLI has been used for grain size analysis, documentation of fine scale outcrop characteristics, and quality control checks of other rover instruments.

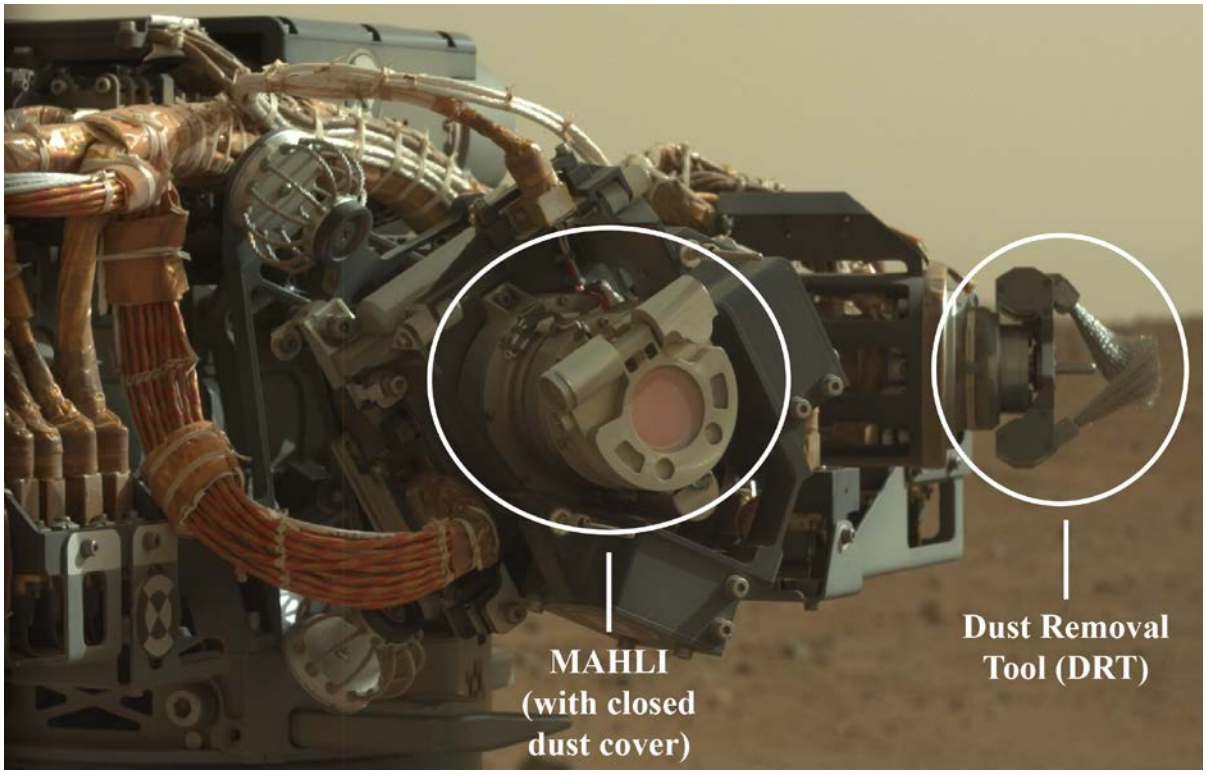

Figure 1.10: Mastcam (M-34) image of the Mars Hand Lens Imager (MAHLI) camera taken on sol 30. The pink circle in the image has a diameter of ~30 mm.

1.3.3 Mastcam

Mastcam (Fig. 1.11) consists of two cameras mounted on the RSM ~20 cm apart. The camera on the left side (M-34; with a focal length of 34 mm) has a focal distance from 0.34 m to infinity. The camera on the right side (M-100; with a focal length of 100 mm) has a focal distance of 1.63 m to infinity. At a distance of 2 m from a target, the M-34 camera has a pixel scale of 450 µm. At the same distance, the M-100 camera has a pixel size of 150 µm

(Grotzinger et al., 2012). Each camera can acquire images and video as fast as 8 frames/second. Both cameras can acquire natural color RGB images, using a Bayer Pattern Filter. Mastcam has the ability to acquire stereo (3D) images and 360° color mosaics. The main purpose of Mastcam is to characterize the geologic formations in Gale Crater that will help decipher the geologic history of the area. Other uses for the camera are capturing video of atmospheric and meteorological events and to help in rover operations, sample documentation, and contact science activities (Grotzinger et al., 2012).

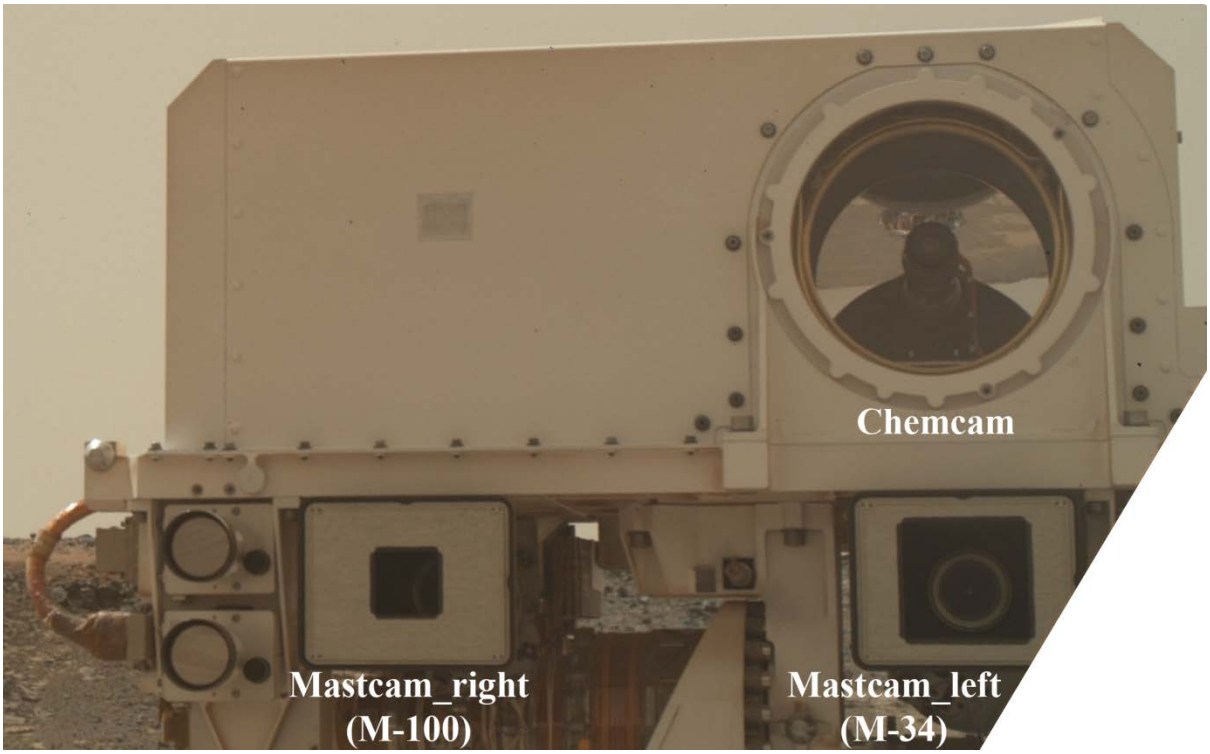

Figure 1.11: Portion of the latest MAHLI rover selfie, taken on sol 868, showing the Mastcam and ChemCam instruments. The ChemCam lens is 20 cm.

1.3.4 ChemCam

The ChemCam instrument (Fig. 1.11) has two components, a laser-induced breakdown spectrometer (LIBS) and a remote micro-imager (RMI). This is the first LIBS to be flown on a planetary mission (Wiens et al., 2012). The purpose of the LIBS is to determine the elemental composition of rock and soil targets as far as 7 m from the rover. The LIBS shoots a pulsed laser at the rock target and ablates small spots (350 – 550 μm) into the rock. The

interaction of the LIBS laser and the target produces a plasma spark. The light produced by the plasma is collected by three spectrometers within the instrument (Wiens et al., 2012; Anderson et al., 2014). A LIBS observation on a rock target involves firing the laser at multiple closely-spaced locations on the same target, either in a grid pattern or along a line transect. Each location in an observation receives a minimum of 30 laser pulses, every laser pulse produces a spectrum, which can be examined individually or averaged. The first few laser pulses analyze the surface dust, and the shock wave from the plasma spark clears the dust away, so that the remaining pulses analyze the composition of the rock itself.

ChemCam's RMI is used to document the location of the LIBS laser pulses on the chosen target, RMI images are always taken before and after the LIBS is fired (Anderson et al., 2014). This helps to verify whether the LIBS shot the intended target and help determine if individual crystal grains or clasts were analyzed in a ChemCam LIBS observation. The RMI also provides information about a target's texture and can be used as a telephoto imager on its own (i.e., without an accompanying LIBS measurement). The RMI can be focused at infinity to image distant landscape. Multiple images of the same target taken at different focus settings can be merged to produce a RMI z-stack (Anderson et al., 2014; Le Mouélic et al., 2014). The z-stacks can help understand the micro-topography of nearby targets.

1.4 Overview of Orbiter Instruments

1.4.1 HiRISE

The cameras onboard Curiosity are the latest addition to an extensive suite of cameras imaging the Martian surface. The Martian surface, including Gale Crater, has already been extensively mapped using cameras onboard orbiting spacecraft. Orbital images allow the locations of Curiosity's surface images to be put into geological context. Images from the High Resolution Imaging Science Experiment (HiRISE; McEwen et al., 2007) onboard the Mars Reconnaissance Orbiter (MRO) were the main source of orbital data for this thesis. HiRISE provides the highest resolution satellite images available for the surface of Mars, with a spatial resolution of 0.25 - 0.32 m/pixel (McEwen et al., 2007). HiRISE can acquire

images in visible to near-infrared wavelengths. One of the main objectives of the HiRISE project is to acquire stereo images, from which DEMs can be derived (McEwen et al., 2007). Orbital images provide an extensive regional overview of the geology, by combining orbital and surface images, surface textures can be correlated to regional geologic differences identified in orbital images. Locations that are covered by both orbital and surface images can be used as reference points for use throughout the study location. These reference points are especially useful to help map the geology of areas that Curiosity will not be able to visit.

1.4.2 THEMIS

The Thermal Emission Imaging System (THEMIS) onboard the 2001 Mars Odyssey orbiter was built to study the mineralogy and physical properties of the units on Mars by taking multi-spectral thermal infrared images of the surface (Christensen et al., 2004). The goal of the THEMIS mission is to map the entire planet in both day and night settings with a 100 m/pixel resolution. THEMIS also has the ability to map portions of the surface at 18 m/pixel resolution. THEMIS was specifically built to identify the spectra of key aqueous minerals such as carbonates and hydrothermal silica (Christensen et al., 2004). Data from THEMIS were used to make the geomorphic map of Gale Crater.

1.4.3 CTX

The primary goals of the Context Camera (CTX) onboard the Mars Reconnaissance Orbiter (MRO) is to provide context images for the other instruments onboard MRO, observe possible landing sites for surface missions, and to investigate geologic, geomorphic, and meteorological processes on Mars (Malin et al., 2007). The CTX can take image swaths of the Martian surface that are ~30 km wide and ~40 km long, with a resolution of 5 - 6.5 m/pixel. CTX images were compiled into a mosaic, and distributed to the MSL team members, as part of the basemap used while mapping the Curiosity landing ellipse.

1.5 ArcGIS Methods

The orbital mapping, crater counting, and thickness measurements were conducted using ArcGIS 10. Multiple datasets, including a Digital Elevation Model (DEM) and HiRISE image mosaics were used to visualize the boundaries of the geomorphic units. The DEM, basemap, and HiRISE mosaics were provided to the MSL team by the Jet Propulsion Laboratory (JPL). The basemap of Gale Crater utilized in this study is a combination of twelve 0.25 cm/pixel HiRISE stereo pairs (created by the U.S. Geological Survey Astrogeology Center in Flagstaff), three CTX 6 m/pixel stereo pairs, and a 50 m/pixel DEM made from the Mars Express High Resolution Stereo Camera (HRSC; Calef et al., 2013; Golombek et al., 2012; Palucis et al., 2014). These three datasets were georeferenced to make a "resolution pyramid" used by all of the MSL team members to map Gale Crater. From this "resolution pyramid" of datasets, MSL team members could extract 0.25 cm/pixel HiRISE visible, 1 m/pixel elevation, and 100 m/pixel thermal inertia data.

Polygon shapefiles were made to trace the boundaries of the CS sub-unit exposures. The geologic unit shapefiles from Grotzinger et al. (2014) were modified to define the boundaries of the landing ellipse units used in this study. This resulted in subtle differences in the surface area of the geologic units between figure 1B in (Grotzinger et al., 2014) and figure 1.7 of this study.

Topographic profiles were made after the map was completed, using the 3D Analyst tool in ArcGIS. The positions of the profiles were saved in a polyline shapefile. Twenty profiles were measured along the boundary of all the large exposures of all five CS sub-units. These profiles were saved as jpeg images and brought into Adobe Illustrator to calculate the thickness of the CS sub-unit. The profiles were also used to help determine the regional geologic context of the CS sub-units.

1.6 Terrestrial Analogs of the Cratered Surface

The terrestrial analogs to which the CS exposures will be compared are described below. After the CS exposures have been described in chapter 2, the physical characteristics of the CS deposits will be compared to the deposits of the terrestrial processes described below.

1.6.1 Pāhoehoe Lava Flows

Typical Hawaiian pāhoehoe lava flows are characterized by a planar, hummocky surface. The flows tend to be laterally extensive, that typically start as 20 – 30 cm thick and can inflate to a thickness of several meters (Hon et al., 1994a; Self et al., 1998). The thin initial flows are the result of the low viscosity of Hawaiian pāhoehoe lava flows. Inflation typically occurs uniformly throughout the entire pāhoehoe sheet (Hon et al., 1994b). However, sometimes differential inflation can occur and cause elevation differences in a single sheet (Garry et al., 2012). Pāhoehoe lava flows can flow across nearly horizontal pre-existing surfaces, surfaces with slopes < 1°. The edges of sheet flows are marked by monoclinal features with shallow to steep dips (10° - 80°; Hon et al., 1994a) . The break in slope between the planar surface of the sheet flow and the monoclines is marked by *en echelon* cracks 1 – 2 m deep.

1.6.2 Subaqueous Sediment Gravity Flows

The term subaqueous sediment gravity flow is a general classification that encompasses many types of subaqueous lateral flow processes, with the two end-members being debris flows and turbidity flows. The various flow processes are classified by physical and mechanical variations, such as sediment concentration, particle cohesion, particle support mechanisms, duration, and rheology (Figs. 1.12 and 1.13; Haughton et al., 2009). Debris flows are cohesive, matrix-supported flows. The sediment carried by debris flows varies in size, shape, and composition. The resulting deposit, when lithified, is a poorly sorted conglomerate (Mulder and Alexander, 2001). Subaqueous debris flows can be very fluid and travel across slopes of < 1° for several hundred kilometers (Gee et al., 2001; Mulder and Alexander, 2001).

Turbidity flows are the opposite endmember from subaqueous debris flows. The turbidite deposits vary depending on their distance from the source. Distal deposits are characterized by the well-known Bouma sequence (Mulder and Alexander, 2001). The bottom portion of the Bouma sequence consists of a massive bed of sand sized particles (Shanmugam, 1997; Mulder and Alexander, 2001). The upper portion of the Bouma Sequence consists of laminated silt to mud sized particles. This lamination varies from parallel to cross-laminated as you move up the sequence (Shanmugam, 1997). There are multiple sub-divisions of sedimentary gravity flows between debris flows and turbidity currents. The grain size of these sub-divisions fall between the sand sized particles, found in turbidite deposits, to larger conglomerates found in debris flows.

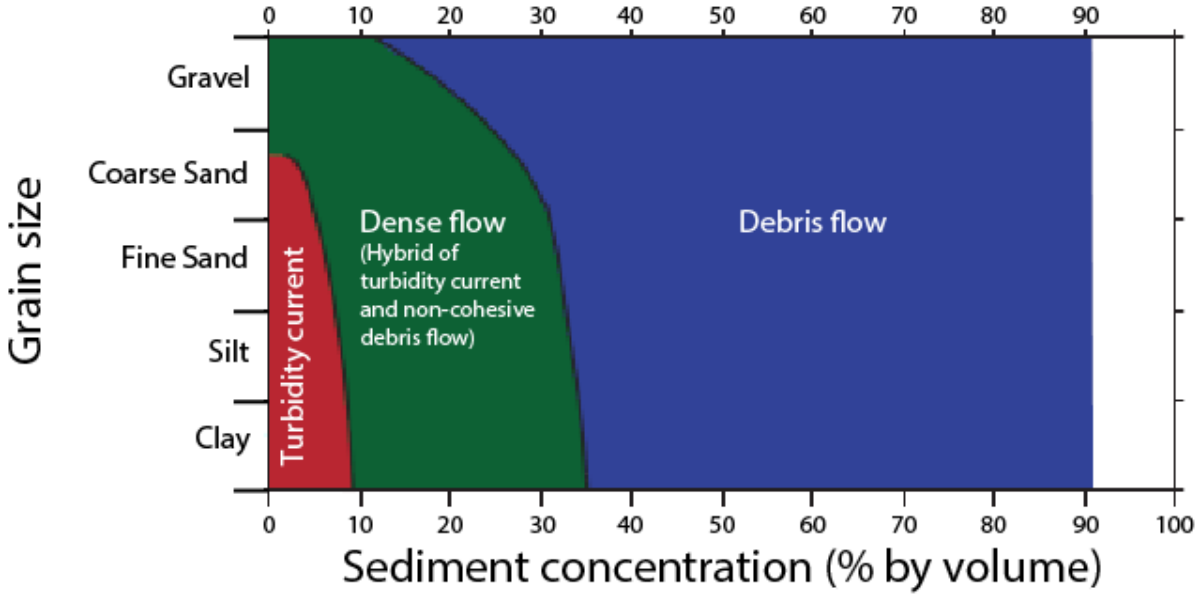

Figure 1.12: X-Y diagram showing the variations between the different types of sedimentary gravity flows. The end members are debris flows, with the highest sediment concentration, and turbidity currents with the lowest sediment concentration. The grain sizes of the resulting deposits can overlap between the various types of sedimentary gravity flows. [Modified from Gani, 2004].

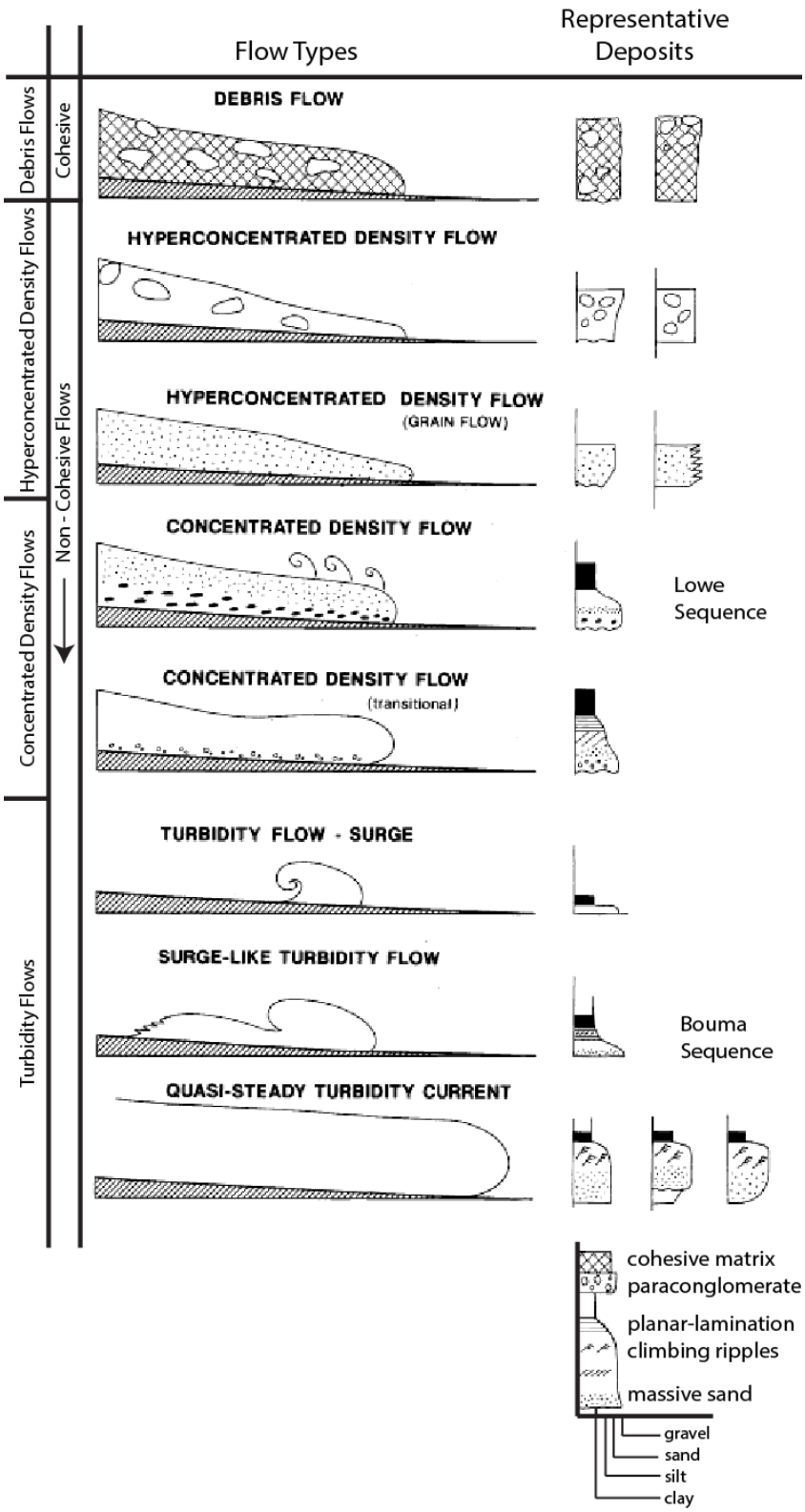

Figure 1.13: Schematic diagram showing the classifications of ideal subaqueous sedimentary gravity flows and the resulting deposits. [Modified from Mulder and Alexander, 2001].

1.6.3 Deltas

Fluvial deltas occur when a river meets a standing body of water and river sediments are deposited in a tripartite progradational sediment package (Bhattacharya, 2006). Delta deposits consist of nearly horizontal topsets, inclined foresets, and nearly horizontal bottomsets (Fig. 1.14; Bhattacharya, 2006). Deposition along each part of the delta is controlled by slightly different sedimentary processes. Topsets are sub-aerial, planar stratified, conglomerate deposits (Mortimer et al., 2005; Bhattacharya, 2006). Foresets are characterized by planar stratified beds of conglomerates and fine to medium grain sandstones. Foresets are the result of sub-aqueous grain flows and sediment avalanching down the foreset slope (Mortimer et al., 2005). The slopes of deltaic foresets can range from 10° - 25° (Bhattacharya, 2006). Foresets can range in thickness up to a few 10s of meters and increase in thickness as the delta progrades into the pre-existing body of water. The height of foresets depends on the depth of the body of water into which the delta is flowing. Bottomsets are characterized by fine to medium grained sandstones, and are the result of the suspension of material from sub-aqueous density currents (Mortimer et al., 2005).

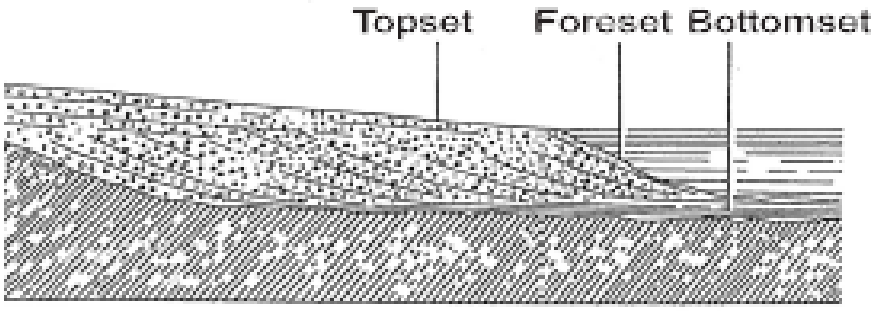

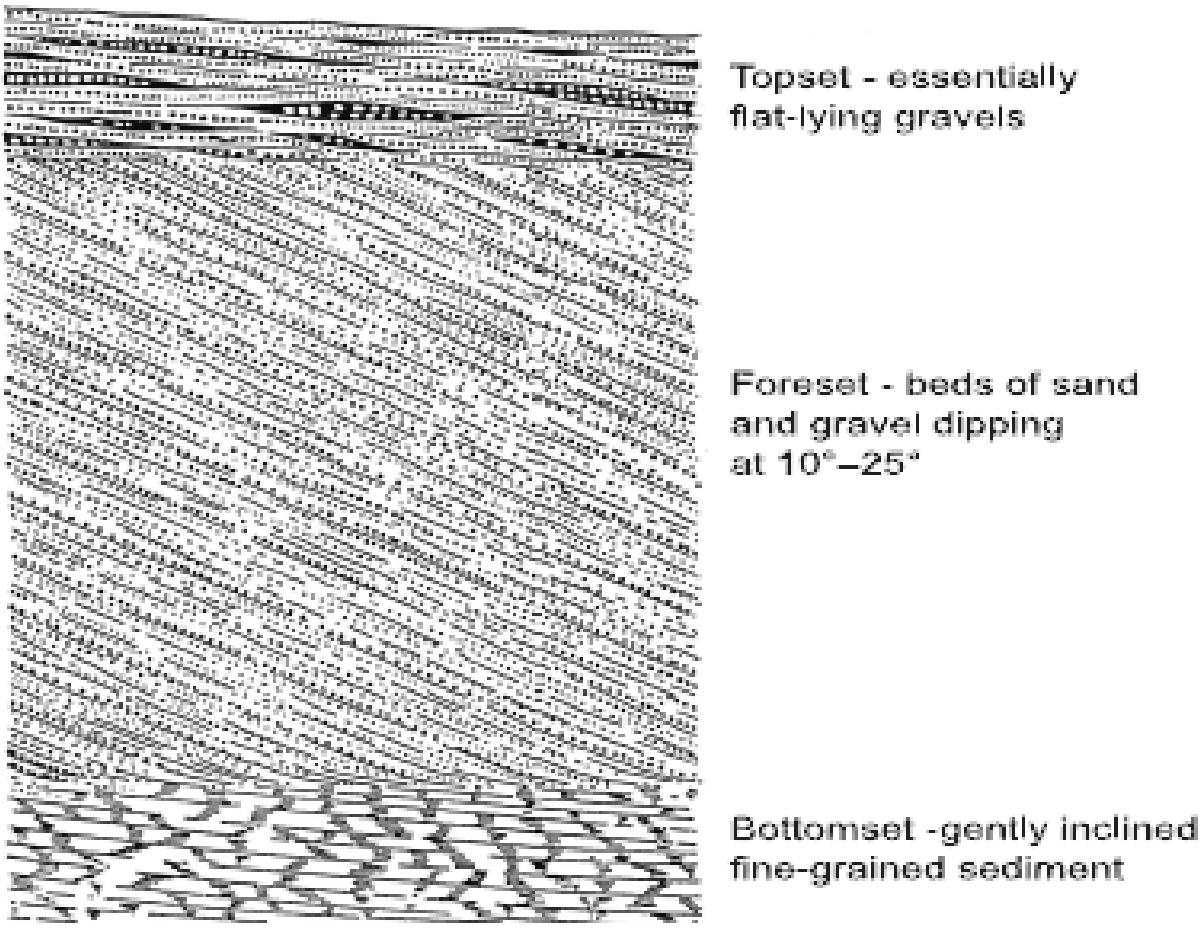

Figure 1.14: Geometry of deltaic deposits. (Figure 2 in Bhattacharya, 2006 after Gilbert, 1890).

1.6.4 Aeolian Dunes

Aeolian dune deposits are formed by the buildup of sand and are divided into bounding surfaces (Fig. 1.15). There can be up to three types of bounding surfaces in an aeolian deposit that are defined by the orientation of their depositional surface. First order bounding surfaces are nearly horizontal (Brookfield, 1977; Kocurek, 1981). Second order bounding surfaces tend to have a low to moderate dip in the downwind direction and are truncated by first order bounding surfaces. The second order bounding surfaces represent slipface deposits caused by the avalanching of sand grains down the lee face of the aeolian dune. Third order bounding surfaces are rare and have a steeper dip than second order bounding surfaces, also in the downwind direction (Brookfield, 1977; Kocurek, 1981). Third order bounding surfaces represent a change in the aeolian environment, typically a change in the wind direction.

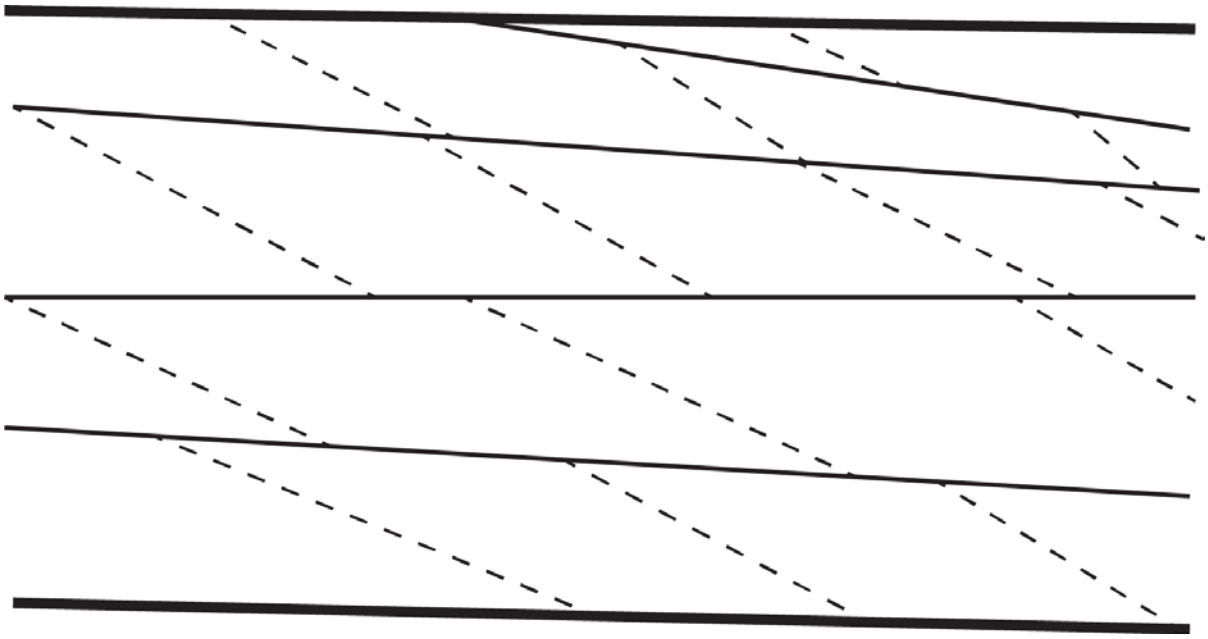

Figure 1.15: Cartoon depicting aeolian bounding surfaces. First order bounding surfaces (thick black lines) represent erosional surfaces. Second order bounding surfaces (thin black lines) represent slipface deposits. Third order bounding surfaces (dashed lines) represent a change in the aeolian environment. [Modified after figure 1 in Kocurek, 1981].

Chapter 2

Cratered Surface Characterization and Geologic Origin

2.1 Geomorphic Characteristics of the Cratered Surface

There are three distinguishing geomorphic characteristics of all CS exposures in the landing ellipse; these are a high crater density, mesa-forming erosional scarps, and a nearly horizontal slope. The CS preserves a large number of impact craters and has the highest crater density (# craters/km^2) of small craters 1 - 31 m in diameter compared to the other landing ellipse units. Whereas all of the CS exposures have a high crater density, there are slight, but quantifiable variations in crater density and surface textures that aided in the subdivision of the CS into five sub-units. These five sub-units are the CS_Flat, CS_Infill1, CS_Infill2, CS_Bedded1, and CS_Bedded2 (Fig. 2.1). The craters range in size and are in various stages of erosion; the specifics of the crater density calculations are discussed in chapter 3. For the following descriptions of the CS sub-units, exposure will be used to denote the CS sub-unit as seen in HiRISE images and outcrop will be used for in situ portions of the CS sub-unit observed in Mastcam images. Figure 2.2 shows the location of scientific waypoints, near CS sub-units, where Curiosity conducted extensive contact science campaigns. These locations will be discussed throughout the text.

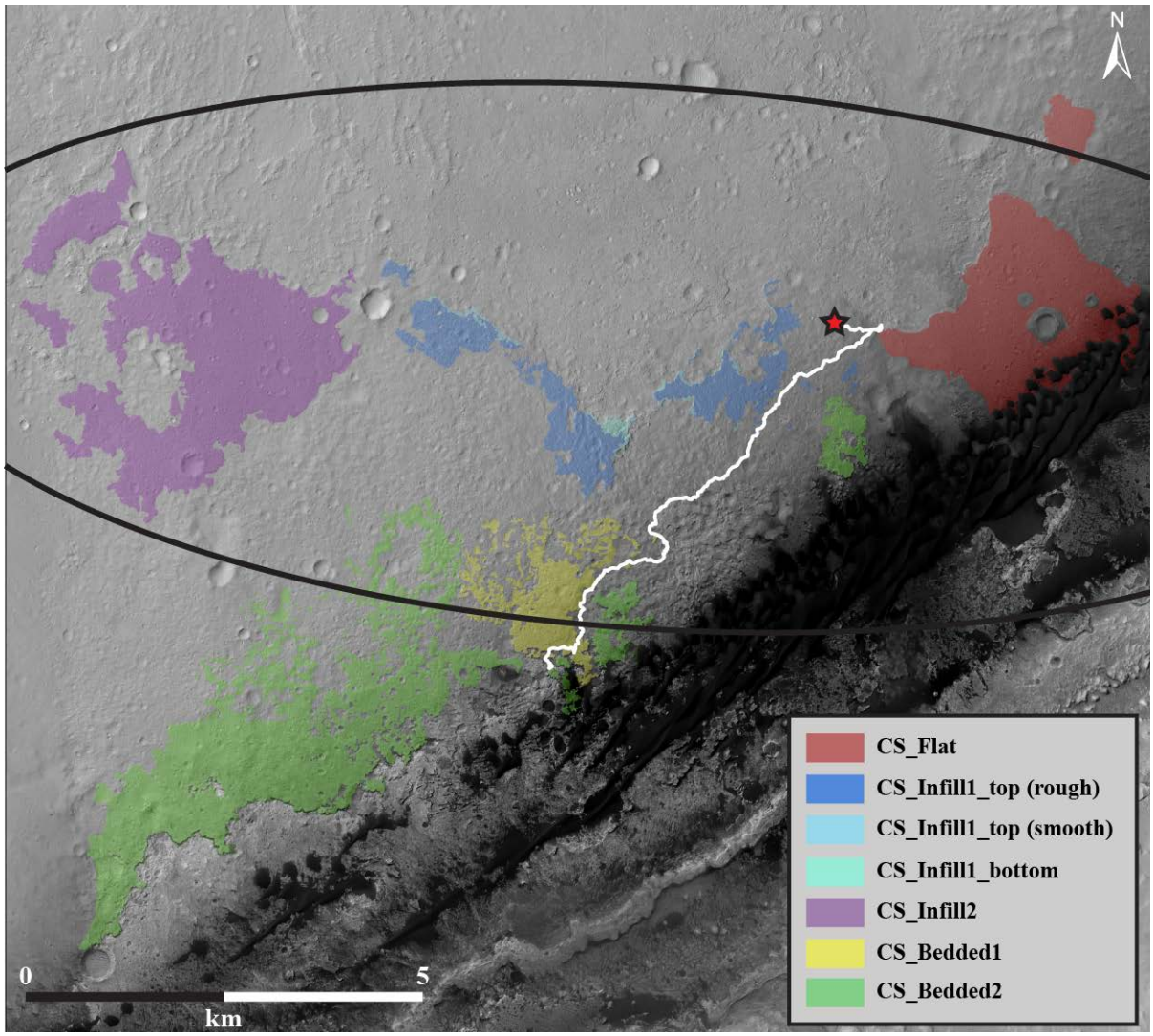

Figure 2.1: CS sub-units, defined by differences in surface morphology. The red outlined star is the Curiosity landing site and the white line shows the Curiosity traverse through sol 926. The black ellipse is the Curiosity landing ellipse.

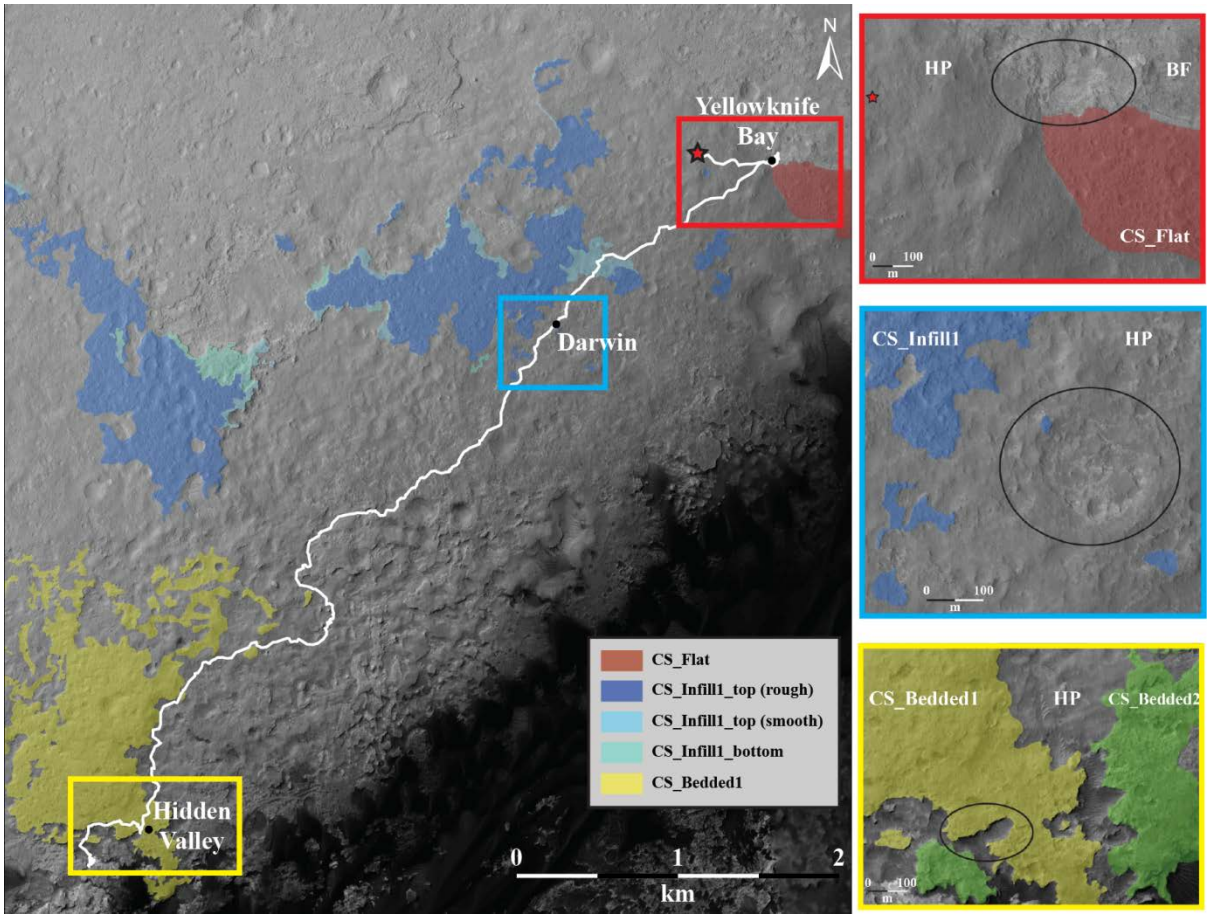

Figure 2.2: A location map highlighting a few scientific waypoints, near CS sub-units.

2.1.1 CS_Flat

The CS sub-unit nearest the landing site is CS_Flat (Fig. 2.3). This sub-unit is present only on the eastern side of the landing site and was differentiated from the other CS exposures on its nearly horizontal and smooth surface. The entire CS_Flat exposure has a consistent albedo, which gives the exposure a smooth surface appearance. There are two separate exposures of CS_Flat that together have a combined area of 4.4 km^2 and an average thickness of 1 m. The larger, southern exposure has an average slope dipping ~1° down to the north. The southern CS_Flat exposure is surrounded by the HP unit to the west and south. At the contact between CS_Flat and the HP unit, there is no significant elevation difference; therefore there is no erosional scarp. The HP unit does, however, gradually increase in elevation to the west, an area which has been informally called Bradbury Rise

(Fig. 2.4). At this location, CS_Flat is topographically lower than the HP unit. To the NW, CS_Flat contacts and overlies the BF unit. Along this contact, there is a ~1.5 m erosional scarp denoting an elevation drop from the top of the CS_Flat exposure to the top of the BF exposure (Fig. 2.5). The erosional scarp delineates the minimum thickness (~1.5 m) of CS_Flat.

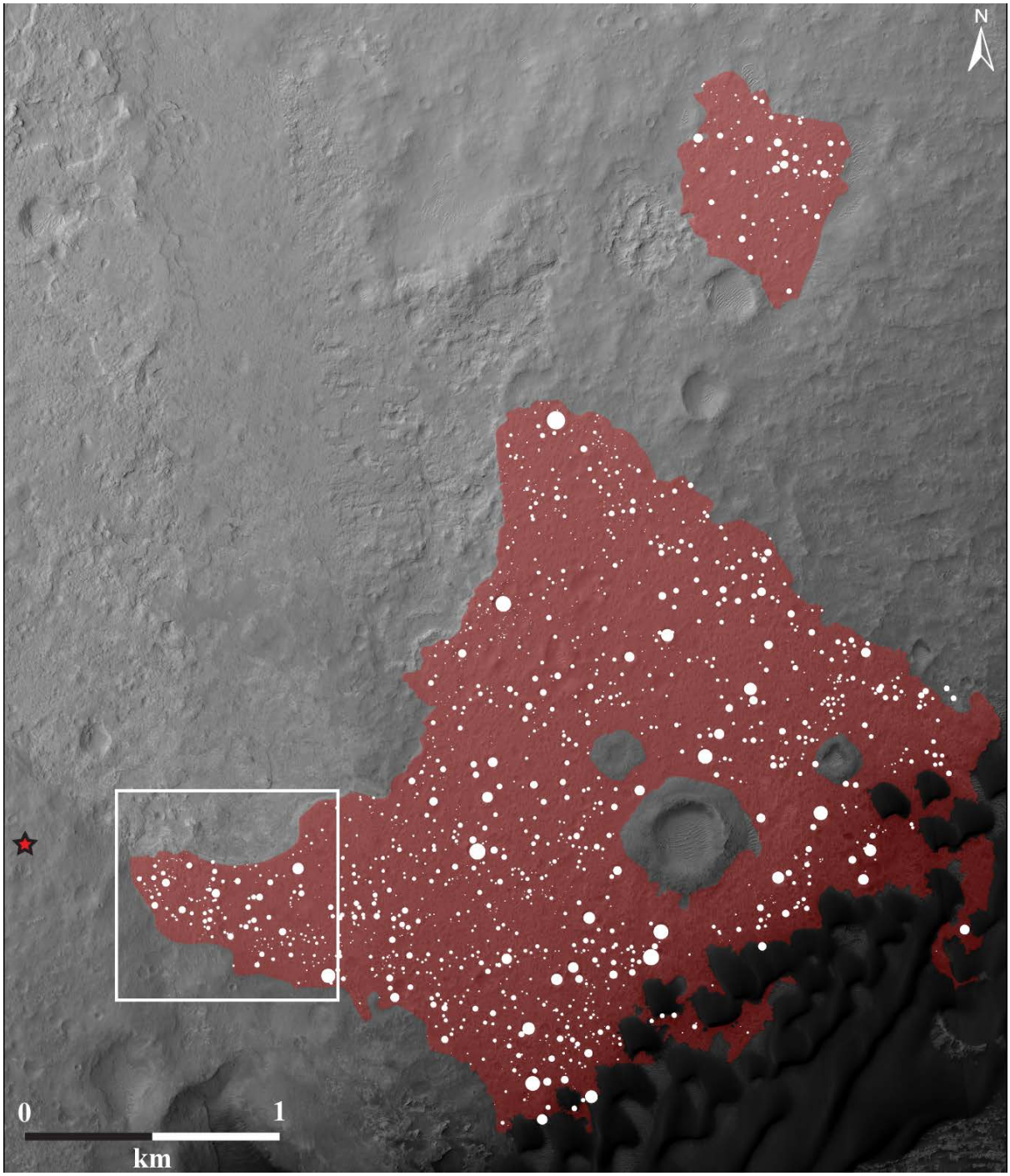

Figure 2.3: Areal extent and crater distribution of CS_Flat. The white box shows the location of figure 2.5. The red outlined star is the Curiosity landing site.

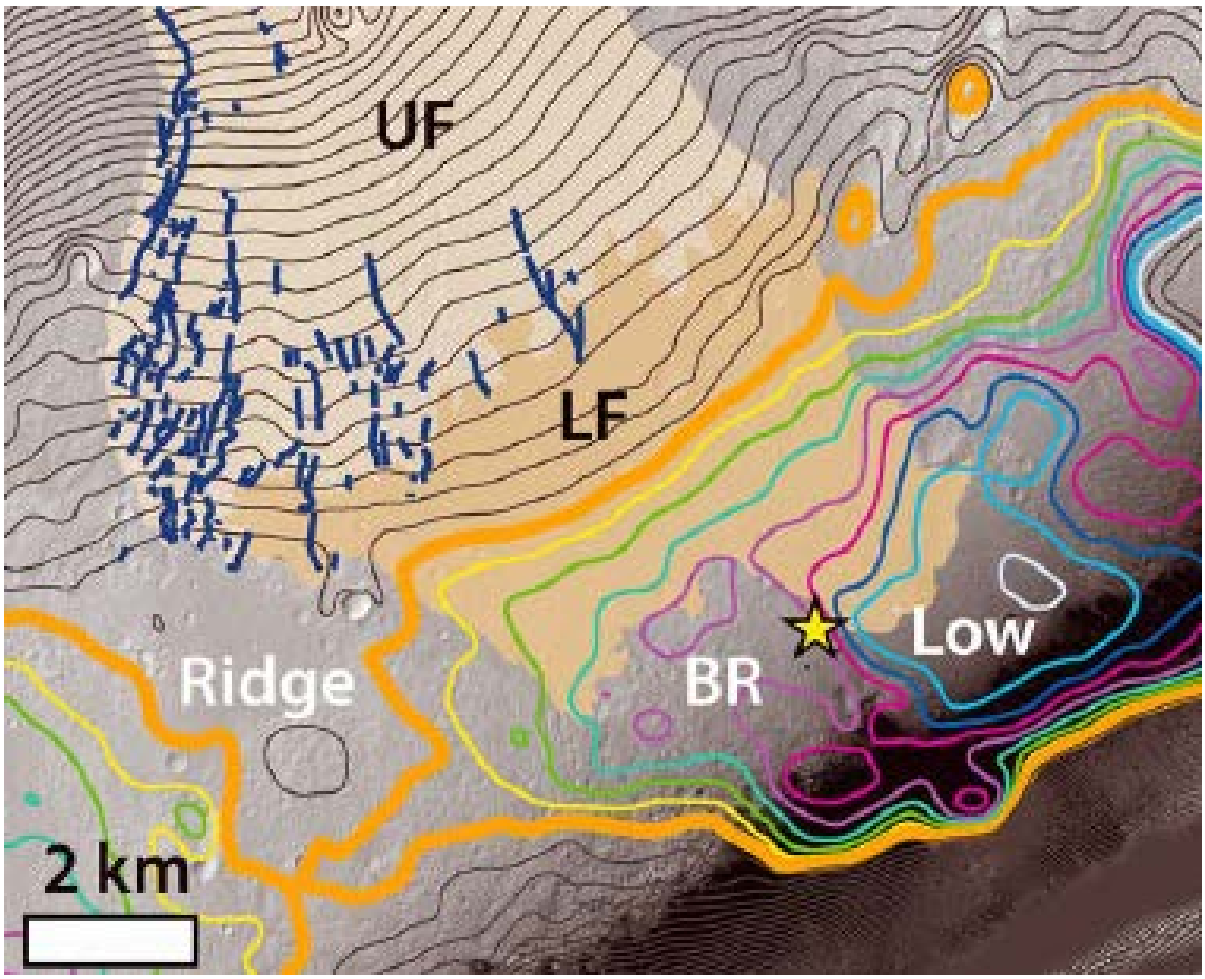

Figure 2.4: Topographic map of the Curiosity landing ellipse showing the location of Bradbury Rise (BR) compared to the location of CS_Flat. In this figure CS_Flat is indicated by the low area on the east. The yellow star indicates the Curiosity landing site. [Modified from Palucis et al., 2014 figure 5].

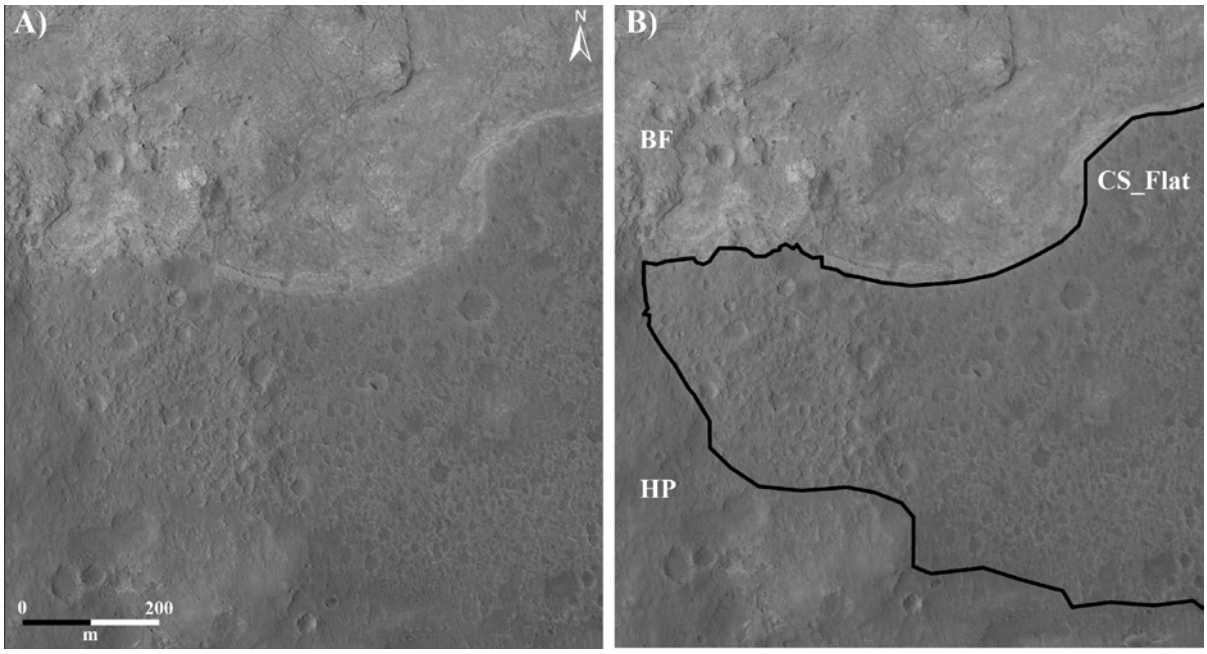

Figure 2.5: Unannotated and annotated portions of HiRISE image ESP_023957_1755, showing the western contact between the CS_Flat (outlined on right), HP, and BF units.

Curiosity first encountered CS_Flat on sol 120, during the rover's descent into Yellowknife Bay. Shortly after landing, the MSL team members collectively decided to drive east of the landing site to explore Yellowknife Bay (Grotzinger et al., 2014). This area was picked for the rover's first major stop because of its proximity to the intersection point between the CS, BF, and HP units, the area's high thermal inertia, and the fractured stratified deposits that could be traced in HiRISE images (Grotzinger et al., 2014). After looking at the Mastcam images taken en route to Yellowknife Bay, the strata were mapped into three different members, which, in ascending order, are the Sheepbed, Gillespie Lake, and Glenelg members (Grotzinger et al., 2014). Additionally, the Glenelg member was divided into various outcrops including Point Lake, Shaler, Rocknest, and Bathurst (Grotzinger et al., 2014; Anderson et al., 2014).

Shaler is distinct among the outcrops of Glenelg because of its thinly layered outcrops of resistant and recessive strata. Shaler is about 1 m thick and can be traced more or less along strike for ~20 m (Anderson et al., 2014). Shaler was later sub-divided into seven facies based on grain size, texture, color, sedimentary structures, and resistance to erosion. The top five facies were imaged and analyzed by Curiosity on sols 120-121 and again on sols 309-

324. The entirety of the Shaler outcrop was originally categorized as a part of the HP unit. For this project however, facies 7 of Shaler has been re-categorized as the edge of the CS_Flat deposit. Mastcam mosaics (Figs. 2.6 and 2.7) of the Shaler outcrop show the contact between CS_Flat and (underlying) facies 6 of Shaler.

In Mastcam images CS_Flat is characterized by dark float rocks with a fine grained texture and pitted surfaces. Most of the float rocks in CS_Flat are massive, except for one ChemCam target, Mary_River, which has faint cross-stratification. This is distinctly different from the lower facies of Shaler, which have very pronounced bedding and other sedimentary textures (Anderson et al., 2014; Siebach et al., 2014; Stack et al., 2014). The CS_Flat deposit is relatively free of Martian dust, in contrast to the surrounding rocks, which makes it very different in color from the lower six facies of Shaler.

CS_Flat is now mostly weathered float rocks, except for a small in situ outcrop imaged by Mastcam on sol 121 (Fig. 2.7). The outcrop has a rough, wind-sculpted surface (similar to that of the float rocks) and consists of two distinct lithologies. The lower lithology, which is ~6 cm thick, displays hints of layering that have been enhanced by differential weathering. The upper ~6 cm consists of dark, relatively fine grained, massive rock. This outcrop can be traced laterally for a distance of ~2 m. The thickest section of the outcrop is ~12 cm.

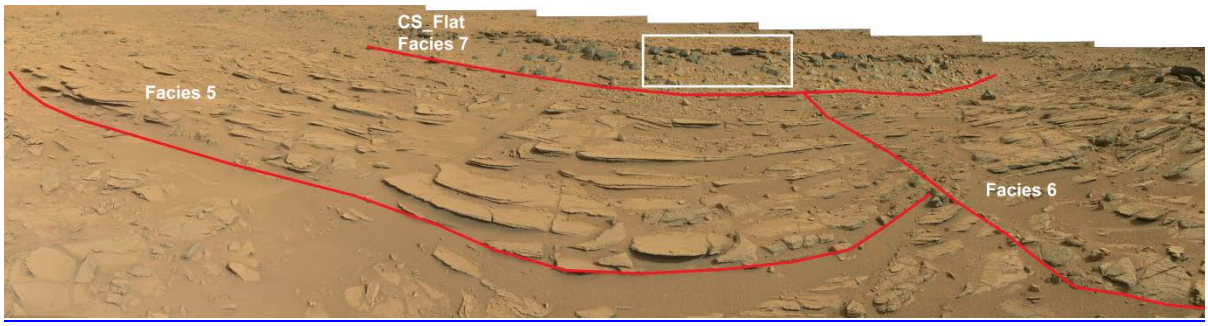

Figure 2.6: Mastcam mosaic (mcam00753) of the Shaler outcrop, taken on sol 120. The dark float rocks of CS_Flat are at the top of the image. The white box indicates the location of figure 2.7. The individual images used for this mosaic can be found at: http://mars.jpl.nasa.gov/msl/multimedia/raw/?s=120&camera=MAST_.

Figure 2.7: Mastcam (M-34) mosaic of the CS_Flat deposit, taken on sol 121. This image shows that CS_Flat consists mostly of dark, fine grained float rocks. On the right hand side of the image is the only in situ CS_Flat outcrop imaged by Curiosity. The images used for this mosaic can be found at: http://mars.jpl.nasa.gov/msl/multimedia/raw/?s=121&camera=MAST_.

At the end of the Yellowknife Bay campaign, the rover stopped again at the CS_Flat deposit on sols 315-322. CS_Flat was imaged again with Mastcam and also analyzed using ChemCam. Specifically, four float rocks were chosen as ChemCam targets including Chioak, Mary_River, Husky Creek, and Sokoman (see Table 1 for LIBS results and specifics of ChemCam observations). The targets Chioak, Mary_River, and Husky Creek were analyzed with the LIBS and imaged with the RMI (Fig. 2.8). The RMI images of Mary_River show hints of cross-bedding (Fig. 2.8B). The top 2/3 of Mary_River is the only target with grains large enough to be resolved, they range from very coarse sand to granule in size and have an average size of 1.945 mm (Anderson et al., 2014). The lower ~1/3 of Mary_River has smaller (and unresolvable) grains than the top 2/3 of the rock. The target Sokoman was only imaged with the RMI because it was too far from the rover to analyze with LIBS (Fig. 2.9). All four targets of the CS_Flat deposit have a similar fine grained, pitted texture in the RMI images.

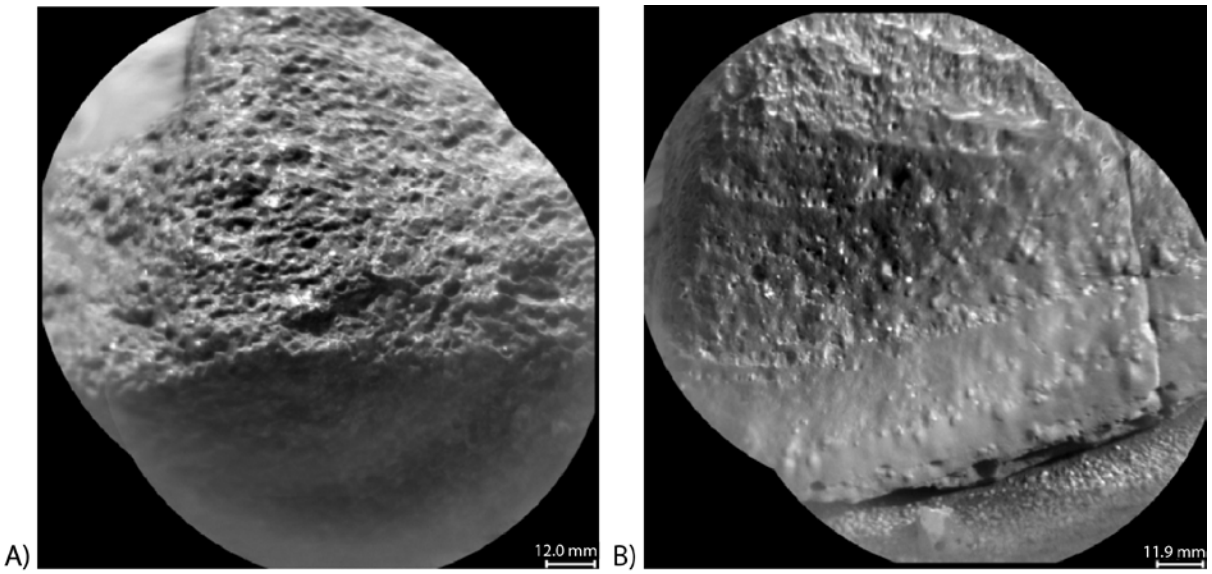

Figure 2.8: RMI images of targets from CS_Flat: A) Chioak and B) Mary_River, which shows hints of cross-bedding near the base of the target.

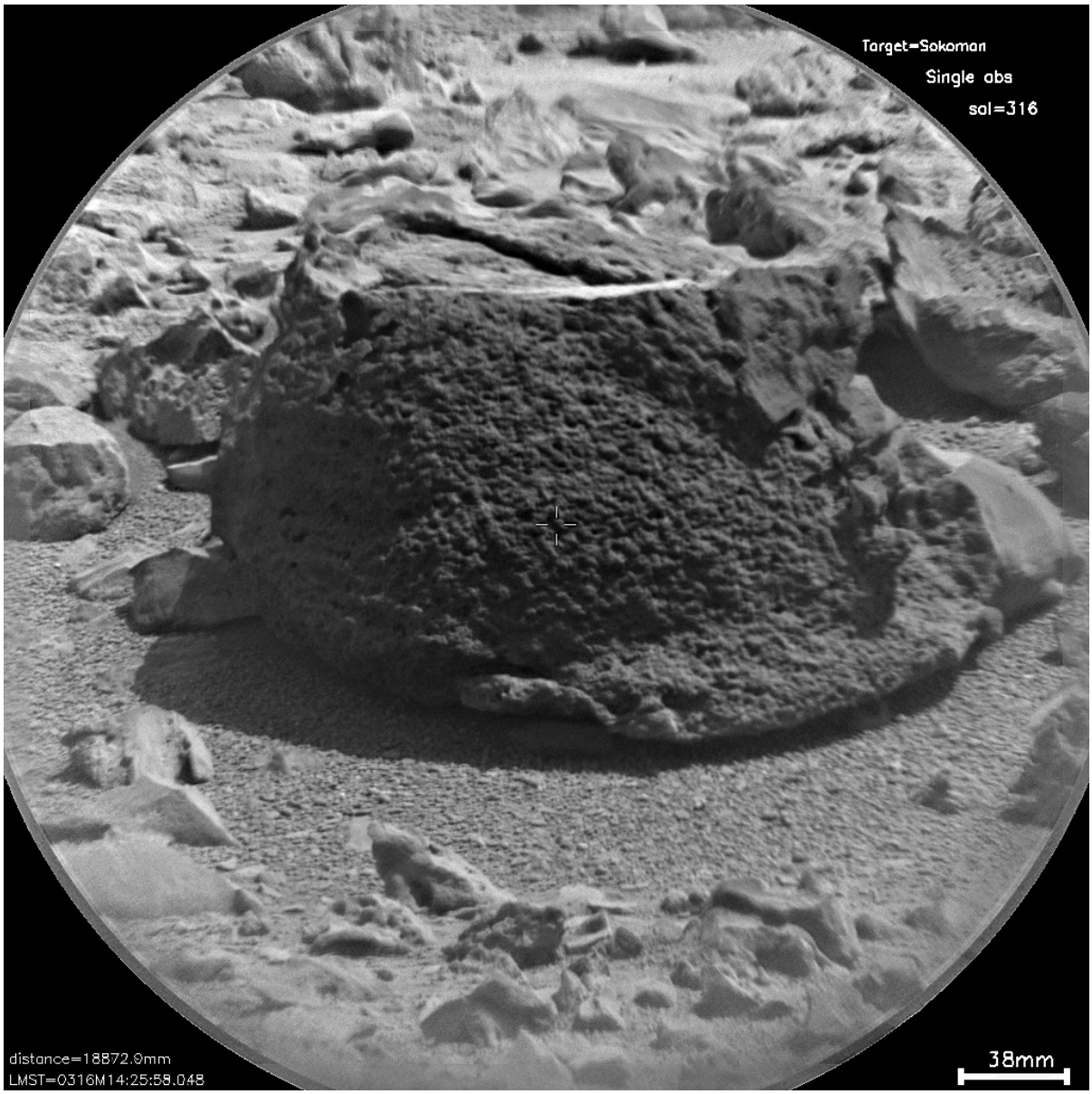

Figure 2.9: RMI z-stack of the CS_Flat target Sokoman, showing the pitted and fine grained texture of the CS_Flat float rocks.

Of the three CS_Flat targets that were analyzed by LIBS, only Mary_River and Chioak had sufficient signal to noise ratios to calculate their elemental concentrations (Anderson et al., 2014). The LIBS analyses showed that Mary_River and Chioak both have high Si, Al, Na, and K when compared to the lower Shaler facies (Anderson et al., 2014). These CS_Flat float rocks differ from Shaler both physically and chemically, suggesting that CS_Flat is a completely separate geologic unit from the Shaler outcrop (see section 2.2.1).

Table 1.1: ChemCam results of CS targets

Target	Sol	Sub-unit	Seq_ID	Range (m from ccam)	Observation	SiO_2	TiO_2	Al_2O_3	FeO_t	MgO	CaO	Na_2O	K_2O	Total
Chioak	315	CS_Flat	ccam01315	4.595	3x3	52.2	1.0	9.6	19.9	4.3	6.2	3.1	1.4	97.7
Mary_River	316	CS_Flat	ccam04316	6.030	3x3	54.0	1.0	10.1	19.2	5.8	6.9	3.4	1.7	102.1
Black_Trout	349	CS_Infill1	ccam01349	2.533	3x3	59.4	1.0	10.8	16.0	1.8	6.0	3.1	1.4	99.5
Mallard_Lake	349	CS_Infill1	ccam03349	4.823	1x5	56.3	1.0	11.9	14.6	5.0	11.2	3.4	1.3	104.7
Bull_Arm	349	CS_Infill1	ccam02349	5.650	1x5	56.8	1.8	13.7	16.6	6.1	6.5	3.5	1.5	106.5
Byrd	396	CS_Infill1	ccam03394	3.430	1x5	63.8	1.7	14.0	14.4	2.5	1.8	2.7	1.1	102.0
Pebble	399	CS_Infill1	ccam02399	4.240	5x1	69.2	1.6	14.4	14.1	2.7	0.6	2.8	1.7	107.1
Onondaga	502	CS_Bedded1	ccam02502	2.221	1x5	58.6	0.7	12.0	11.0	1.0	5.2	4.6	2.0	95.1
Beagle	618	CS_Bedded1	ccam01618	3.952	4x4	47.4	1.1	8.2	18.7	5.4	6.5	2.3	1.2	90.8
Eliot	663	CS_Infill1	ccam01663	4.467	3x3	53.9	1.3	11.7	18.3	1.3	6.1	2.8	1.7	97.1
Balch_Hill	666	CS_Infill1	ccam01666	2.833	1x5	57.8	0.4	9.3	11.5	1.4	6.4	3.5	2.6	92.9
Calef	669	CS_Infill1	ccam02669	6.154	5x1	60.0	1.2	22.4	12.4	2.5	0.7	5.6	2.4	107.2
Johnnie	694	CS_Bedded1	ccam01694	2.251	1x5	48.9	1.1	6.9	20.2	7.3	5.5	2.3	0.8	93.0
Skidoo	701	CS_Bedded1	ccam06700	2.963	1x10	51.0	1.3	8.2	18.4	4.7	6.5	2.3	1.0	93.4
Chocolate_Sundae_Mountain	701	CS_Bedded1	ccam07700	4.070	1x10	52.4	1.0	9.5	18.4	5.6	5.8	2.7	1.3	96.7
Cuzcatlan	703	CS_Bedded1	ccam01703	3.220	10x1	50.8	1.1	8.5	19.7	1.3	7.1	2.3	1.0	91.8
Andrews_Mountain	703	CS_Bedded1	ccam02703	3.409	1x10	49.9	0.8	8.1	18.8	1.6	6.8	2.4	1.1	89.5
Poleta	703	CS_Bedded1	ccam01705	4.508	3x3	54.4	0.9	8.1	22.1	3.0	4.6	3.0	1.5	97.6
Resting_Spring	704	CS_Bedded1	ccam04704	4.410	3x3	53.8	0.6	8.2	21.0	2.4	5.0	2.7	1.5	95.2
Thimble	704	CS_Bedded1	ccam03704	4.450	1x5	56.0	0.8	9.6	18.8	2.6	6.7	3.2	1.7	99.4

2.1.2 CS_Infill1

West and southwest of the Curiosity landing site are scattered exposures of CS_Infill1 (Fig. 2.10). Together all the CS_Infill1 exposures cover an area of ~5.5 km^2. In HiRISE images, CS_Infill1 forms a ~2 m erosional scarp where it contacts the underlying HP unit (Fig. 2.11), forming small mesas. Each of the individual exposures has a horizontal surface, < 0.5° slope. The average thickness of the CS_Infill1 exposures is 0.8 m. Due to the mottled albedo of CS_Infill1 exposures, the surface appears to have a rough surface morphology. In some places CS_Infill1 forms a single scarp, whereas elsewhere it is clear that CS_Infill1 consists of layers which form steps from the upper surface down to the underlying HP unit (Fig. 2.11).

Some of the larger CS_Infill1 exposures have been divided into two layers (Figs. 2.10 and 2.11). The layers are distinguished mainly by variations in surface morphology, surface area, and crater density. The top layer of all the CS_Infill1 exposures is mainly characterized by a rough surface morphology, and has the highest crater density of the two layers. However, portions of the surface of the top CS_Infill1 layer, near the edges of the exposures, have a smooth morphology and very few impact craters. There is little to no elevation difference between the smooth and rough portions of the CS_Infill1 top layer, and they make a single topographic mesa; therefore the smooth and rough portions of the top CS_Infill1 layer are still considered to be the same layer. The top layer is mostly surrounded by the topographically and stratigraphically lower HP unit. At the contact of the top CS_Infill1 layer and HP unit, there is typically an erosional scarp that ranges from 2 – 6 m in height (Fig 2.11). However, in other locations, there is a very small topographic difference at the contact between the top CS_Infill1 layer and HP unit. At one location, which will be discussed in detail later, the top CS_Infill1 layer sits topographically lower, but stratigraphically above, the rim of an impact crater in the HP unit.

Lastly, there is the bottom layer of CS_Infill1. The exposures of the bottom layer are very sparse. The largest visible area of this layer shows that the surface is smoother than the main rough portions of the top CS_Infill1 layer, but rougher than the smooth edges of the top

CS_Infill1 layer. The bottom CS_Infill1 layer has virtually no impact craters. There is an elevation difference of ~2 m between the top CS_Infill1 layer and the bottom CS_Infill1 layer. The contact between the bottom CS_Infill1 layer and the HP unit is ~2 m.

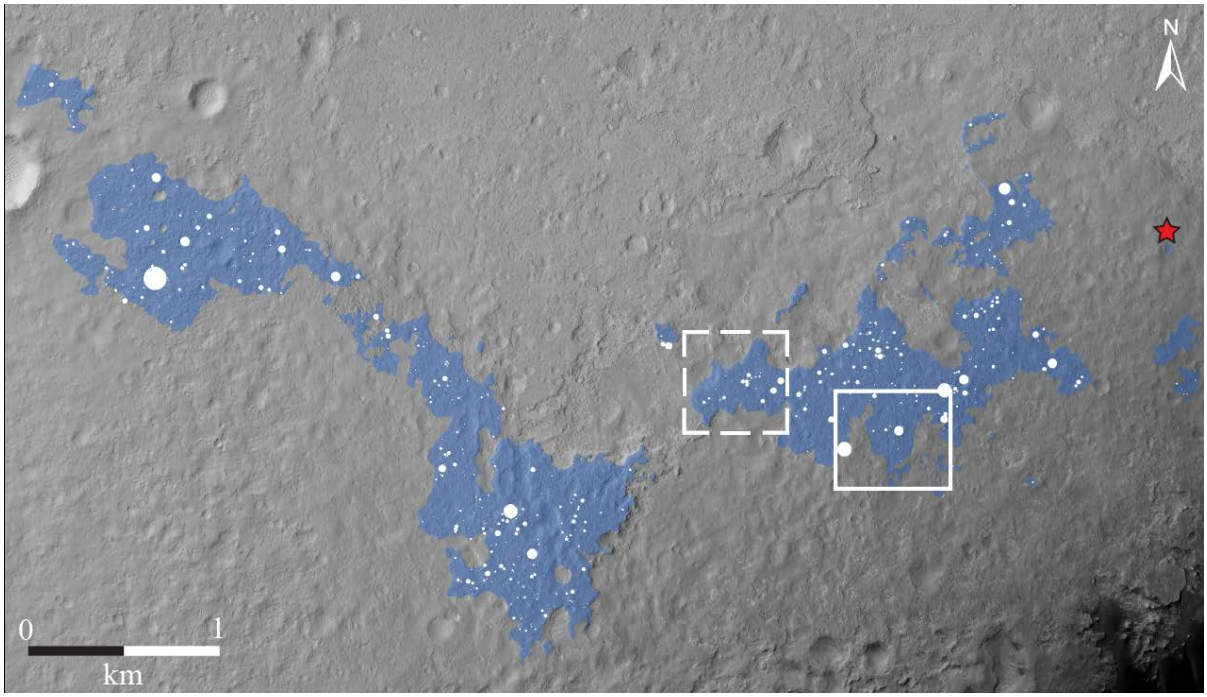

Figure 2.10: Areal extent and crater distribution of CS_Infill1. The dashed white box shows the location of figure 2.11, and the solid white box shows the location of figure 2.25. The red star is the Curiosity landing site.

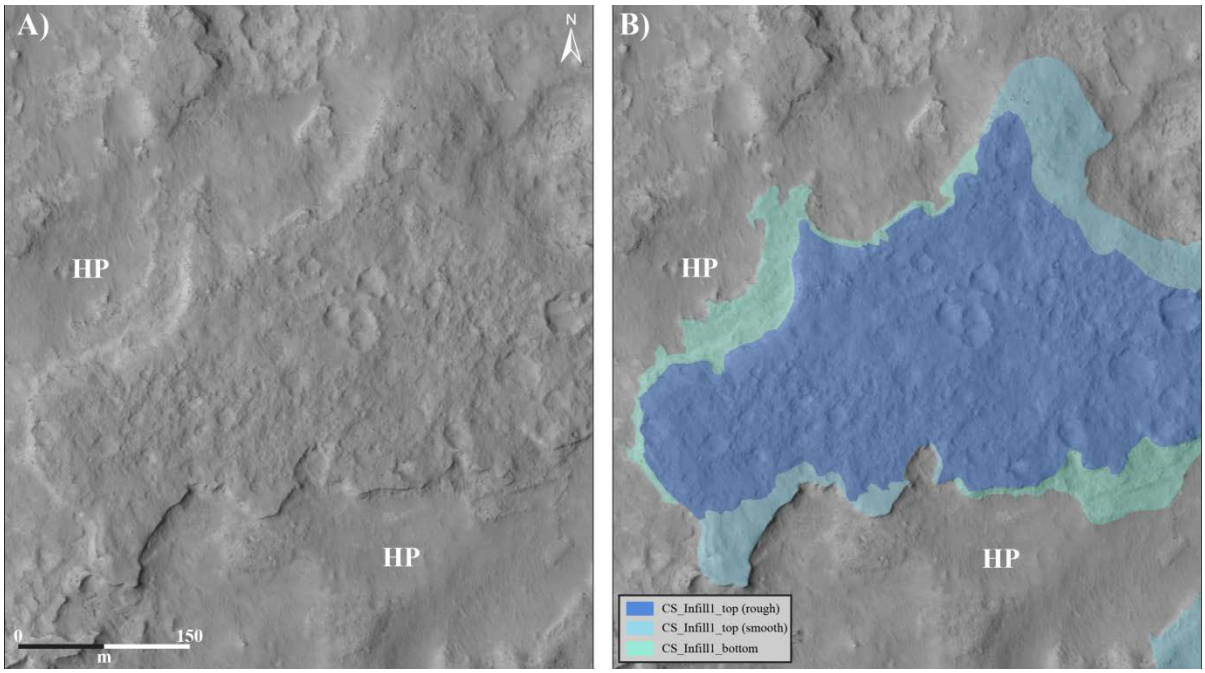

Figure 2.11: Unannotated (A) and annotated (B) portions of HiRISE image ESP_022111_1755, showing the erosional scarp along the western contact between the CS_Infill1 and HP unit. The image also shows the surface textures of the two CS_Infill1 layers and the smooth portions of the top CS_Infill1 layer.

The CS_Infill1 unit was visited by Curiosity, at the Darwin waypoint, on sols 387-401 during the drive to the base of Mt. Sharp (Fig. 2.2). The area visited correlates to the top CS_Infill1 layer. This patch has an area of ~464 m^2. In the HiRISE images, it stands out as a cratered mesa, standing at an elevation of -4505 m, which is almost 2 m above most of the surrounding area. The float rocks on and nearby this mesa are dark, pitted, and fine grained (Fig. 2.12), similar to the float rocks at the CS_Flat location discussed above. However at this location, there is no in situ outcrop visible in the Mastcam images.

Figure 2.12: Mastcam (M-34) image of CS_Infill1 float rocks at the Darwin waypoint, collected from a distance of ~11 m and viewed toward the southeast. The dark float rocks have a pitted, fine grained texture similar to those at the CS_Flat location. The images used for this mosaic can be found at: http://mars.jpl.nasa.gov/msl/multimedia/raw/.

At the Darwin waypoint, a large float rock named Pebble was chosen for ChemCam analysis (Fig. 2.13; Table 1). The results show that Pebble has concentrations of Si, Al, Na, and K indicative of albite or another alkali feldspar phase. This is similar to the elemental composition of the ChemCam targets analyzed at the CS_Flat location. The RMI images show that Pebble has a fine-grained texture with a pitted surface (Fig. 2.14).

Figure 2.13: Mastcam image showing the CS_Infill1 target Pebble. The dark float rocks have a pitted, fine grained texture similar to those at the CS_Flat location. This image can be found at: http://mars.jpl.nasa.gov/msl/multimedia/raw/.

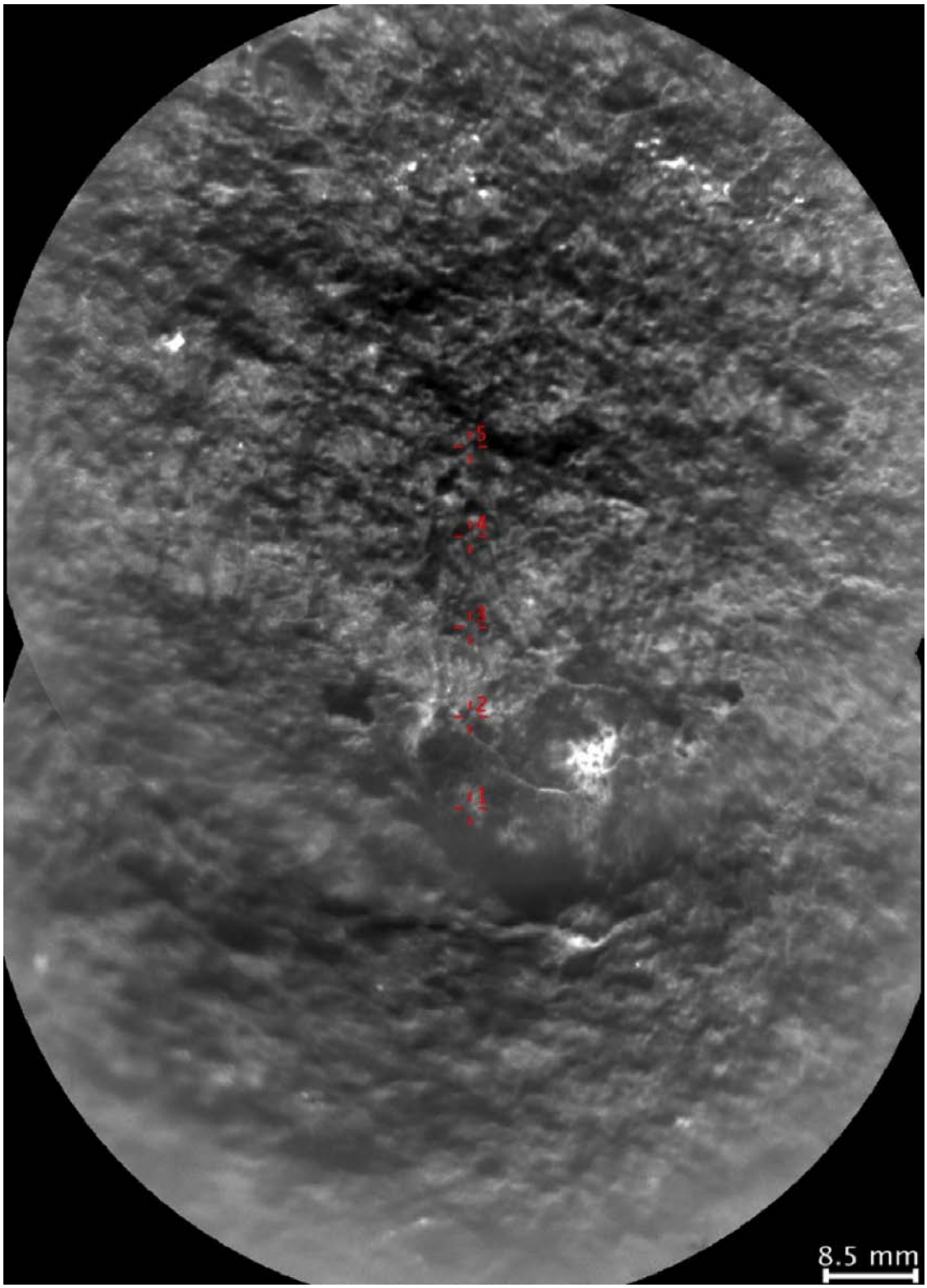

Figure 2.14: RMI image of the CS_Infill1 target Pebble at the Darwin waypoint. The images show that the rock is fine grained and pitted, similar to the CS_Flat targets near Shaler. The red crosses show the locations of the five ChemCam LIBS shots.

2.1.3 CS_Infill2

The CS_Infill2 sub-unit occurs in the northwest portion of the Curiosity landing ellipse (Fig. 2.15). Like CS_Infill1, this CS sub-unit is distinguished by a nearly horizontal surface. However, CS_Infill2 is different in that it has a consistent albedo throughout and therefore appears to have a smooth surface morphology. CS_Infill2 is composed of three separate exposures with a total area of 7.7 km^2. The three exposures all have an average slope of ~1° and an average thickness of ~1 m. CS_Infill2 exposures are relatively indistinct in HiRISE; the similar albedo and typical lack of an erosional scarp at the contact with the HP unit makes CS_Infill2 almost indistinguishable (Fig. 2.16).

The main criterion used to identify CS_Infill2 exposures was its high crater density relative to the underlying HP unit. The distinct erosional scarp delineating the CS_Infill1 boundary is not seen around the majority of CS_Infill2 exposures. The only place the CS_Infill2 forms an erosional scarp is along the northern contact of the largest CS_Infill2 exposure. This scarp is most noticeable because here CS_Infill2 is in contact with the RT and AF units. CS_Infill2 has not been, nor will it be, visited or imaged by Curiosity; therefore its physical characteristics and geologic origin will be described solely from HiRISE data. CS_Infill1 and CS_Infill2 were named because the CS material surrounds and partially fills large, pre-existing impact craters (Figs. 2.23 and 2.24). In both instances, the crater rims are not completely buried by, and stand 1-2 m above the CS_Infill deposits. These stratigraphic relationships are telling of the possible type of depositional environments in which the CS_Infill sub-units originated, and will be discussed further in section 2.2.2.

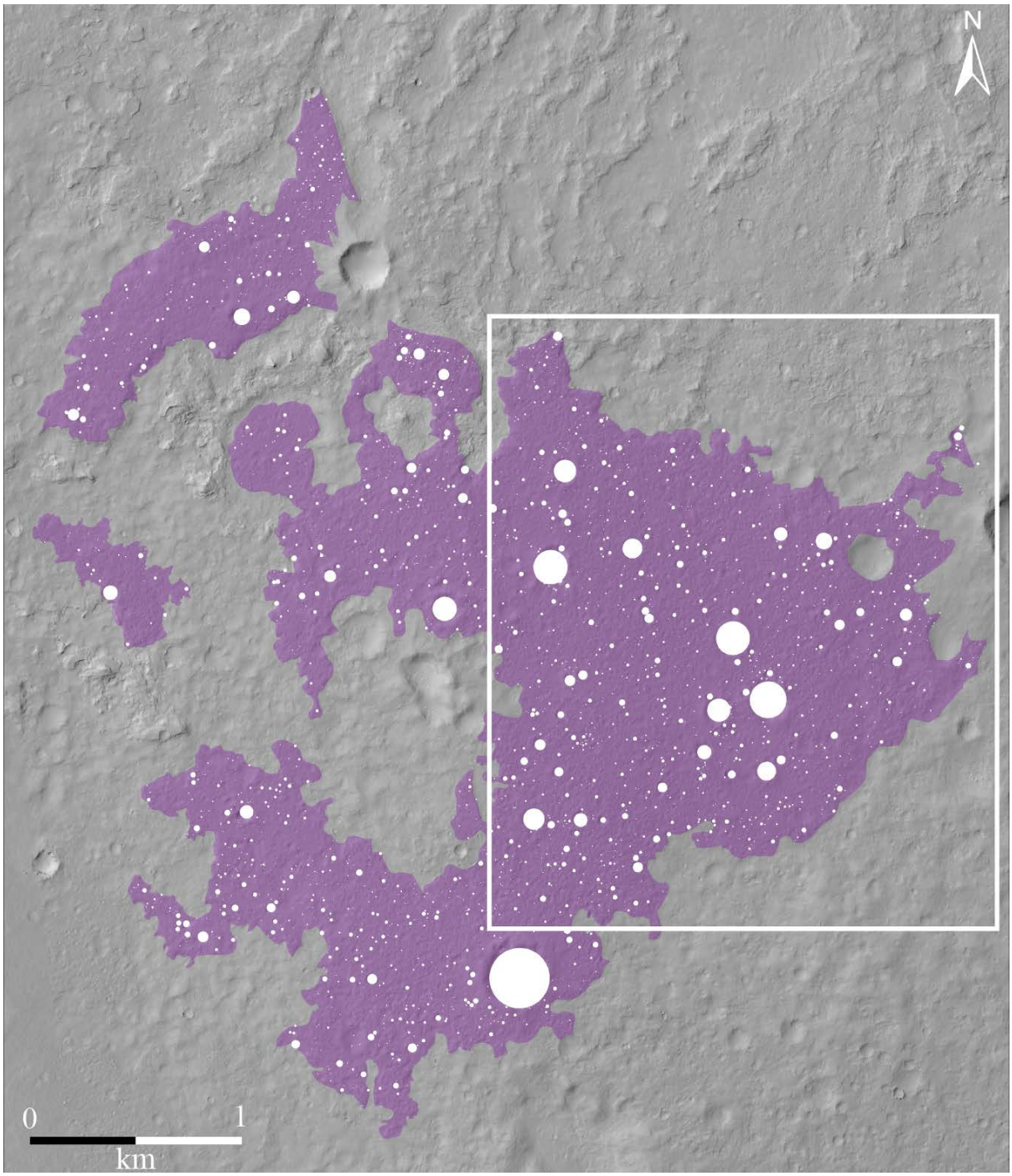

Figure 2.15: Areal extent and crater distribution of CS_Infill2. The white box shows the location of figure 2.16.

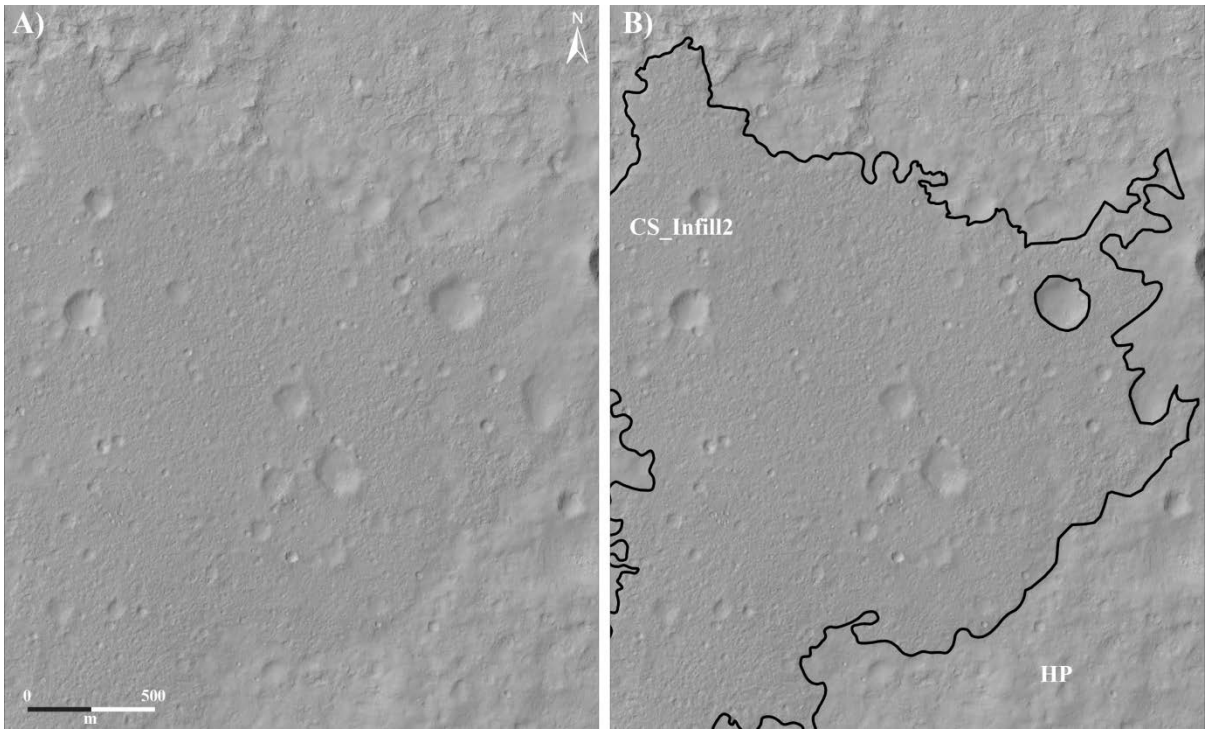

Figure 2.16: Unannotated (A) and annotated (B) portions of HiRISE image ESP_018920_1755, showing the northern portion of CS_Infill2.

2.1.4 CS_Bedded1

Near the southern extent of the Curiosity landing ellipse lies CS_Bedded1. CS_Bedded1 is made of one large exposure and multiple smaller exposures, with a total area of 0.34 km^2. CS_Bedded1 (Fig. 2.17) has a mottled albedo throughout and appears to have a hummocky surface morphology with broad hummocks. The northern boundary of the exposure has a very small erosional scarp, making this boundary with the HP unit somewhat indistinct (Fig. 2.18). The southern boundary, however, forms a ~3 m erosional scarp with the lower units of Mt. Sharp. This scarp was extensively imaged during the Hidden Valley campaign (Fig. 2.19).

After Curiosity visited the CS_Infill1 patch at the Darwin waypoint, the rover spent a couple weeks at Hidden Valley (Fig. 2.2). Curiosity imaged and analyzed CS_Bedded1 at Hidden Valley on sols 703-726. Hidden Valley (Fig. 2.19) is a prominent feature in HiRISE

images because of the ~3 m erosional scarp on both the northwest and southest sides of the valley. The floor of the valley is covered in very fine sand dunes.

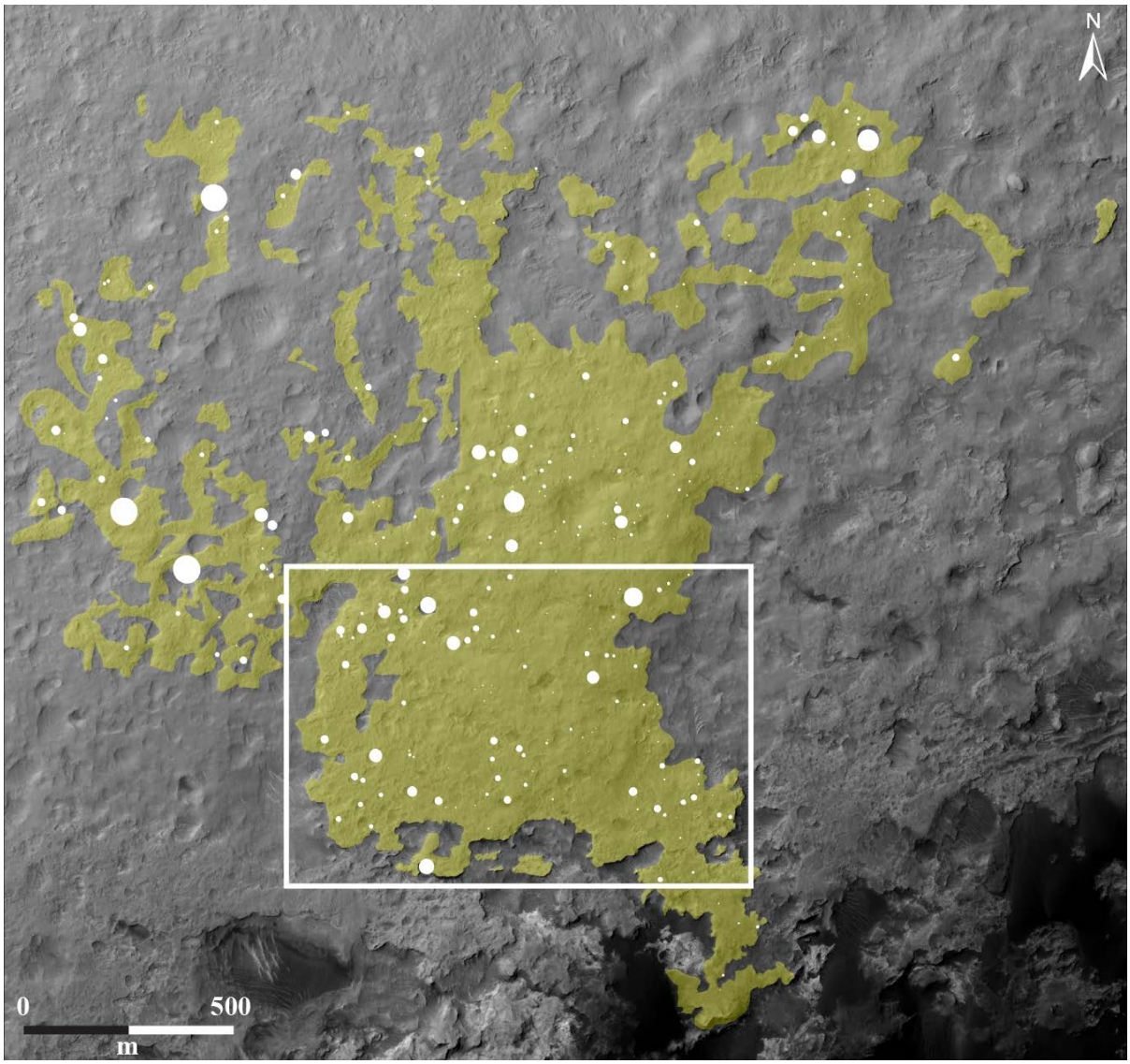

Figure 2.17: Areal extent and crater distribution of CS_Bedded1. The white box shows the location of figure 2.18.

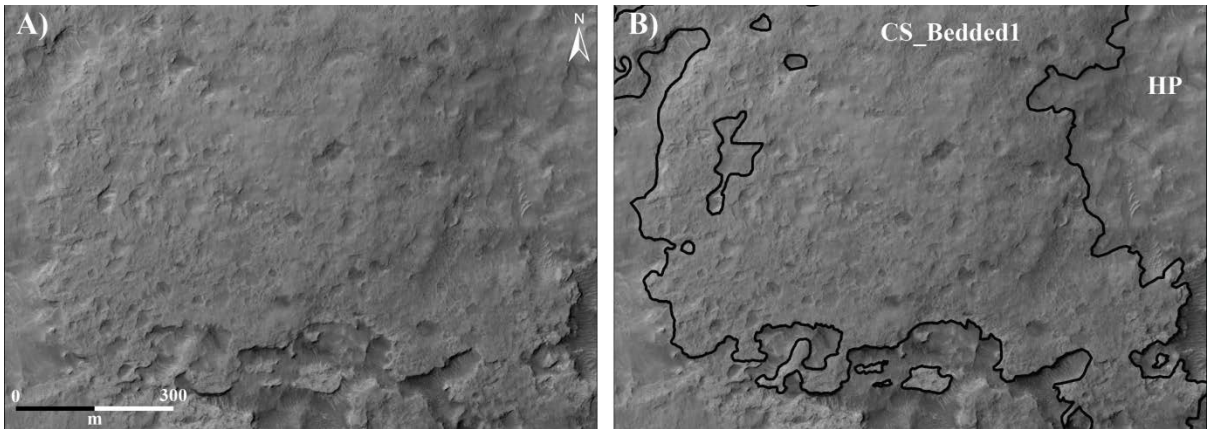

Figure 2.18: Unannotated (A) and annotated (B) portions of HiRISE image ESP_029034_1750 showing a portion of CS_Bedded1.

The walls of Hidden Valley were extensively imaged by Curiosity and are characterized by fine-grained, resistant, scarp-forming outcrops and consist of both massive and layered lithologies. The walls of Hidden Valley can be divided into multiple layered and stratigraphically distinct sections based on variations in the bedding characteristics (Fig. 2.19). The southeast wall of Hidden Valley can be divided in to multiple textural sections that can be characterized as either bedded or massive (Fig. 2.19). The very bottom of the scarp is characterized by a section made of light-toned, fine grained, platy material (section A). Section A is not considered to be part of the CS_Bedded1 deposit.

The first CS_Bedded1 section is made of dark, fine grained, very finely bedded material (section B). The next section is made of dark toned, massive material (section C). This section does not have any bedding, but does have vertical cracks. At the top of the Hidden Valley wall is another dark, fine grained section with very fine bedding (section D). Moving southeast along the base of the scarp, section A is only visible for a few meters. The rest of section A is covered by talus from the upper sections. The contact between section A and B is also partially obscured by the talus. Sections B, C, and D are made of similar dark toned, fine grained material, making the division of these sections difficult at times. Some of these different textural sections can also be seen in the northwest wall of Hidden Valley. Sections B, C, and D have the same physical features as the sections defined on the southeast wall. The complexity of the Hidden Valley walls was not evident from the mapping of surface textures in the HiRISE basemap.

Figure 2.19: The SE wall of Hidden Valley. Bottom Mastcam image, which is a subset of the top Mastcam image, shows the stratigraphically distinct bedding variations. The cartoon on the right shows the various types of bedding in the ~3 m wall of Hidden Valley.

2.1.5 CS_Bedded2

CS_Bedded2 (Fig. 2.20) is also located along the southern boundary of the landing ellipse, west of CS_Bedded1. The southwest portion of CS_Bedded2 extends out of the Curiosity landing ellipse. CS_Bedded2 is made up of one large exposure and numerous small exposures with a total combined area of ~8.6 km^2. This sub-unit is the only CS sub-unit with a noticeable average slope, which ranges from ~3 - 5° down to the west. CS_Bedded2 has a thickness of ~1 m.

The northern edge of CS_Bedded2 is in contact with the HP unit, and has a consistent light albedo; it has a very similar albedo as the HP unit making the contact nearly indistinguishable. There is little to no erosional scarp along the CS_Bedded2 and HP unit contact (Fig. 2.21). Once again, the increased abundance of craters is the main factor in determining the contact between CS_Bedded2 and the HP unit. The southern edge of CS_Bedded2 has a slightly darker albedo than the northern portion. The albedo for the southern edge is consistent, giving it a smooth surface appearance. The southern boundary is distinguished by an erosional scarp that can be 1 – 8 m in height (Fig. 2.21). To the south, CS_Bedded2 is in contact with the lower units of Mt. Sharp.

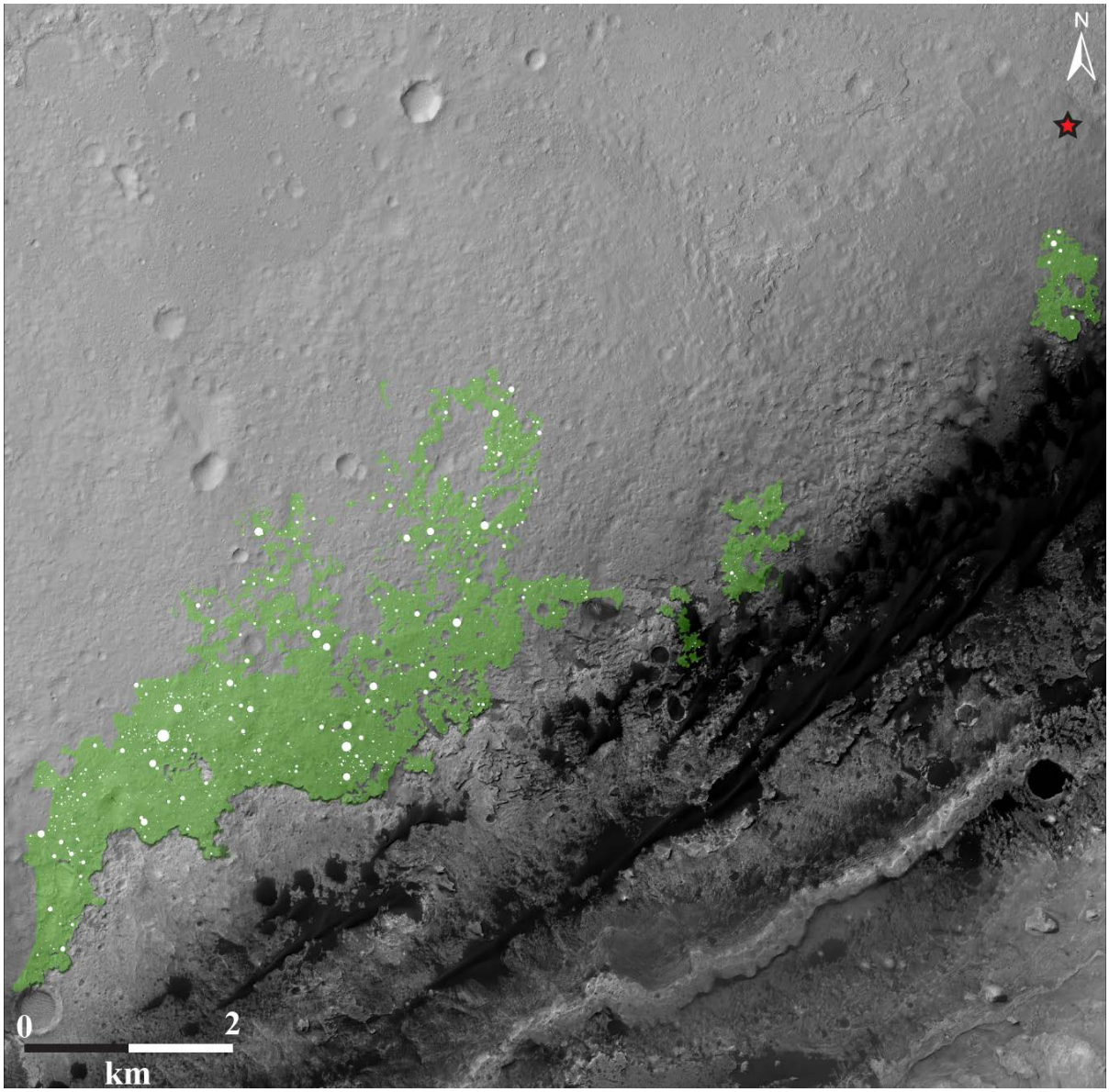

Figure 2.20: Areal extent and crater distribution of CS_Bedded2. The red star shows the location of the Curiosity landing site. White box shows the location of figure 2.21.

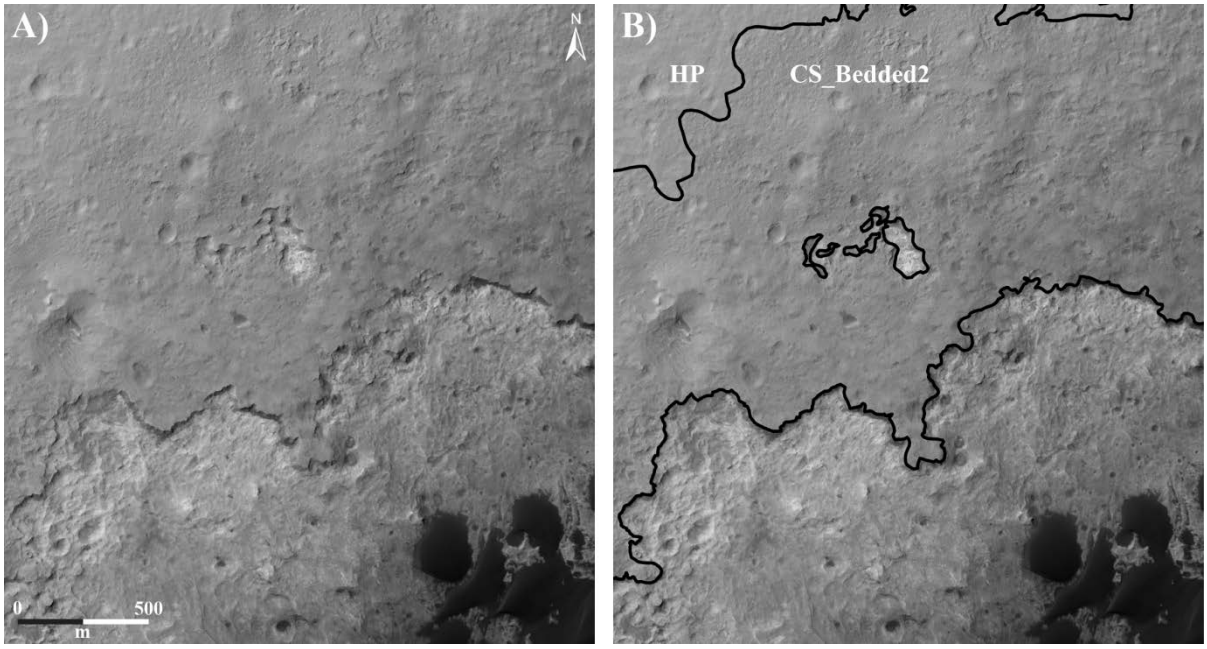

Figure 2.21: Unannotated (A) and annotated (B) portions of HiRISE image ESP_018920_1755 showing a portion of CS_Bedded2.

Curiosity has only imaged a small mesa of CS_Bedded2 at the southern end of Hidden Valley, from a distance of ~140 m (Fig. 2.22). The images show southeast dipping beds ~60 cm in length. At such a large distance, it is difficult to say much about the physical characteristics of the CS_Bedded2 outcrop. The planned traverse for Curiosity will hopefully allow for imaging of CS_Bedded2 at a closer distance on the way up Mt. Sharp.


Figure 2.22: View to the southwest of CS_Bedded2 at the south end of Hidden Valley. In this image the red lines trace the southeast-dipping beds.

2.1.6 Summary of Sub-Units

The sub-units discussed above were all initially mapped as part of the CS mainly due to their ability to retain impact craters. In HiRISE images, all of the CS sub-units can be characterized as resistant, mesa forming, crater retaining surfaces. These surface similarities suggest that all five sub-units were originally one laterally extensive unit. However, the variations in albedo (consistent vs. mottled), surface morphology (rough vs. smooth) and crater density suggest otherwise, that the five sub-units are not portions of one extensive unit, but are indeed five separate units. The same story is seen in the Mastcam images, where all five sub-units appear to be made of the same fine grained, resistant material; however, there are differences such as fine grained bedded deposits vs. fine grained massive deposits. These textural differences suggest different emplacement stories for the various CS sub-units.

Table 2: Physical characteristics of the five CS sub-units as seen in HiRISE and Mastcam images.

Sub-unit (Area km^2)	Location	Slope	Erosional Scarp	Surrounding units	Albedo/Surface Morphology (as seen in HiRISE images)	Lithology (as seen in Mastcam images)
CS_Flat (4.4)	E of Bradbury Landing site: Eastern tip of landing ellipse	~1° down to N	Yes along North contact with BF unit, no along West and South contact with HP unit	BF to the North and HP to the West and South	Consistent tone/Smooth surface	Massive/Layered
CS_Infill1 (5.5)	W of Bradbury Landing site: Center of landing ellipse	Horizontal	Yes along entire contact with HP unit	HP	Mottled tone/Rough surface	Massive
CS_Infill2 (7.7)	W of Bradbury Landing site: Western tip of landing ellipse	~1° down to N	Minimal scarp	Mostly HP	Consistent tone/Smooth surface	Not visited by Curiosity
CS_Bedded1 (0.34)	SW of Bradbury Landing site: Southern edge of landing ellipse	~1° down to N	Prominent scarp along southern boundary smaller scarp outlining the remainder of the exposure	HP along northern contact, lower Mt. Sharp units to the south	Mottled tone/Hummocky surface	Massive/Very Fine Bedding
CS_Bedded2 (8.6)	SW of Bradbury Landing site: Exposures lie partially outside of landing ellipse	3-5° down to W	Prominent scarp along southern boundary smaller scarp outlining the remainder of the exposure	HP along northern contact; lower Mt. Sharp units to the south	**Consistent** light tone for northern portion of exposure **Consistent** darker tone for southern portion of exposure **Smooth** surface throughout the exposure	Layered

2.2 Comparison of CS Sub-Units and Geomorphic Features of Terrestrial Deposits

To summarize, the CS is a thin, fine-grained unit that retains a high number of small impact craters, all suggesting that the CS is the most erosionally resistant unit in the Curiosity landing ellipse. These characteristics are useful for mapping the boundaries of the CS exposures in HiRISE images. However, the characteristics are common to multiple rock types, which means that it is extremely difficult to conclusively determine a single emplacement mechanism for the individual CS sub-units, based on the data available. The physical characteristics are consistent with rocks that on Earth are emplaced by a variety of different fall or flow processes, as will be discussed below. The descriptions below will compare the features of all five CS sub-units, as seen in HiRISE and Mastcam images, to the terrestrial processes described in section 1.6 of the introduction chapter.

2.2.1 CS_Flat

In the HiRISE images, the CS_Flat exposures have a planar, nearly horizontal upper surface. The slope of CS_Flat, ~1° down to the N, suggests that the CS_Flat material came from the direction of Mt. Sharp. The planar surface of CS_Flat is indicative of a geologic process that forms an equipotential surface, either during or after emplacement. Additionally, because the pre-existing topography of the BF unit has a very gradual slope, the CS_Flat material must've had a sufficiently low viscosity such that it could flow across nearly horizontal pre-existing surfaces. However, because the CS_Flat material is not seen on the eastern slopes of the HP unit, Bradbury Rise, the formation mechanism must not have had sufficient energy to push the CS_Flat material up the eastern slope of Bradbury Rise. There are two types of geologic processes that have similar geomorphic characteristics as CS_Flat, 1) a low viscosity pāhoehoe lava flow and 2) a low-energy subaqueous sediment flow.

Pāhoehoe lava flows have the ability to flow across pre-existing slopes of <2° (Hon et al., 1994a). However, because pāhoehoe lava flows are low-energy geologic processes, they do

not have enough energy to cover topographic highs. Instead pāhoehoe lava flows pond in topographic lows and against the banks of topographic highs, resulting in a nearly horizontal surface. These attributes of pāhoehoe lava flows could explain the stratigraphic relationships between the CS_Flat, HP, and BF units, seen at the intersection point of the three units near Yellowknife Bay.

The massive nature of the CS_Flat float rocks seen in Mastcam images, and the thickness of the CS_Flat exposure measured in HiRISE images, indicate the pāhoehoe lava flow would have experienced inflation after deposition. Pāhoehoe lava flows are typically 10s of centimeters thick and can inflate to be a few meters thick (Hon et al., 1994a). Inflated pāhoehoe flows tend to be massive because some of the trapped volatiles have sufficient time to escape the lava before it completely solidifies. However, not all of the volatiles will necessarily escape the lava flow. Aeolian erosion tends to highlight vesicularity differences in a lava flow and form volcanic ventifacts, which have a layered appearance. The layered textures seen in the CS_Flat outcrop could be the result of erosion by aeolian abrasion. Ventifact features have been identified in the Curiosity landing ellipse (Bridges et al., 2014).

A planar surface and ability to flow across a gradual pre-existing slope are not however, exclusive features of a pāhoehoe lava flow. There are numerous fluvial and lacustrine depositional environments that produce horizontally layered deposits. The distinct cross-bedding seen in the lower facies of the Shaler outcrop are interpreted to have been deposited in a high-energy fluvial environment (Anderson et al., 2014; Grotzinger et al., 2014). However, the distinct cross-bedding is not seen extending into the CS_Flat (originally facies 7) deposits. This would indicate that the CS_Flat deposits were formed under a lower-energy fluvial environment compared to the lower facies of Shaler. This is in line with the absence of CS_flat material on the topographically higher slopes of Bradbury Rise, which indicates CS_Flat formed in a low-energy environment.

2.2.2 CS_Infill1 and CS_Infill2

Geomorphic, spatial, and stratigraphic relationships allow us to constrain the emplacement mechanism of the CS_Infill1 and CS_Infill2 sub-units. The physical

relationships, described below, suggest a depositional mechanism involving low-energy lateral flow as the likely origin of the CS_Infill sub-units. Evidence for this comes from areas where the deposits surround and partially fill large, pre-existing impact craters. In both instances, the crater rims were not completely buried by, and stand 1 - 3 m above the CS_Infill sub-units. One example, in CS_Infill1, is located near the center of the Curiosity landing ellipse, ~1800 m SW of the Bradbury landing site (Fig. 2.23). Here, slightly more than half of the southern ~350 m-wide crater rim, consisting of HP material, forms a concave-northward arc that stands 1 - 3 m above the surrounding surface of essentially horizontal CS_Infill1. Where the northern portion of the rim is inferred to have been appears to have eroded away and its location is now covered by the top CS_Infill1 layer. The interior of the crater is partially filled by material from the top CS_Infill1 layer, and it appears that a small amount of CS_Infill1 flowed south through a low spot in the southern crater rim. CS_Infill1 material has surrounded the outside of the topographically higher east and west portions of the impact crater, and flowed over the pre-existing HP unit. Therefore, the pre-existing impact crater is surrounded by CS_Infill1 material on the north, east, and west sides.

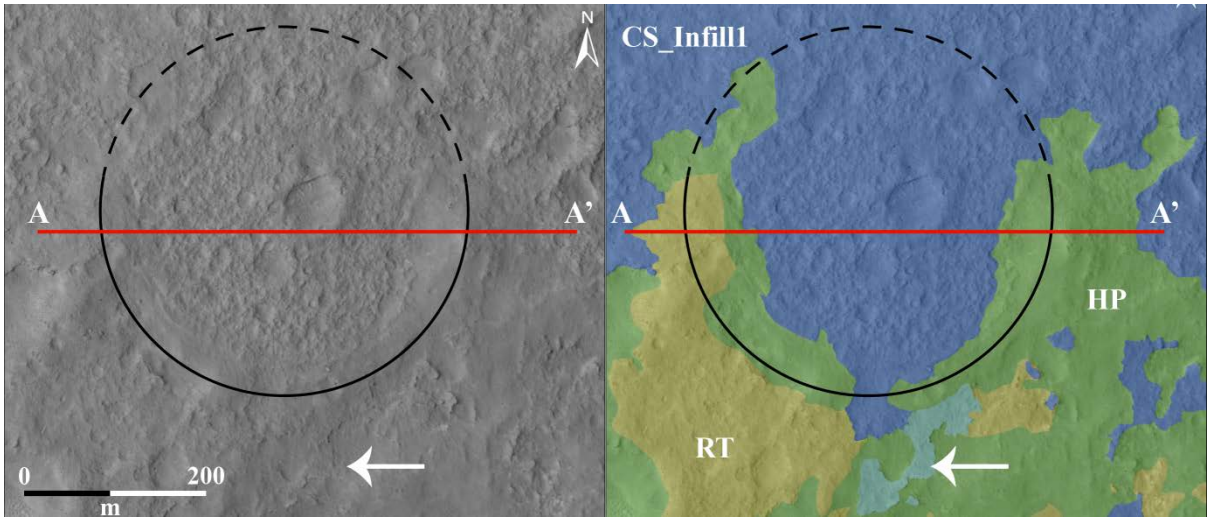

Figure 2.23: Portion of HiRISE image ESP_018854_1755, showing a crater (the rim is outlined in black) that has been partially filled by CS_Infill1 (blue). The highest part of the rim is 1-3 m above the nearly horizontal surface of CS_Infill1 that was deposited inside the crater. Note that some of CS_Infill1 extends beyond the southern portion of the crater rim. The red line shows the location of the cross section in figure 2.25.

A similar situation is located in the NW corner of the Curiosity landing ellipse, at coordinates 137° 16' E and 4° 34' S (Fig. 2.24). At this location, a crater ~517 m in diameter has been partially filled by CS_Infill2. Here, the crater is interpreted to have formed in the RT unit before both the HP and CS_Infill2 units were deposited. There is little evidence of a rim along the SE quadrant of the crater, coinciding with the HP and CS_Infill2 units. The northern half of the crater rim is still visible in the topography of the RT. The crater floor was most likely initially covered by the HP unit and later covered again by CS_Infill2. The NW portion of the crater rim stands ~5 m higher than the CS_Infill2 deposit on the crater floor. The eastern portion of the crater appears to be significantly eroded and the southern portion of the crater rim has completely eroded away.

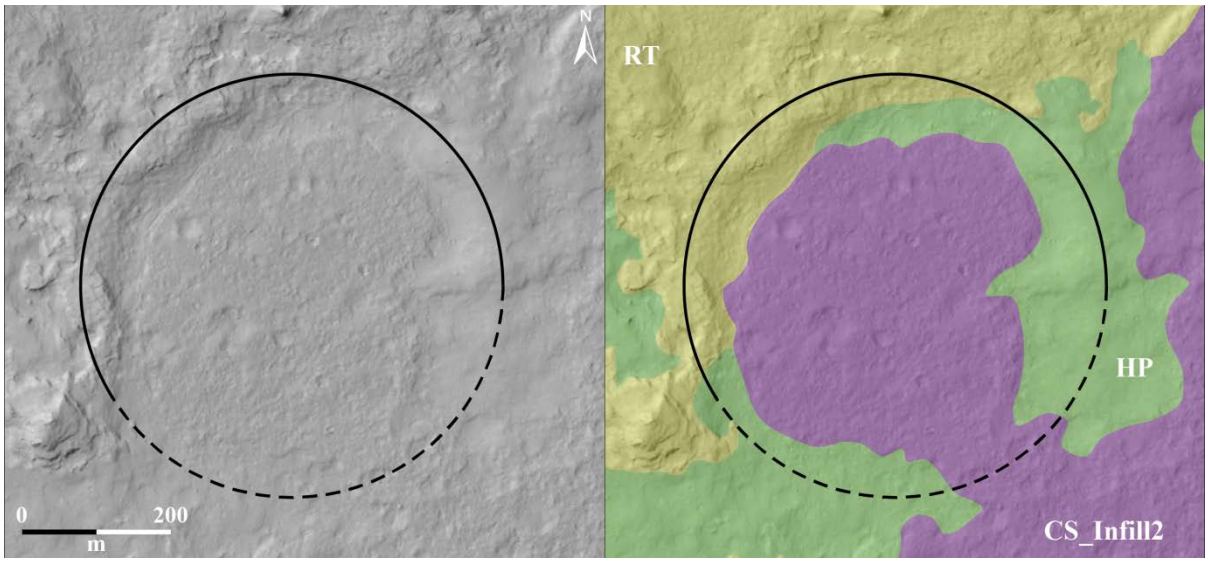

Figure 2.24: A crater ~517 m in diameter that is partially filled by CS_Infill2 (purple). In this case, the filled crater was most likely formed in the RT before the CS_Infill2 sub-unit was deposited. The NW portion of the crater rim is ~5 m higher than the portion of the crater rim that is now covered (dashed line) by CS_Infill2.

There are two scenarios that could produce the stratigraphic relationships seen at the two locations described above: 1) the pre-existing impact crater was completely buried by the CS_Infill material, or 2) the pre-existing impact crater was only ever partially filled and surrounded by the CS_Infill material. Scenario 1 (Figs. 2.25b, and 2.26) indicates that after the impact crater formed, the CS_Infill material was deposited, either subaqueously or subaerially, to a point that the impact crater was completely buried. Erosion would then have

stripped away the CS_Infill material down to the present surface, leaving the rim of the impact crater topographically higher than the remaining CS_Infill material. In this scenario, the crater rim was once completely buried by the CS_Infill material, and was exposed due to erosion, meaning the present day surface is an erosional surface. The second scenario (Figs. 2.25c and 2.27) is that the CS_Infill material was emplaced laterally into the pre-existing impact crater via low points of the crater rim. However, the CS_Infill material never completely buried the topographically higher portions of the pre-existing impact crater rim.

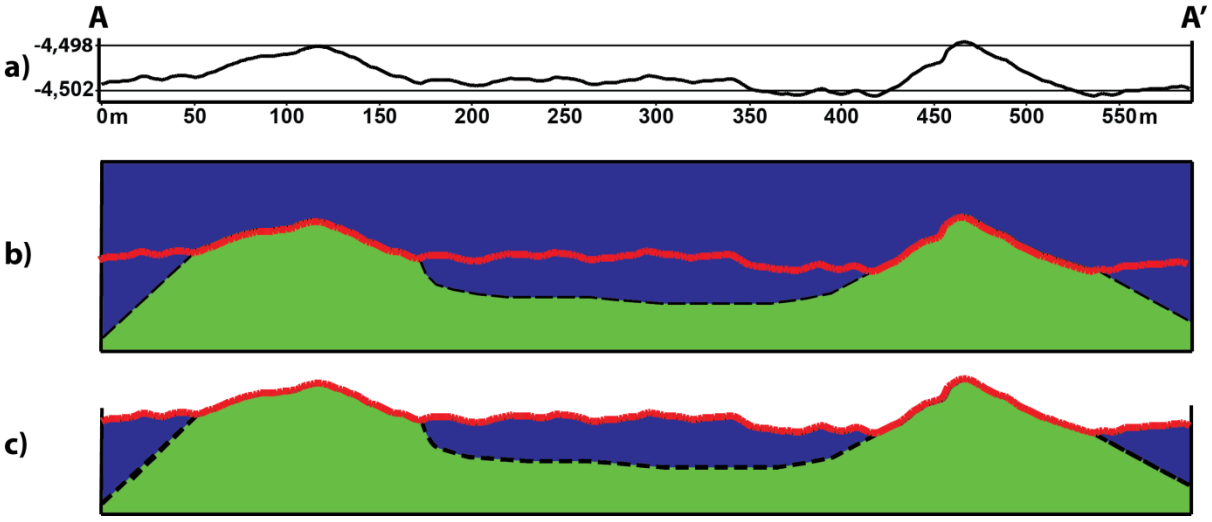

Figure 2.25a: Topographic profile (5x vertical exaggeration) of the present day surface (see location of profile in figure 2.23). 2.25b: Scenario 1 where the CS_Infill1 (blue) completely buried the pre-existing impact crater in the HP unit (green). Red line represents the present day topography. 2.25c: Scenario 2 where the CS_Infill1 only partially filled the crater and surrounded the topographically higher but stratigraphically lower HP crater rim. The true thickness of each unit is unknown.

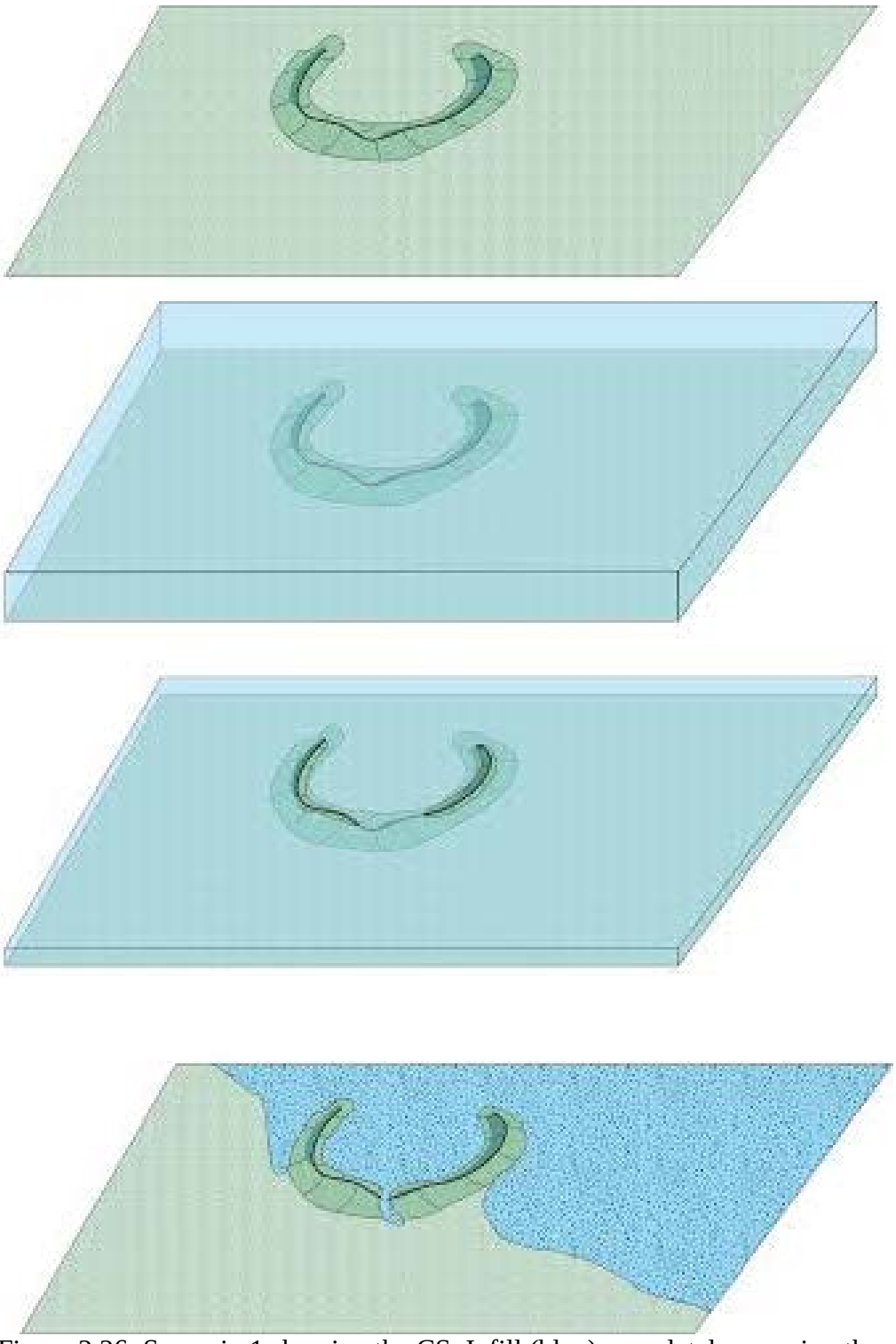

Figure 2.26: Scenario 1 showing the CS_Infill (blue) completely covering the pre-existing impact crater (green).

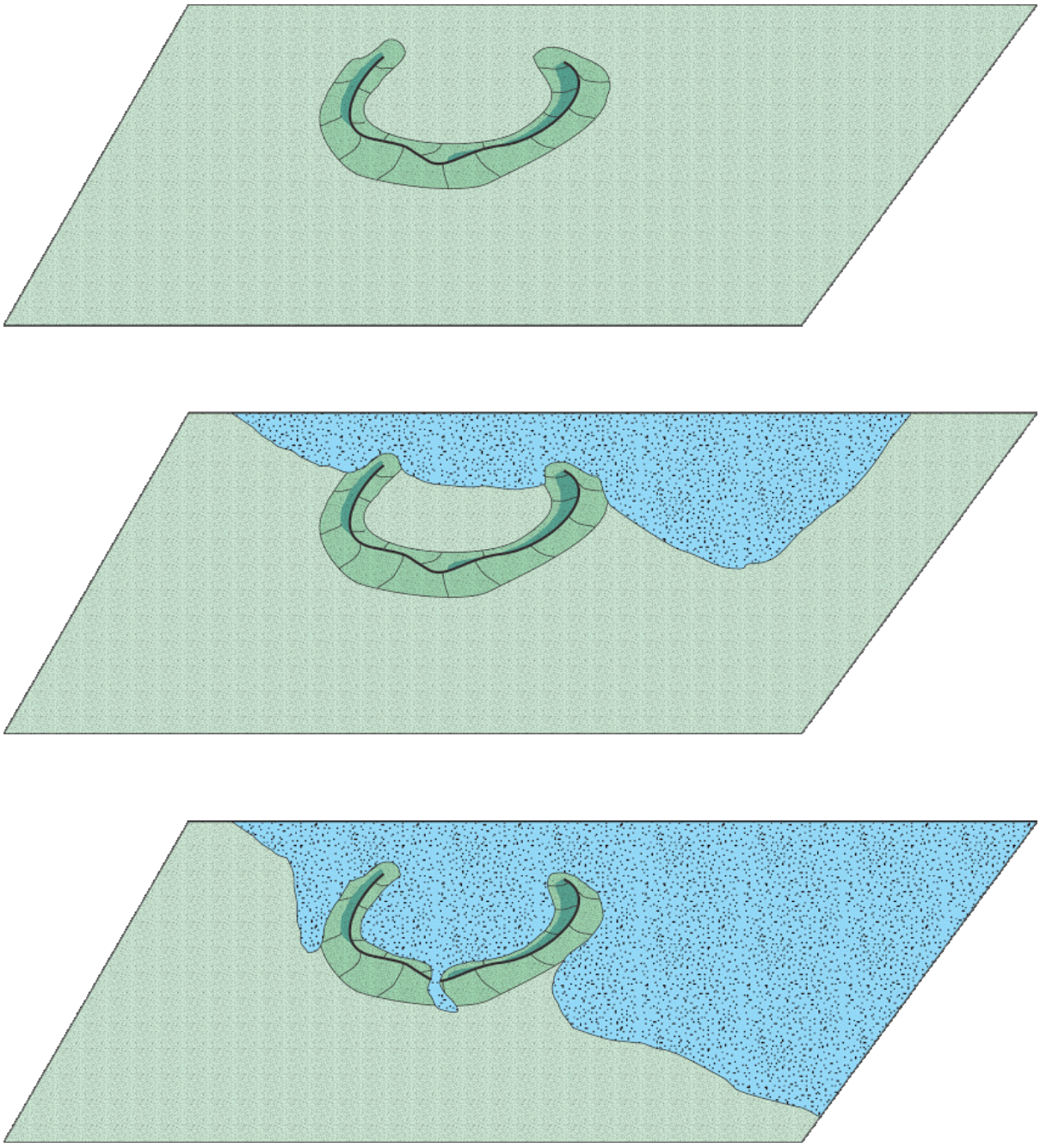

Figure 2.27: Scenario 2 showing the CS_Infill (blue) only partially filling and surrounding the pre-existing impact crater (green).

The key observation that causes the first scenario to be least plausible, is that the rim of the pre-existing impact crater consists of the less erosionally resistant unit (HP or RT+HP), yet the rim is topographically higher than the more erosionally resistant CS_Infill material. If the CS_Infill material once completely buried the impact crater rim, the present

topographic relationships would require that the CS_Infill material was preferentially eroded. This scenario is not plausible as it cannot explain why an erosionally-resistant, crater-retaining unit (CS_Infill) would experience more erosion than the less resistant units (HP and RT). If the impact crater was completely buried it would be expected that the crater rim would have been eroded to an equal or lower topographic level than the CS_Infill material (Fig. 2.28). That is, the CS_Infill material and the less resistant HP or RT units, would have experienced similar amounts of erosion.

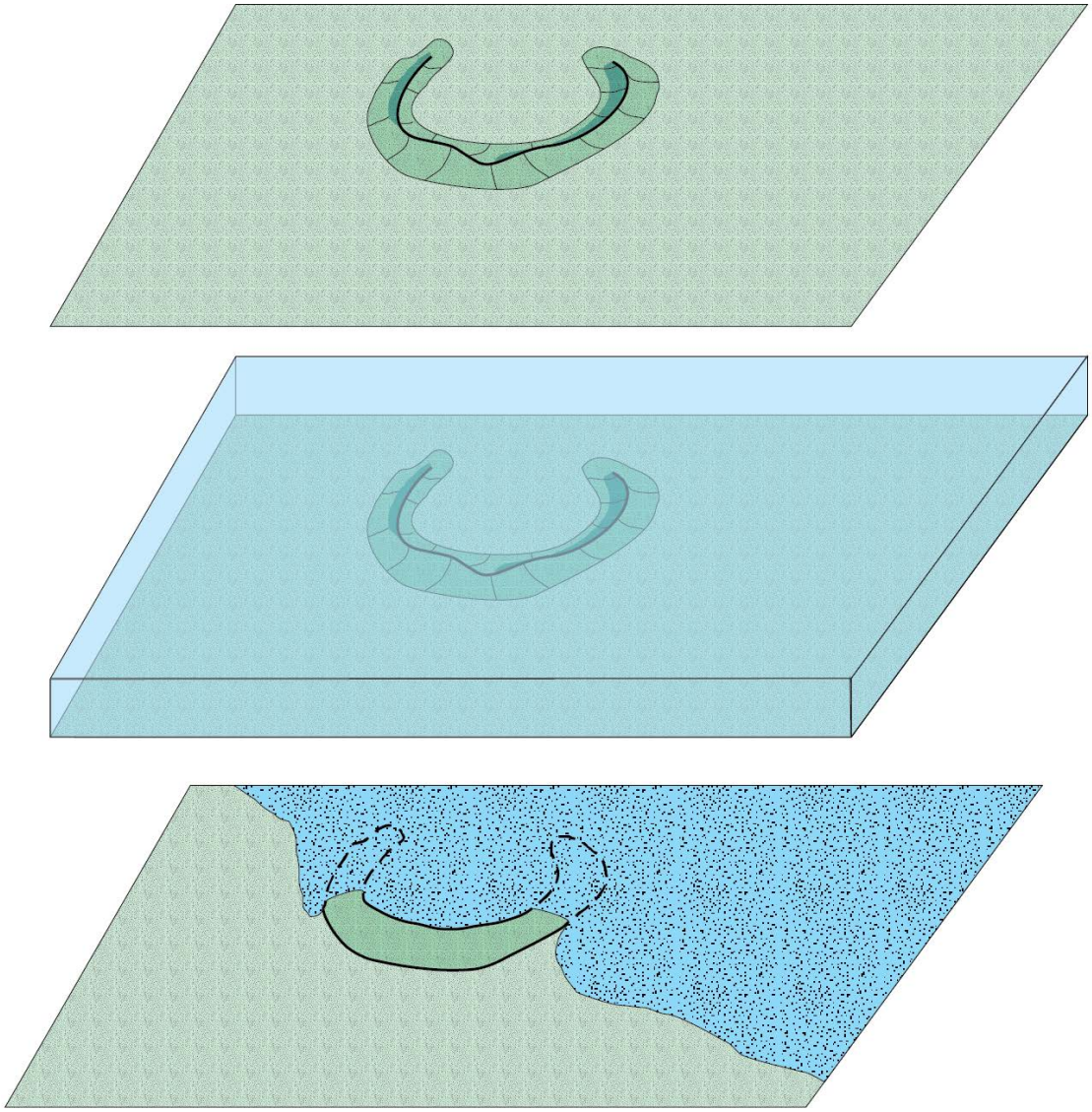

Figure 2.28: Cartoon showing the expected topographic relationships of the CS_Infill (blue) material and the pre-existing crater rim (green), if the crater was once completely buried by the CS_Infill material.

Scenario 2 is favored because it does not require the more erosionally resistant CS_Infill material to be preferentially eroded over the less resistant HP or RT units. If the CS_Infill material never completely buried the crater rim, the present day surface represents the true depositional surface of the CS_Infill sub-units. Assuming scenario 2 is correct, it can be concluded that the CS_Infill sub-units were deposited laterally. More specifically, the CS_Infill sub-units were deposited by a low-energy lateral process. This is evident by the fact that the crater rims were not completely buried yet provided only minimal topographic barriers (2 - 5 m height with very gradual slopes). A highly energetic process can be ruled out because any type of rapid lateral depositional process would have sloshed over such minimal topographic features.

From the locations described above it is possible to infer direction of origin. The rim of the impact crater filled by the top CS_Infill1 layer was probably topographically lower to the north, as it is today. This would have allowed CS_Infill1 material to flow into and partially fill the crater from the north. Additionally, CS_Infill1 material appears to have flowed out of a low place on the south portion of the crater rim. These observations suggest that CS_Infill1 was emplaced from north to south, at this specific location.

The rim of the crater filled by CS_Infill2 is topographically lower to the southeast. The crater rim was likely eroded before CS_Infill2 was deposited, allowing the material to flow into and pond in the crater. The flow direction of CS_Infill2 indicated at this location would have been from the southeast to northwest.

The planar surface and isolation of pre-existing topographic highs, suggests that CS_Infill1 and CS_Infill2 formed under a low-energy depositional environment. Similar to CS_Flat, there are two types of geologic processes that have the necessary geomorphic characteristics to be comparable to the CS_Infill deposits. These are 1) a low viscosity pāhoehoe lava flow and 2) a low-energy subaqueous sediment flow.

Because pāhoehoe lava flows are low-energy geologic processes, they do not have enough energy to bury topographic highs, resulting in the isolation of pre-existing topographic highs. The impact crater rims, which are only 1 - 3 m higher than the CS_Infill

deposits, acted as a barrier and inhibited the flow from advancing; this is why the pre-existing impact craters were never completely buried. The CS_Infill1 deposit imaged at the Darwin waypoint was only represented by massive float rocks. The CS_Infill2 deposits will not be imaged by Curiosity. The massive nature of the CS_Infill1 float rocks seen in Mastcam images, and the thickness of the CS_Infill1 exposure measured in HiRISE images, again indicate the possibility of an inflated pāhoehoe flow as the depositional environment for CS_Infill1. The layers identified in the CS_Infill1 exposures, could represent multiple inflated pāhoehoe lava flows stacked on top of one another.

However, there are also numerous fluvial and lacustrine depositional environments that could explain the geomorphic characteristics of the CS_Infill deposits. Although the one CS_Infill1 float rock imaged by the RMI did not have grains larger than the resolution limit of the camera, the similarities with the CS_Flat float rocks suggest the CS_Infill material could also be sandstone.

Although the topographic relationships of the CS_Flat, CS_Infill1, and CS_Infill2 sub-units with the underlying units and the geomorphic characteristics of the deposits could have resulted from a pāhoehoe lava flow that mantled the gradual pre-existing topography and ponded in topographic lows, there is one major caveat to this hypothesis. There has been no volcanic source identified within Gale Crater. It is possible that the source vent has been completely eroded away, as pāhoehoe lava flows near the source are more easily eroded than the downslope lava flows.

2.2.3 CS_Bedded1

The CS_Bedded1 deposits as seen in the walls of Hidden Valley are characterized by interbedded textures of very fine horizontal bedding (sections B and D in Fig. 2.19) and massive sections (section C). The very fine bedding is indicative of multiple fluvial and lacustrine environments. One such fluvial mechanism could be a delta. In a deltaic environment, the delta front advances through the pre-existing body of water forcing the water to laterally prograde in the opposite direction of the incoming sediment and increase in depth. The delta front includes the gradually sloping topsets, the steeply dipping foresets,

and the nearly horizontal bottomsets (Fig. 1.14). As the depth of the pre-existing water increases, there is more room for sediment to be deposited forming additional layers, parallel to the previously deposited deltaic layers. The horizontal beds of the CS_Bedded1 deposit could represent the topsets of a delta front. The massive section C, seen in the SE wall of Hidden Valley could represent a mudstone interbedded with a delta front.

2.1.4 CS_Bedded2

CS_Bedded2 seen at the south end of Hidden Valley (Fig. 2.22) is comprised of southeast dipping beds. The southeast dipping geometry combined with the increasing elevation of the beds requires a depositional mechanism that could deposit sediment into a standing body of water (Fig. 2.29). One such mechanism could again be a delta. In this case, the inclined beds of CS_Bedded2 would represent the steeply dipping foresets of a deltaic front (Fig. 1.14). As the depth of the pre-existing water increases, there is more room for sediment to be deposited forming additional layers, parallel to the previously deposited deltaic layers.

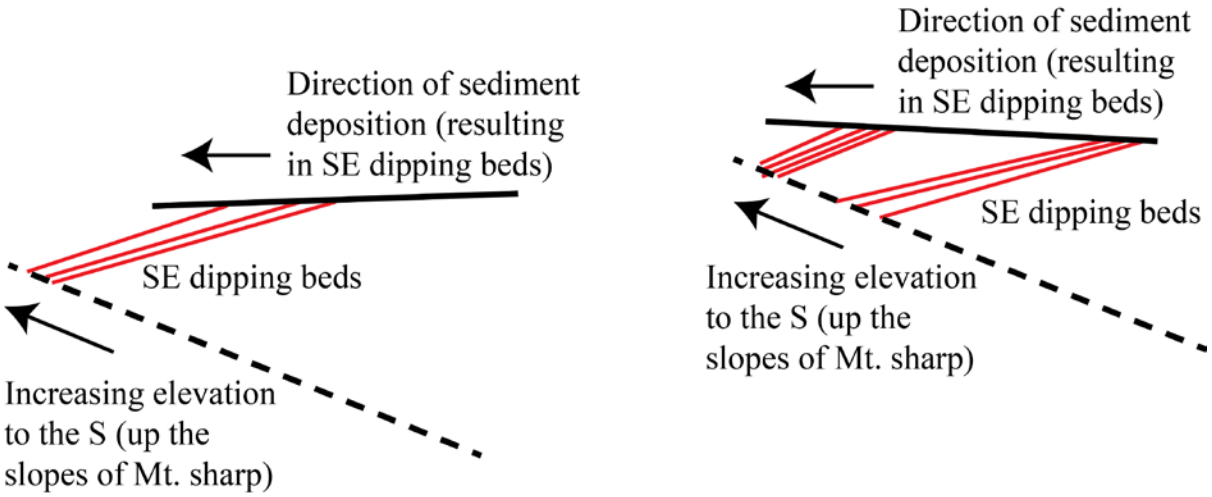

Fig. 2.29: Cartoon showing the topographic relationships of the southeast dipping beds of CS_Bedded2 and the pre-existing topography.

Whereas the Mastcam images used to infer the texture of the CS_Bedded2 beds were taken at a distance, the inclined beds appear to be made of similar fine-grained, resistant material as that seen in the walls of Hidden Valley. The distance the Mastcam images were taken at precludes making inferences about the sorting or grading of the grains in the

CS_Bedded2 deposit. This in turn inhibits any further classification about the type of delta that may have deposited the CS_Bedded2 material. One caveat to this theory is that there have not been any corresponding topsets or bottomsets identified, with the appropriate orientation, to match the inclined beds of CS_Bedded2. The inclined beds appear to be terminated by a single erosional bounding surface, which is actually more common to aeolian deposits.

Many studies have successfully determined that aeolian processes are presently active in Gale Crater and have likely contributed to the erosion of the landing ellipse units (Hobbs et al., 2010; Silvestro et al., 2013; Bridges et al., 2014). The increasing elevation of the inclined beds of the CS_Bedded2 requires a strong enough wind regime flowing from north to south to have pushed the fine-grained material up the slopes of Mt. Sharp. The CS_Bedded2 deposits consist of nearly horizontal first order bounding surfaces (white lines in Fig. 2.22) and inclined second order bounding surfaces (red lines in Fig. 2.22; Brookfield, 1977; Kocurek, 1981). The second order bounding surfaces are likely made of climbing-ripple structures (Hunter, 1977). Further classification of the type of dune structures is inhibited due to the distance from which the Mastcam image of the CS_Bedded2 outcrop was taken (~140 m). The active Bagnold dune field provides a modern day Martian analog that proves the wind regime in Gale Crater is indeed strong enough to have deposited fine-grained material up the slopes of Mt. Sharp.

Chapter 3

Crater density as an aid to understanding substrate resistance to erosion on Mars

Abstract

The objective of this chapter is to show how crater counting can be used as a mapping tool to understand the erosional history of geologic units observed from orbit, specifically some of the units in the MSL Curiosity rover landing ellipse in Gale Crater, Mars. The crater density (# craters per km^2) of the CS was compared to the crater densities of the HP and BF units to determine the erosional resistance and relative stratigraphic position of the CS. It was determined that the CS has the highest density of small craters, but the lowest density of large craters. This indicates that the CS is the youngest, but most erosionally resistant unit in the Curiosity landing ellipse. The subdivisions of the CS are also supported by the relative crater densities of the sub-units. The crater densities of the CS sub-units provide additional evidence that the sub-units likely represent different and discrete geologic units. This chapter explores a unique opportunity to compare the physical properties of the geologic units observed from orbit and rover images. Using Mastcam images from Curiosity, the physical properties of the three main landing ellipse units such as grain size and weathering pattern, were compared to gain a better understanding of how target rock properties allow a particular unit to retain a higher density of craters.

3.1 Introduction

All rocky planetary bodies in the solar system have experienced impact cratering. The rate of the cratering process has been determined to be different, and varied throughout the history of each individual planetary body (Michel and Morbidelli, 2013). Impact cratering can therefore be used as a chronometer to help decipher the geologic history of a planetary surface. The abundant sample set of Apollo lunar rocks allowed for calibration of the crater

density of a geologic landscape to the absolute age of the sample from that particular location (Hartmann, 1966, 2005). In the absence of returned samples from known locations on Mars, crater densities are the main tool available to calculate the crater retention age of a geologic formation exposed at the surface. However, using the lunar crater to age calibration and accounting for atmospheric and gravitational differences, a Mars/Moon cratering ratio can be calculated. This ratio also assumes that the size distribution and time dependence of impactors are the same on Mars as they are on the Moon (Hartmann, 2005). The resulting Mars crater density calibration factor has allowed scientists to place age constraints on the major time periods of the Martian geologic timescale (Fig. 1.2; Tanaka, 1986; Hartmann and Neukum, 2001; Carr and Head, 2010).

The ages determined from the crater densities represent crater retention ages of the surfaces. Hartmann (1966) defined the crater retention age as the amount of time a crater of a particular diameter can be retained by the target surface. The crater retention age represents either the minimum age for the deposition of a geologic formation or the age of the last resurfacing event.

There are a number of factors that complicate the process of calibrating crater density to an absolute age. These include the proper identification of sub-km impact craters as primary or secondary craters, the physical characteristics of the target material that enables retention of impact craters, and active geologic processes that can completely or partially bury, erode, or exhume impact craters (McEwen et al., 2005a; Malin et al., 2006; Hartmann, 2007).

3.1.1 Small Craters: Primary or Secondary?

Over the past decade, the availability of decameter-scale resolution image datasets has enabled systematic observations of, and scientific investigations using, meter-scale impact craters (Malin et al., 2006; Hartmann, 2007; Daubar et al., 2013). This has both enhanced and complicated crater age dating. Crater age dating, for relative or absolute age determination, is based on the assumption that every crater identified is a primary crater. Therefore, to accurately calculate the crater retention age of a geologic feature, it must be determined whether sub-km impact craters are primary or secondary craters. It is the change in flux of primary craters, those created by collision of interplanetary bodies, through

geologic time that allows crater-counting to be used for age-dating (Hartmann, 2005). In contrast, secondary craters are created by fall-back debris ejected from the surface by the impact that formed the associated larger primary craters. Secondary craters therefore are not directly related to the flux of impactors in the solar system and thus contaminate the calculated crater chronometer (McEwen and Bierhaus, 2006).

It is sometimes difficult to identify a small crater as either a large secondary crater or a small primary crater. Obvious secondary craters typically have a sharp rim, asymmetric shape, and bright ejecta (McEwen et al., 2005b; McEwen and Bierhaus, 2006). This type of craters are found closer to the primary crater and are often found in clusters of multiple small craters or lie in the path of the bright rays of the large primary crater. It is these secondary craters that are often easily excluded from crater counts. However, as you get farther from the primary crater, the secondary craters become more symmetrical in shape and are harder to identify as secondary craters. It is difficult to know for certain whether a dataset has excluded all the possible secondary craters, which is why Hartmann (2007) stresses the fact that the crater retention age system he has developed is based on the total number of craters in each size bin, including obvious primary craters and the indistinguishable secondary craters.

Because of the complications that arise from using sub-km craters for age dating typically only larger craters, $D > 1$ km, are included in the crater dataset. However, employing the traditional methods of relative crater age dating is challenging for meter to kilometer-scale geologic/geomorphic features. Smaller geologic features, such as alluvial fans, deltas, and small lava flows, that have a surface area of only a few km squared only retain small, sub-km impact craters. It is these small features, however, that are thought to represent the geologic surface processes that occurred in Mars' recent geologic history. It is therefore crucial to understand how to predict an accurate absolute age using small, primary or secondary, craters.

Substantial debate in the planetary community over the past decade has centered on the identification of small, sub-km, craters as either primary or secondary and the statistical validity of using these small craters to date a geologic feature. McEwen et al. (2005a) stated

that sub-km craters observed on the surface of Mars are predominantly secondary craters, and therefore cannot be used to determine the age of a surface or geologic unit. Hartmann (2005, 2007), however, stated that it is vital to determine the production rate of small craters (primary or randomly scattered secondary craters) because Mars' recent geologic history, last 10 Ma, is expressed by kilometer-scale features that only retain sub-km craters. Hartmann (2005) also concluded that the isochrons he calculated for the lunar and martian surfaces are based on the density of background secondary craters and small primary craters. The background secondary craters are defined as those not in obvious clusters or the ray paths of larger primary craters. Therefore, Hartmann (2005, 2007) supported the use of small craters that are not obvious secondary craters, in crater density datasets used to predict the age of a geologic surface.

Both Hartmann (2005, 2007) and McEwen et al. (2005a) agreed that great caution must be used when absolute ages are inferred from craters < 100 m in diameter. Hartmann (2005) stated that the inferred age from crater counting studies that use only small craters could have an uncertainty as high as a factor of 10. Because the majority of craters used for this study are in this size range (D < 100 m), caution is required when predicting an absolute age of the various units. However, because this uncertainty should apply equally to all the units in this study, the relative ages of the units determined here are still deemed valid.

This chapter will address some of the crater counting complications discussed above by presenting a crater counting study done in Gale Crater, Mars. This study will show how small, sub-km, craters can be used to understand the relative erosional resistance of three units within the MSL Gale Crater landing site. Later, the chapter will focus on how the physical characteristics of a unit such as grain size, cementation, and overall erosional resistance affect crater retention. Mastcam images from the Curiosity rover plus the abundance of HiRISE images of Gale Crater provide a unique opportunity to investigate the connection between the surface characteristics of a geologic unit and the crater density as calculated from orbital images.

3.2 Characteristics of the Curiosity Landing Ellipse Units

3.2.1 Cratered Surface

In the geomorphic map (Fig. 1.7) made prior to Curiosity landing in Gale Crater, all surface exposures of heavily cratered terrain were lumped into a single geomorphic unit (i.e., the CS). There are three distinguishing geomorphic characteristics of all CS exposures in the landing ellipse, as seen from HiRISE images (orbital insert in Fig. 3.1). These are a high crater density (specifically increased retention of smaller diameter craters), mesa-forming erosional scarps, and a nearly horizontal surface. However, based on analysis of HiRISE images, there are subtle, but spatially contiguous differences within the CS exposures, allowing the CS to be divided into five sub-units (Fig. 2.1). These five sub-units are CS_Flat, CS_Infill1, CS_Infill2, CS_Bedded1, and CS_Bedded2. The characteristics used to subdivide the CS include albedo, surface roughness, crater density, and the erosional state of crater rims. In the Mastcam images taken by Curiosity, the CS sub-units appear to be made of similar dark, fine grained material. The in situ outcrops of the CS sub-units vary in lithology from massive to very fine bedding (Fig. 3.1).

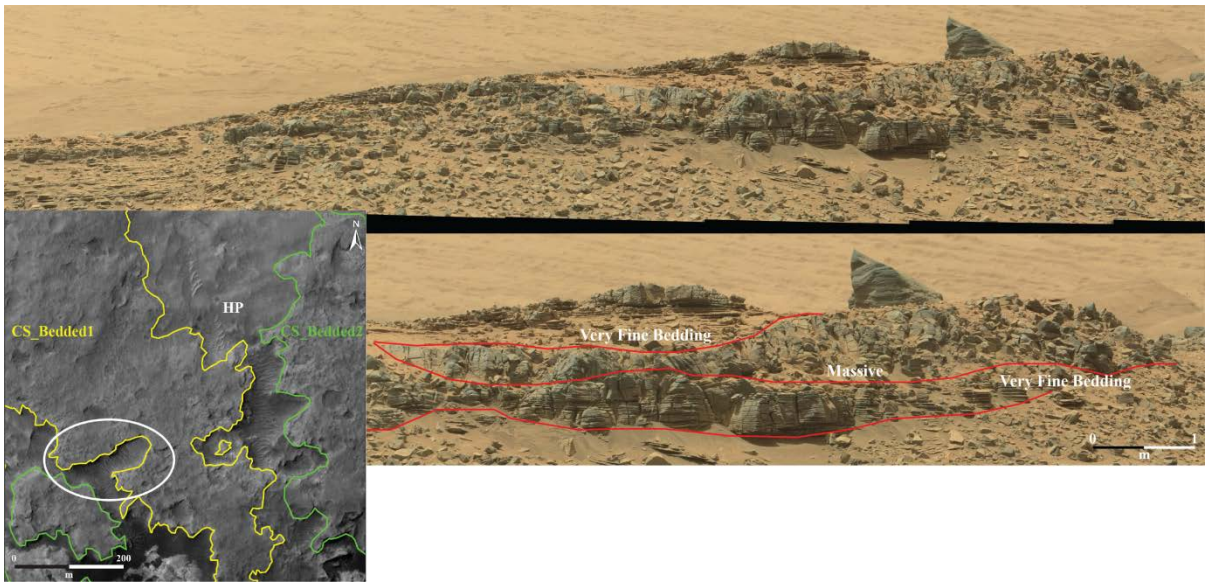

Figure 3.1: The SE wall of Hidden Valley. Bottom image, which is a subset of the top image, shows the stratigraphically distinct bedding variations. The inset on the left is the HiRISE image showing the Hidden Valley location (white oval) from orbit. CS_Bedded sub-units are outlined.

3.2.2 Hummocky Plains Unit

For much of the ~9 km traverse from Yellowknife Bay to the base of Mount Sharp, the Curiosity rover travelled across the HP unit. In Mastcam images (Fig. 3.2), the HP unit is characterized mainly by a pavement of loose clasts that range in size from pebbles to boulders. The HP unit also includes several exposures of in situ conglomerate and sandstone outcrops that were analyzed by the Curiosity rover. These exposures are small, and are indistinguishable at the orbital scale in figure 1.7 (Williams et al., 2013; Vasavada et al., 2014). The conglomerate outcrops consist of rounded grains that range in size from very coarse sand to pebbles. The sandstone outcrops, seen prominently at the Shaler outcrop, are characterized by pebble sized grains in a sandstone matrix and decimeter-scale trough cross-stratification (Anderson et al., 2014; Vasavada et al., 2014).

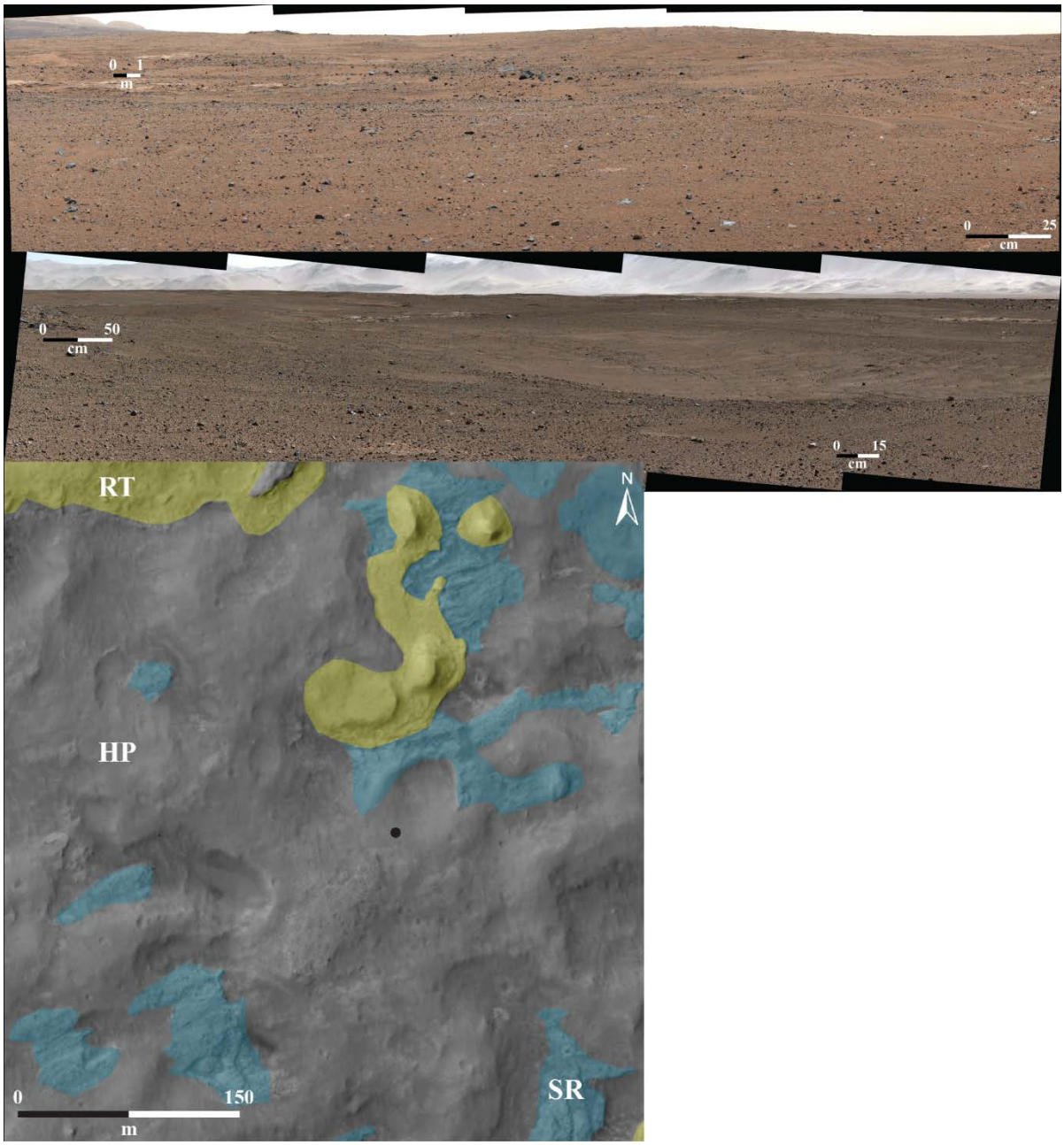

Figure 3.2: Mastcam images showing the physical characteristics of the HP unit. Orbital inset shows the physical differences between the HP, RT, and SR units. Black dot indicates the rover's position on sol 634 when the bottom Mastcam mosaic was taken. The rover's position on sol 338 when the top Mastcam image was taken can be seen in figure 3.3.

3.2.3 Bedded Fractured Unit

The BF unit was studied in great detail during the first year of the Curiosity mission at Yellowknife Bay, an area that was picked for the rover's first major stop because of its

proximity to the intersection point between the CS, BF, and HP units, the area's high thermal inertia, and the fractured stratified deposits that could be traced in HiRISE images (Grotzinger et al., 2014). The BF unit was observed in situ at exposures of the Gillespie Lake and Sheepbed members of the Yellowknife Bay formation (Fig. 3.3). The Sheepbed member is a very fine-grained sedimentary rock of bulk basaltic composition and has been eroded back to form a topographic scarp at the contact with the Gillespie Lake member. The uniform fine grain size of the Sheepbed member and the lateral continuity of the Sheepbed-Gillespie Lake boundary support a distal alluvial or lacustrine depositional interpretation for the Sheepbed member (Grotzinger et al., 2014). The presence of abundant diagenetic features such as nodules, hollow nodules, and raised ridges (nonpolygonal, parallel-sided fractures) suggests that the sediments of the Sheepbed member experienced post-depositional aqueous alteration (Grotzinger et al., 2014; Siebach et al., 2014; Stack et al., 2014).

The Gillespie Lake member of Yellowknife Bay is stratigraphically lower than the Sheepbed member. The Gillespie Lake strata consist of poorly sorted, massive sandstone (Grotzinger et al., 2014). The grains are angular to well-rounded and range in size from medium to very coarse sand of bulk basaltic composition. The Gillespie Lake sandstones have very low porosity suggesting a high degree of cementation. The presence of raised ridges, similar to those seen in the Sheepbed member, support the idea of early cementation of the Gillespie Lake member (Grotzinger et al., 2014; Siebach et al., 2014). The fine-grained mudstones of the Sheepbed member plus the coarser grained sandstones of the Gillespie Lake member make the Yellowknife Bay formation a very texturally heterogeneous location.

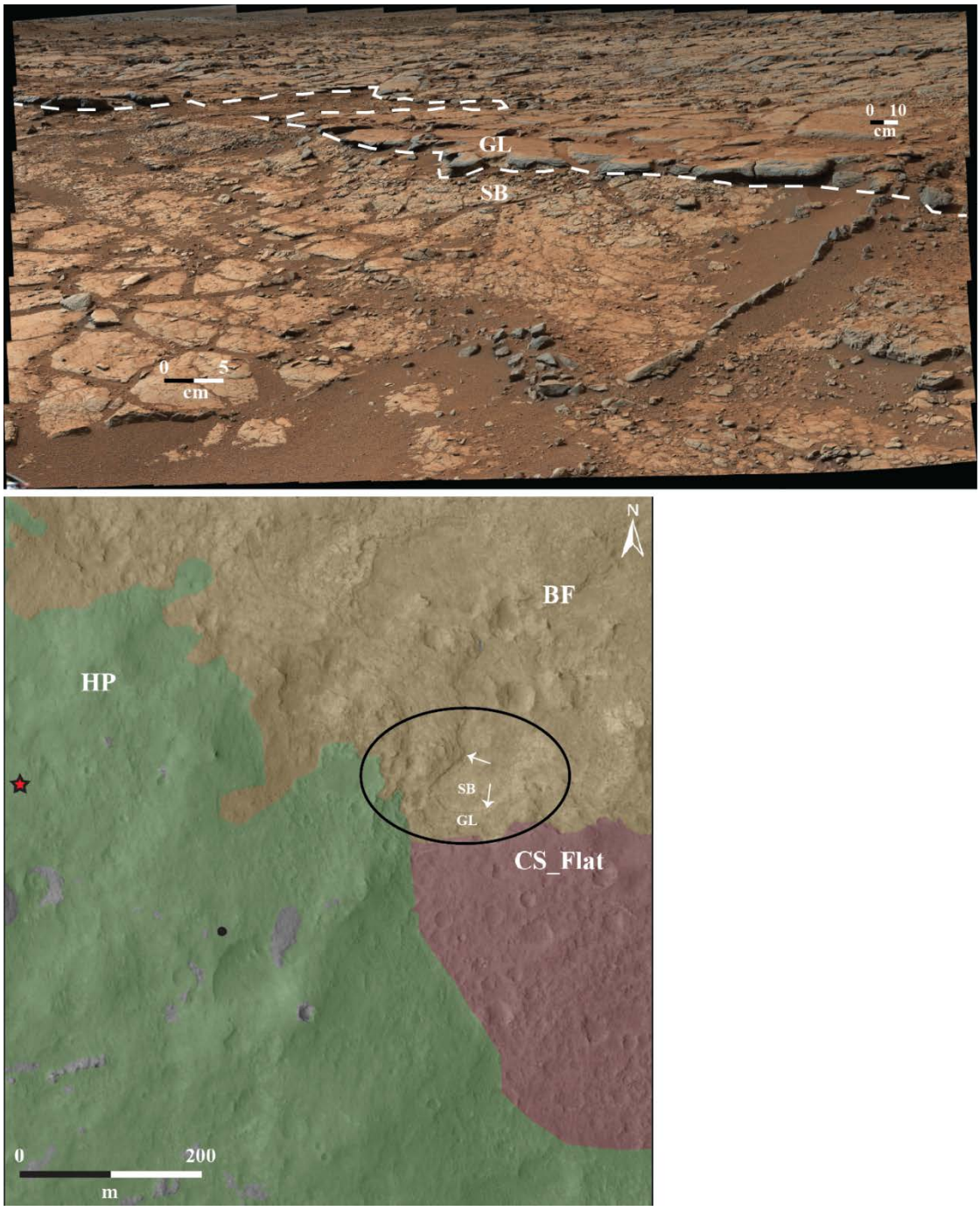

Figure 3.3: Mastcam image shows the in situ physical characteristics of the BF unit as seen in the Sheepbed and Gillespie Lake members of the Yellowknife Bay formation. Orbital inset shows the physical differences between the CS, HP, and BF units. The red outlined star is the Curiosity landing site, and the black dot is the location of the top HP unit Mastcam image in figure 3.2.

3.3 Methods

The craters in the Curiosity landing ellipse were originally mapped by Mackenzie Day at a 1:1000 scale in four HiRISE images that covered the majority of the landing ellipse (PSP_009716_1755, PSP_003453_1750, PSP_009571_1755, and ESP_011417_1755). This scale was chosen as an appropriate scale to map the smallest crater, but was small enough as to not pixelate the HiRISE images. The 0.25 cm/pixel spatial resolution of the HiRISE images enabled craters as small as 1 m across to be included in the dataset, totaling ~75,700 craters. In this study, additional HiRISE coverage was used to supplement the original database.

The geologic unit shapefiles from Grotzinger et al. (2014) were modified to define the boundaries of the CS, HP, and BF units used in this study. Not only was the CS divided into the five new sub-units, the contacts of the geologic units were altered based on my preferences. This resulted in subtle differences in the surface area of the geologic units in figure 1.7 from the original geologic units published in (Grotzinger et al., 2014). Craters specifically associated with the CS, HP, and BF units were identified using the modified geologic unit shapefiles and the intersect tool in the Analysis Tools section of the ArcToolbox in ArcGIS 10.0. Crater statistics such as total number of craters per unit (N) and diameter (D) were compiled and measured in ArcGIS.

Interpreted ages for each unit were derived from the cumulative frequency plots produced by the Craterstats2 software (Michael and Neukum, 2010). Absolute ages were calculated from the production function of Hartmann (2005) and the chronology function of Michael (2013). Craters < 31 m in diameter were not used for the age interpretations. However, these craters (D = 1 – 31 m) were useful in deciphering the relative erosional history of the various units.

3.4 Results

3.4.1 Crater Counts of the CS Sub-Units

It was noted from inspection of HiRISE images that the five CS sub-units have differences in both their geomorphic characteristics and their crater densities. The cumulative crater frequency plot (Fig. 3.4) shows that for craters 1 – 20 m in diameter, the five CS sub-units can be divided into roughly three groups based on the crater density the sub-unit retains. For craters < 8 m in diameter, CS_Infill1 and CS_Bedded2 have the lowest crater density (~200 craters/km^2), and CS_Infill2 and CS_Flat have a slightly higher crater density (~400 craters/km^2). For craters > 8 m in diameter, CS_Infill1, CS_Infill2, and CS_Bedded2 all have similar crater densities. CS_Flat has a higher crater density for craters 8-20 m in diameter and then has a similar crater density as the other three sub-units for the larger craters. CS_Bedded1 has the highest crater density for all craters 1 – 63 m in diameter. However, CS_Infill2 has the highest crater density of craters > 63 m in diameter, as CS_Bedded1 does not have any identified craters > 63 m in diameter.

For craters > 31 m in diameter, the five sub-units can be divided into two categories to predict the crater retention ages. Cumulative statistics for CS_Flat, CS_Infill1, CS_Infill2, and CS_Bedded2 approach the 250 Ma isochron. The cumulative statistics for CS_Bedded1 approach the 1.1 Ga isochron. These ages place all five CS sub-units in the early to mid-Amazonian. It should be noted that while the areas used in this study are small, the statistical error, based on the number of craters per size bin, supports the results of this project.

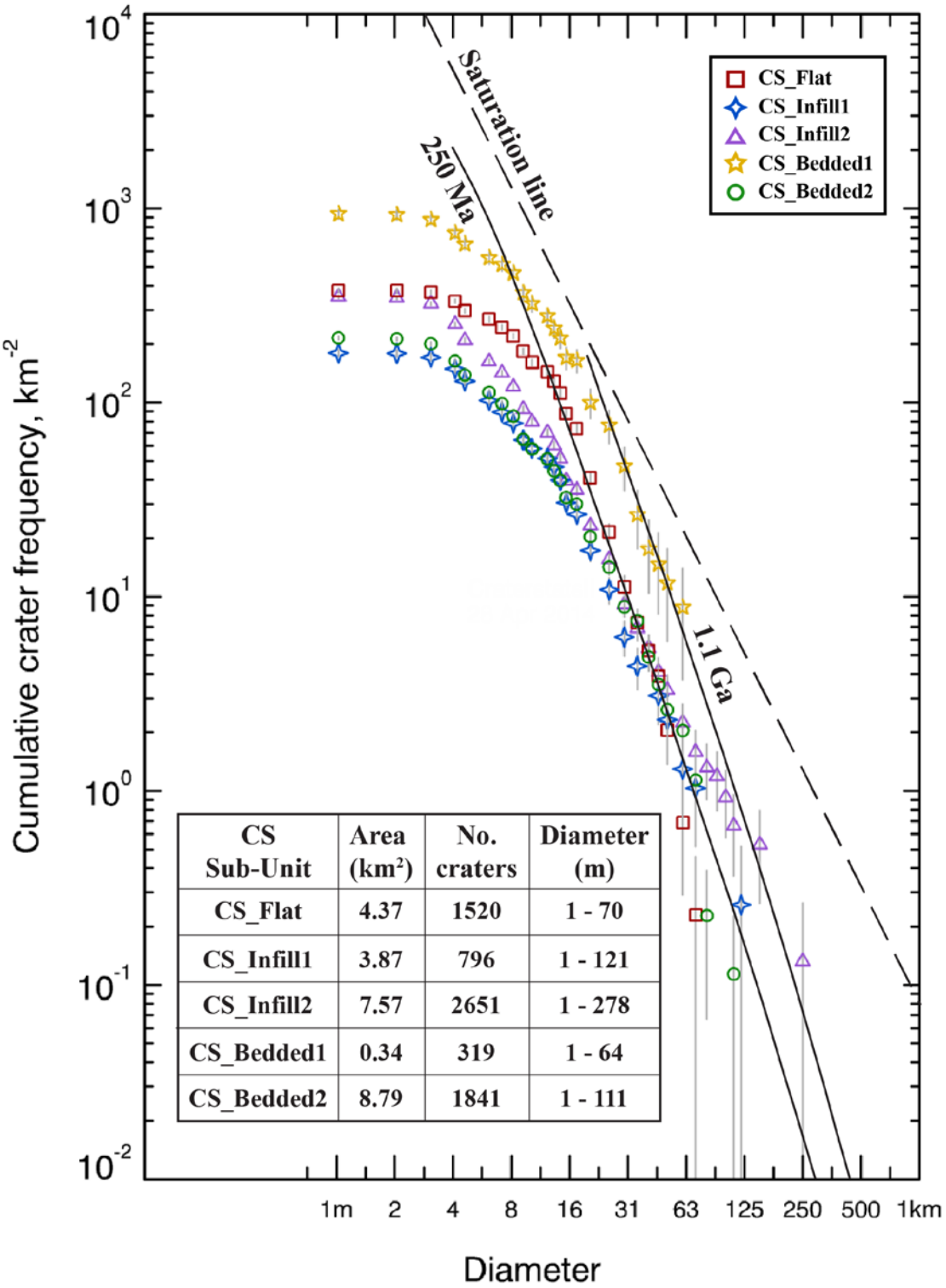

CS Sub-Unit	Area (km^2)	No. craters	Diameter (m)
CS_Flat	4.37	1520	1 - 70
CS_Infill1	3.87	796	1 - 121
CS_Infill2	7.57	2651	1 - 278
CS_Bedded1	0.34	319	1 - 64
CS_Bedded2	8.79	1841	1 - 111

Figure 3.4: The cumulative crater frequency plot comparing the crater densities and predicted ages for the five CS sub-units.

3.4.2 Crater Counts of the CS, HP, and BF Landing Ellipse Units

The CS, HP, and BF units are the three major units in the Curiosity landing ellipse identified from orbital mapping (Fig. 1.7). A cumulative crater frequency plot (Fig. 3.5) shows that for craters 1 – 20 m in diameter, the CS has the highest crater density whereas the BF unit has the lowest crater density; this matches the findings of Grant et al. (2014). For craters 20 – 63 m in diameter, the three units have similar crater densities. Lastly, the CS has a lower crater density for craters > 63 m in diameter, whereas the HP and BF units have a similar density for craters in this size range. For age-dating it is useful to plot the units separately (Fig. 3.6).

Cumulative statistics for the CS approach the 250 Ma isochron for craters > 16 m in diameter. Data the HP and BF units fall on two isochrons (Fig. 3.6). Specifically, for craters 31 - 50 m in diameter, cumulative statistics for the HP and BF units also indicate an age of 250 Ma. However, the craters > 125 m in diameter indicate an age of 600 Ma. The craters 50 - 125 m in diameter produce a bend in the data and these craters do not fall on any expected isochron. The predicted ages for the CS, HP, and BF units would date these surfaces as early to mid-Amazonian.

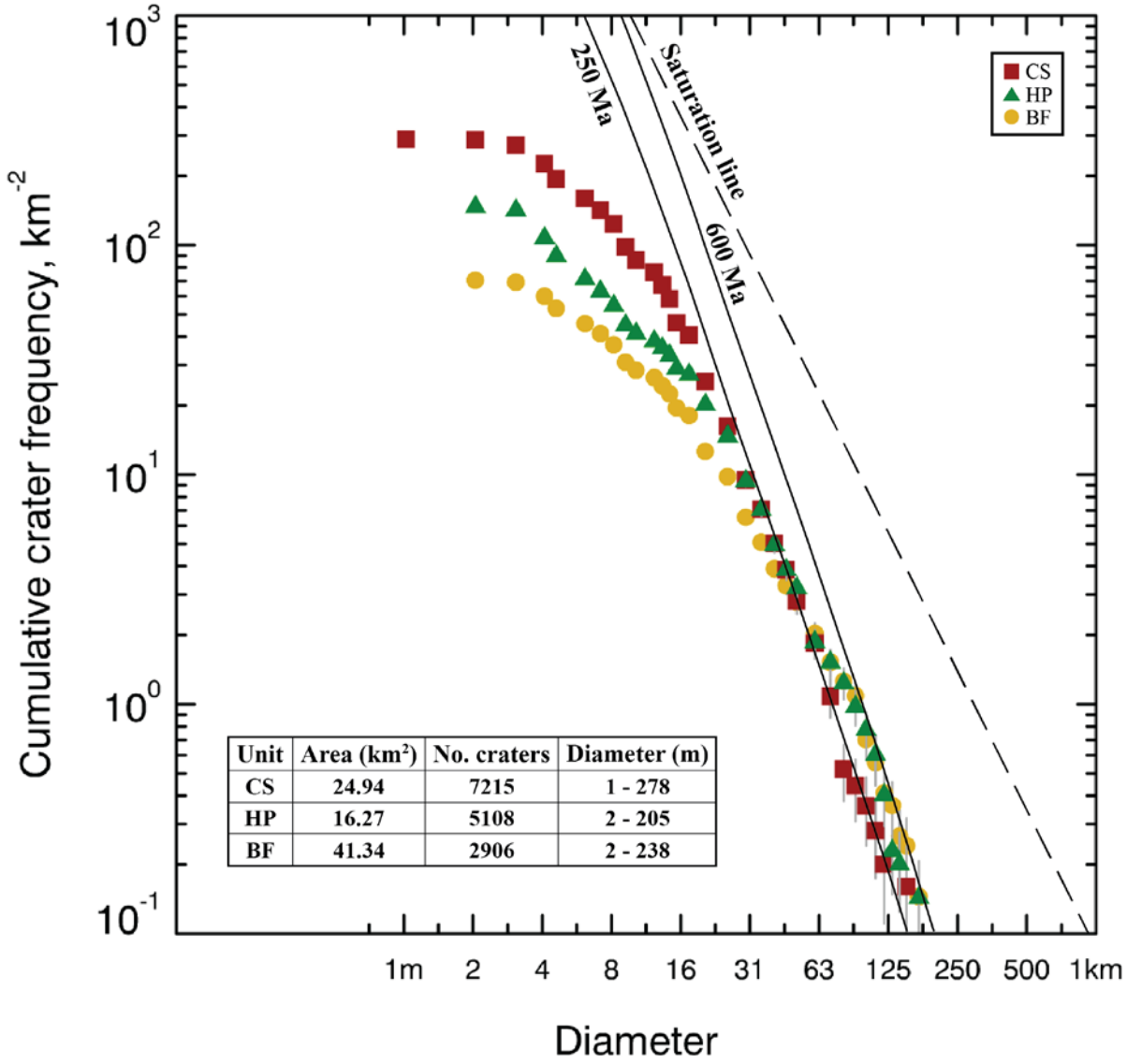

Figure 3.5: Cumulative crater frequency plot comparing the crater densities of the CS, HP, and BF units. The differences in crater densities for craters 1-31 m in diameter help determine the relative erosional resistance of the three units.

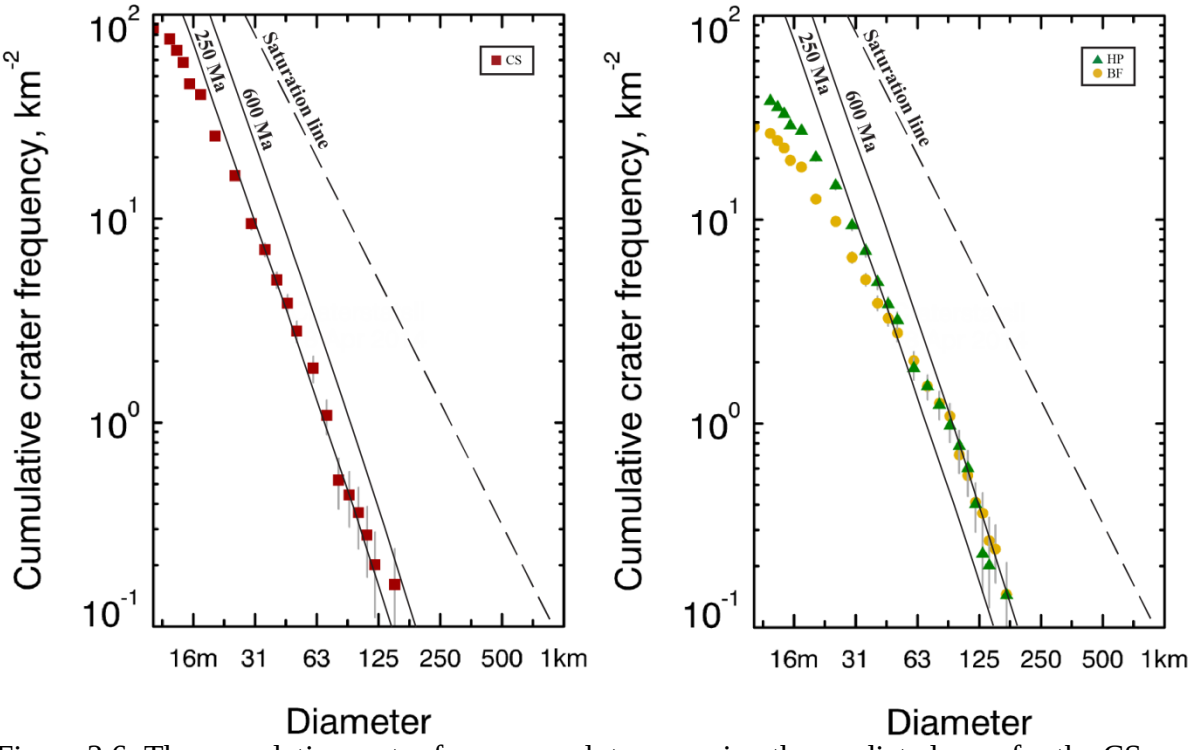

Figure 3.6: The cumulative crater frequency plot comparing the predicted ages for the CS, HP, and BF units. The crater densities for the CS predict one age for the entire unit. However, there is a bend in the crater densities for both the HP and BF units, indicating two possible ages.

3.5 Discussion

3.5.1 Erosional Resistance

Whereas the small craters (D < 31 m) may not be helpful in determining the age of a surface, they are helpful in understanding the relative erosional resistance of the three landing ellipse units. The fact that the CS has the highest density of these small craters indicates that the CS is either the most erosionally resistant unit compared to the HP and BF units (and likely for all the units in the landing ellipse) or is the oldest unit in the landing ellipse. However, there is both visual evidence, weathering patterns of the three units as seen in HiRISE and Mastcam images, and quantitative evidence, predicted relative ages from this study, that indicate the CS is the youngest unit in the Curiosity landing ellipse. The in situ outcrops of the CS, as seen in Hidden Valley, form meter scale erosional scarps that cap mesas and valley walls. The talus slopes and fields of angular float rocks surrounding the CS

outcrops indicate the CS material is well indurated. This is contrary to the weathering pattern of the HP unit, which rarely forms scarps and is not observed to cap mesa or valley walls. This weathering pattern is indicative of a poorly indurated unit. The weathering pattern of the CS and HP unit suggest that induration plays a key role in how well a unit retains impact craters. The weathering patterns seen in Mastcam images confirm that the CS is more erosionally resistant than the HP unit. Therefore, the high crater density of the CS, compared to the HP and BF units, indicates that the CS is the most erosionally resistant unit in the landing ellipse.

Whereas the BF unit is also expressed by in situ outcrops in the Mastcam images, there are several physical characteristics that cause it to be the least erosionally resistant unit compared to the CS and HP unit. The combination of fine-grained mudstones and coarser grained sandstones, as seen in the Sheepbed and Gillespie Lake members, creates a heterogeneous target material that ultimately hinders the BF unit's crater retention ability. Whereas there are erosionally resistant portions of the BF unit, i.e. the raised ridges in the Sheepbed and Gillespie Lake members, the majority of the Yellowknife Bay area imaged by Curiosity appears to be highly susceptible to erosion and alteration. Additionally, the original porosity of the Yellowknife Bay material, although reduced by the post-depositional diagenetic processes, likely enhanced the erosional susceptibility of the BF unit.

3.5.2 Stratigraphy of the CS, HP, and BF Units

The crater densities and predicted ages presented in this study confirm that the CS is the youngest unit mapped in the Curiosity landing ellipse. The fact that the CS has retained more small craters ($D < 31$ m) suggests that the CS has also retained more of the larger craters ($D > 31$ m) that were used to predict the ages of the units in this study. Therefore, since the density of larger craters has been the least affected by erosion, this confirms that the CS is the youngest unit of the three units compared in this study. This matches the visual stratigraphy, as observed in the Mastcam images at Yellowknife Bay. The stratigraphic order of the three units observed in this study, from oldest to youngest is BF, HP, and CS. The erosional scarp that forms at the contact between the CS and BF unit, and the BF and HP units provide visual verification that the BF unit is the oldest stratigraphic unit (Fig. 2.5).

The erosional scarps that form at the contact of the CS and HP unit elsewhere throughout the landing ellipse indicate that the CS is stratigraphically younger than the HP unit.

Because of the statistical uncertainty in the cumulative crater frequency plots, the predicted ages for the HP and BF units are the same. There are two scenarios to explain this similarity: (1) the true age of these two units are so close that their respective crater densities were never different enough to predict different ages, or (2) the erosional resistance of the two units has affected the density of the larger craters used to predict the ages. Because the BF unit is the least erosionally resistant unit of the three units compared in this study, the larger craters that would have been used to calculate ages would have been most affected by erosion. Therefore, any larger craters that were potentially part of the original BF unit crater density have likely eroded away and the predicted age from this study is younger than the true age of the BF unit.

Even within the statistical uncertainty of the crater frequency plots for the HP and BF units there is a noticeable bend in the data. This bend supports the possibility of a resurfacing event in the history of these two units. The smaller craters ($31 < D < 50$) of the HP and BF units predict a resurfacing event with an age of 250 Ma. This resurfacing event corresponds with the crater retention age of the CS. This is proof that even though the absolute ages of the three units in this study may not be statistically different, the relative age difference between the HP (and BF) unit and the CS is accurate.

3.5.3 Relative Timing of the CS Deposition

As mentioned above, the ages predicted from the Hartmann (2005) production function are crater retention ages. Accordingly, we explore two possibilities: (1) the ages presented in this study for the CS represent the absolute deposition age (Fig. 3.7), or (2) the ages presented here date the timing of the last resurfacing or exhumation event (Fig. 3.8). If the predicted age represents the true deposition age of the CS, there are two possible scenarios under which the CS could have been deposited, either scenario would suggest that the deposition of the CS is a very recent event in the history of Gale Crater. The first scenario (Fig. 3.7a) assumes that the impact that formed Gale Crater occurred near the

Noachian/Hesperian boundary , and the crater-filling strata of lower Mount Sharp formed shortly after the impact (Malin and Edgett, 2000; Irwin et al., 2005; Thomson et al., 2011; Grant et al., 2014). Being that the predicted ages for the CS are far younger than the Noachian, the CS would have had to be deposited after the deposition and erosion of the older Noachian/Hesperian-aged layered sediments. The processes responsible for the erosion of the older strata and the duration and extent of this erosion are unknown.

The second scenario (Fig. 3.7b) assumes the depositional model put forth by Kite et al. (2013), which does not require all of Gale Crater to be filled with sediments, rather Kite et al. (2013) conclude that Mt. Sharp is a depositional feature formed in a shape close to its current morphology mostly from aeolian deposition. The paper places no constraints on the timing of deposition of the crater floor units. Therefore, it is possible that the crater floor units (at least the youngest CS unit) could have been deposited much later after the formation of Gale Crater and Mt. Sharp, with an unknown amount of time and erosion between the two depositional events. Under these two scenarios, it is possible that the 250 Ma age of the CS is the true deposition age.

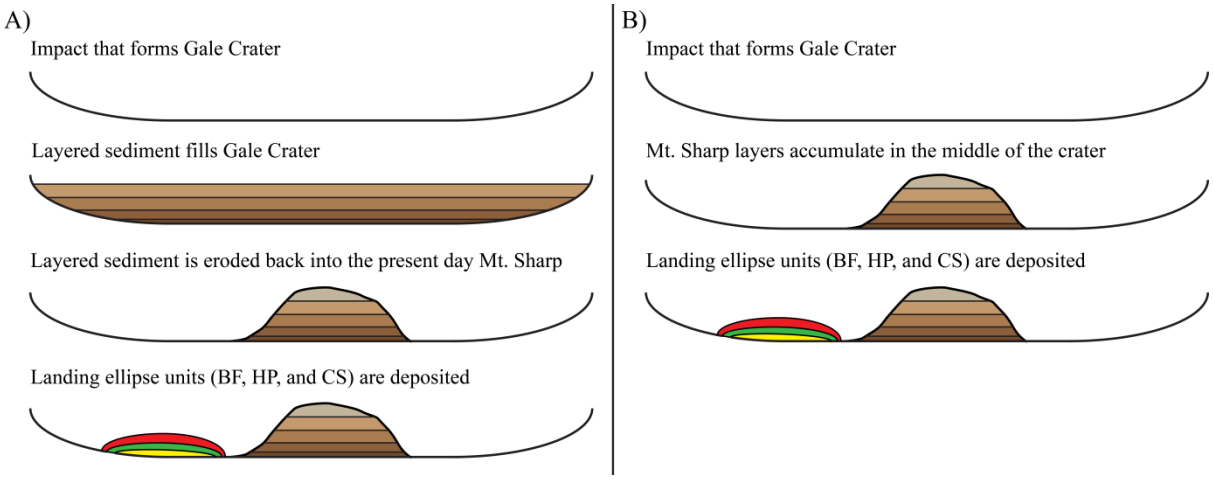

Figure 3.7: A cartoon showing the two scenarios under which the predicted age of the CS would represent the true deposition age. Scenario 1 (A) illustrates the Malin theory and has the deposition of the landing ellipse units being after the erosion that formed Mt. Sharp. Scenario 2 (B) illustrates the Kite theory and has the deposition of the landing ellipse units being after the aeolian deposition that formed Mt. Sharp.

Alternatively, the predicted ages could represent the age of the last resurfacing or exhumation event (possibility 2). Because the CS is interpreted to be the youngest stratigraphic unit in the landing ellipse, the last "resurfacing" event would have been the erosional exhumation of the CS. This suggests that the CS was at one time completely buried (Fig. 3.8), and has only been exposed for the last 250 Ma of Martian history. This would also suggest that erosional processes were actively eroding Mt. Sharp into its present state very recently in Martian history.

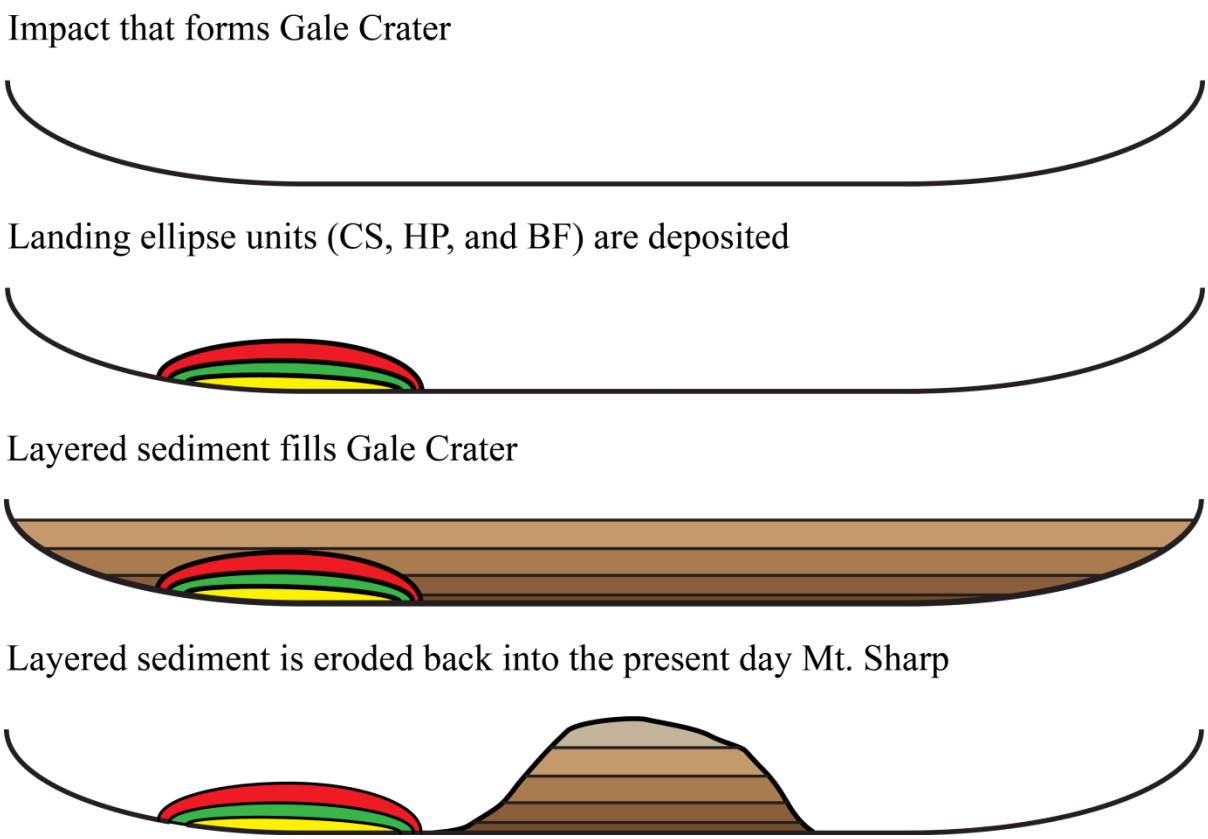

Figure 3.8: A cartoon illustrating the sequence of events under which the predicted age of the CS would represent the age of the last "resurfacing" event, the exhumation of the CS. This cartoon assumes that Gale Crater was once filled to some extent with the layered sediments that formed Mt. Sharp. These layered sediments would have completely buried the landing ellipse units (CS, HP, and BF).

3.6 Conclusion

In August 2012, the Curiosity rover safely landed in Gale Crater. Prior to landing, the landing ellipse for the Curiosity rover was mapped into six geomorphic units including the AF, BF, CS, HP, RT, and SR units. All of the heavily cratered exposures were mapped as one geomorphic unit (the CS). The CS exposures share three distinguishing geomorphic characteristics including a high crater density, mesa-forming erosional scarps, and a nearly horizontal surface. However, differences in the physical characteristics of the CS exposures, such as albedo and crater density suggest that the CS was not one laterally extensive geomorphic unit, but could instead be divided into multiple sub-units. In Mastcam images, the CS sub-units appear to be made of similar material that is characterized by fine grained, resistant outcrops that always cap mesas and valley walls.

The majority of the CS sub-units, four out of five, were imaged by Curiosity. The physical characteristics of the various sub-units, as seen in HiRISE and Mastcam images, were compared to the physical characteristics of the deposits of various terrestrial geologic processes, in an attempt to understand the geologic origin of each CS sub-unit. Although none of the characteristics of the CS sub-units are exclusive to one depositional environment, some constraints can be placed on the types of environments that the CS sub-units could have formed under.

For instance, the planar surface and ponding against the topographically higher slopes of Bradbury Rise that is characteristic of CS_Flat could represent either an inflated pāhoehoe lava flow or low-energy fluvial environment. Similarly, the planar surface and topographic relationships of CS_Infill1 and CS_Infill2 with the topographically higher impact crater rims, suggest these two CS sub-units also formed under a low-energy lateral depositional environment. This low-energy environment could again be either an inflated pāhoehoe lava flow or low-energy fluvial environment. The horizontal bedding of the CS_Bedded1 deposit suggests that this sub-unit either formed in a lacustrine or deltaic environment. Lastly, the inclined bedding of the CS_Bedded2 deposit suggests that this sub-unit represents either the foresets of a delta front, or aeolian dunes. The data does not allow for a single origin to be conclusively stated as the geologic origin for any of the CS sub-units.

Another goal of this study was to use HiRISE and Mastcam images to determine what physical characteristics of a geologic unit could help or hinder the retention of impact craters. The crater densities of the five CS sub-units were compared to determine that there are at least two ages represented in the CS exposures. The crater densities of the CS, HP, and BF units were compared to determine that the CS is the most erosionally resistant unit of the three units (and possibly in the entire Curiosity landing ellipse) and that the BF unit is the least erosionally resistant unit of the three units compared in this study. The BF unit was characterized mainly by the features seen in the Mastcam images of the Sheepbed and Gillespie Lake members of the Yellowknife Bay formation. The very fine to coarse-grained sedimentary rocks of the Sheepbed and Gillespie Lake members are among the least erosionally resistant rocks observed by the Curiosity rover, and fail to retain craters. Both visual inspection of HiRISE and Mastcam images, and the predicted ages of the crater densities confirm that the CS sub-units represent the youngest stratigraphic unit in the Curiosity landing ellipse.

Bibliography

Anderson, R.B., Bell, J.F., 2010. Geologic mapping and characterization of Gale Crater and implications for its potential as a Mars Science Laboratory landing site. Mars 5, 76–128. doi:10.1555/mars.2010.0004

Anderson, R., Bridges, J.C., Williams, A., Edgar, L., Ollila, A., Williams, J., Nachon, M., Mangold, N., Fisk, M., Schieber, J., Gupta, S., Dromart, G., Wiens, R., Le Mouelic, S., Forni, O., Lanza, N., Mezzacappa, A., Sautter, V., Blaney, B., Clark, B., Clegg, S., Gasnault, O., Lasue, J., Leveille, R., Lewin, E., Lewis, K.W., Maurice, S., Newsom, H., Schwenzer, S.P., Vaniman, D., 2014. ChemCam results from the Shaler outcrop in Gale Crater, Mars. Icarus 249, 2–21.

Beyer, R.A., Stack, K.M., Griffes, J.L., Milliken, R.E., Herkenhoff, K.E., Byrne, S., Holt, J.W., Grotzinger, J.P., 2012. An Atlas of Mars Sedimentary Rocks as seen by HiRISE, in: Grotzinger, J.P., Milliken, R.E. (Eds.), Sedimentary Geology of Mars, SEPM Special Publication. SEPM (Society for Sedimentary Geology), pp. 49–95.

Bhattacharya, J.P., 2006. Deltas, in: Posamentier, H.W., Walker, R.G. (Eds.), Facies Models Revisited. Society for Sedimentary Geology.

Blasius, K.R., Cutts, J.A., 1977. Geology of the Valles Marineris: First Analysis of Imaging From the Viking 1 Orbiter Primary Mission. Journal of Geophysical Research 82, 4067–4091.

Bridges, N.T., Calef, F.J., Hallet, B., Herkenhoff, K.E., Lanza, N.L., Le Mouélic, S., Newman, C.E., Blaney, D.L., de Pablo, M.A., Kocurek, G.A., Langevin, Y., Lewis, K.W., Mangold, N., Maurice, S., Meslin, P.-Y., Pinet, P., Renno, N.O., Rice, M.S., Richardson, M.E., Sautter, V., Sletten, R.S., Wiens, R.C., Yingst, R.A., 2014. The rock abrasion record at Gale Crater: Mars Science Laboratory results from Bradbury Landing to Rocknest: ABRASION AT GALE CRATER. Journal of Geophysical Research: Planets 119, 1374–1389. doi:10.1002/2013JE004579

Brookfield, M.E., 1977. The origin of bounding surfaces in ancient aeolian sandstones. Sedimentology 24, 303–332.

Cabrol, N.A., Grin, E.A., Newsom, H.E., Landheim, R., McKay, C.P., 1999. Hydrogeologic Evolution of Gale crater and Its Relevance to the Exobiological Exploration of Mars. Icarus 139, 235–245.

Calef, F.J., Dietrich, W.E., Edgar, L., Farmer, J., Fraeman, A., Grotzinger, J., Palucis, M.C., Parker, T., Rice, M., Rowland, S., Stack, K.M., Sumner, D., Williams, J., MSL Science Team, 2013. Geologic Mappig of the Mars Science Laboratory Landing Ellipse. Presented at the Lunar and Planetary Science Conference.

Carpenter, A.H., 1948. Principles of Historical Geology Applied to Neighboring Planets and Life on Mars. Popular Astronomy 56, 233–246.

Carr, M.H., Head, J.W., 2010. Geologic history of Mars. Earth and Planetary Science Letters 294, 185–203. doi:10.1016/j.epsl.2009.06.042

Christensen, P.R., Jakosky, B.M., Kieffer, H.H., Malin, M.C., McSween Jr, H.Y., Nealson, K., Mehall, G.L., Silverman, S.H., Ferry, S., Caplinger, M., Ravine, M., 2004. The thermal emission imaging system (THEMIS) for the Mars 2001 Odyssey Mission. Space Science Reviews 110, 85–130.

Daubar, I.J., McEwen, A.S., Byrne, S., Kennedy, M.R., Ivanov, B., 2013. The current martian cratering rate. Icarus 225, 506–516. doi:10.1016/j.icarus.2013.04.009

Edgett, K.S., Yingst, R.A., Ravine, M.A., Caplinger, M.A., Maki, J.N., Ghaemi, F.T., Schaffner, J.A., Bell, J.F., Edwards, L.J., Herkenhoff, K.E., Heydari, E., Kah, L.C., Lemmon, M.T., Minitti, M.E., Olson, T.S., Parker, T.J., Rowland, S.K., Schieber, J., Sullivan, R.J., Sumner, D.Y., Thomas, P.C., Jensen, E.H., Simmonds, J.J., Sengstacken, A.J., Willson, R.G., Goetz, W., 2012. Curiosity's Mars Hand Lens Imager (MAHLI) Investigation. Space Science Reviews 170, 259–317. doi:10.1007/s11214-012-9910-4

Falk, P.D., Dorsey, R.J., 1998. Rapid development of gravelly high-density turbidity currents in marine Gilbert-type fan deltas, Loreto Basin, Baja California Sur, Mexico. Sedimentology 45, 331–349.

Gani, M.R., 2004. From Turbid to Lucid: A Straightforward Approach to Sediment Gravity Flows and Their Deposits. The Sedimentary Record 2, 4–8.

Garry, W.B., Robinson, M.S., Zimbelman, J.R., Bleacher, J.E., Hawke, B.R., Crumpler, L.S., Braden, S.E., Sato, H., 2012. The origin of Ina: Evidence for inflated lava flows on the Moon: INFLATED LAVA FLOWS ON THE MOON. Journal of Geophysical Research: Planets 117, n/a–n/a. doi:10.1029/2011JE003981

Gee, M.J.R., Masson, D.G., Watts, A.B., Mitchell, N.C., 2001. Passage of debris flows and turbidity currents through a topographic constriction: seafloor erosion and deflection of flow pathways. Sedimentology 48, 1389–1409.

Ghaemi, F.T., 2009. Design and fabrication of lenses for the color science cameras aboard the Mars Science Laboratory rover. Optical Engineering 48, 103002. doi:10.1117/1.3251343

Gilbert, G.K., 1890. Lake Bonneville. US Government Printing Office.

Golombek, M., Grant, J., Kipp, D., Vasavada, A., Kirk, R., Fergason, R., Bellutta, P., Calef, F., Larsen, K., Katayama, Y., Huertas, A., Beyer, R., Chen, A., Parker, T., Pollard, B., Lee, S., Sun, Y., Hoover, R., Sladek, H., Grotzinger, J., Welch, R., Noe Dobrea, E., Michalski, J., Watkins, M., 2012. Selection of the Mars Science Laboratory Landing Site. Space Science Reviews 170, 641–737. doi:10.1007/s11214-012-9916-y

Grant, J.A., Wilson, S.A., Mangold, N., Calef, F., Grotzinger, J.P., 2014. The timing of alluvial activity in Gale crater, Mars. Geophysical Research Letters 41, 1142–1149. doi:10.1002/2013GL058909

Greeley, R., Guest, J.E., 1987. Geologic map of the eastern equatorial region of Mars. United States Geological Survey Miscellaneous Investigations Series.

Grotzinger, J.P., Crisp, J., Vasavada, A.R., Anderson, R.C., Baker, C.J., Barry, R., Blake, D.F., Conrad, P., Edgett, K.S., Ferdowski, B., Gellert, R., Gilbert, J.B., Golombek, M., Gómez-Elvira, J., Hassler, D.M., Jandura, L., Litvak, M., Mahaffy, P., Maki, J., Meyer, M., Malin, M.C., Mitrofanov, I., Simmonds, J.J., Vaniman, D., Welch, R.V., Wiens, R.C., 2012. Mars Science Laboratory Mission and Science Investigation. Space Science Reviews 170, 5–56. doi:10.1007/s11214-012-9892-2

Grotzinger, J.P., Milliken, R.E., 2012. The Sedimentary Rock Record of Mars: Distribution, Origins, and Global Stratigraphy, in: Grotzinger, J.P., Milliken, R.E. (Eds.), Sedimentary Geology of Mars, SEPM Special Publication. SEPM (Society for Sedimentary Geology), pp. 1–48.

Grotzinger, J.P., Sumner, D.Y., Kah, L.C., Stack, K., Gupta, S., Edgar, L., Rubin, D., Lewis, K., Schieber, J., Mangold, N., Milliken, R., Conrad, P.G., DesMarais, D., Farmer, J.,

Siebach, K., Calef, F., Hurowitz, J., McLennan, S.M., Ming, D., Vaniman, D., Crisp, J., Vasavada, A., Edgett, K.S., Malin, M., Blake, D., Gellert, R., Mahaffy, P., Wiens, R.C., Maurice, S., Grant, J.A., Wilson, S., Anderson, R.C., Beegle, L., Arvidson, R., Hallet, B., Sletten, R.S., Rice, M., Bell, J., Griffes, J., Ehlmann, B., Anderson, R.B., Bristow, T.F., Dietrich, W.E., Dromart, G., Eigenbrode, J., Fraeman, A., Hardgrove, C., Herkenhoff, K., Jandura, L., Kocurek, G., Lee, S., Leshin, L.A., Leveille, R., Limonadi, D., Maki, J., McCloskey, S., Meyer, M., Minitti, M., Newsom, H., Oehler, D., Okon, A., Palucis, M., Parker, T., Rowland, S., Schmidt, M., Squyres, S., Steele, A., Stolper, E., Summons, R., Treiman, A., Williams, R., Yingst, A., Team, M.S., Kemppinen, O., Bridges, N., Johnson, J.R., Cremers, D., Godber, A., Wadhwa, M., Wellington, D., McEwan, I., Newman, C., Richardson, M., Charpentier, A., Peret, L., King, P., Blank, J., Weigle, G., Li, S., Robertson, K., Sun, V., Baker, M., Edwards, C., Farley, K., Miller, H., Newcombe, M., Pilorget, C., Brunet, C., Hipkin, V., Leveille, R., Marchand, G., Sanchez, P.S., Favot, L., Cody, G., Fluckiger, L., Lees, D., Nefian, A., Martin, M., Gailhanou, M., Westall, F., Israel, G., Agard, C., Baroukh, J., Donny, C., Gaboriaud, A., Guillemot, P., Lafaille, V., Lorigny, E., Paillet, A., Perez, R., Saccoccio, M., Yana, C., Armiens-Aparicio, C., Rodriguez, J.C., Blazquez, I.C., Gomez, F.G., Gomez-Elvira, J., Hettrich, S., Malvitte, A.L., Jimenez, M.M., Martinez-Frias, J., Martin-Soler, J., Martin-Torres, F.J., Jurado, A.M., Mora-Sotomayor, L., Caro, G.M., Lopez, S.N., Peinado-Gonzalez, V., Pla-Garcia, J., Manfredi, J.A.R., Romeral-Planello, J.J., Fuentes, S.A.S., Martinez, E.S., Redondo, J.T., Urqui-O'Callaghan, R., Mier, M.-P.Z., Chipera, S., Lacour, J.-L., Mauchien, P., Sirven, J.-B., Manning, H., Fairen, A., Hayes, A., Joseph, J., Sullivan, R., Thomas, P., Dupont, A., Lundberg, A., Melikechi, N., Mezzacappa, A., DeMarines, J., Grinspoon, D., Reitz, G., Prats, B., Atlaskin, E., Genzer, M., Harri, A.-M., Haukka, H., Kahanpaa, H., Kauhanen, J., Paton, M., Polkko, J., Schmidt, W., Siili, T., Fabre, C., Wray, J., Wilhelm, M.B., Poitrasson, F., Patel, K., Gorevan, S., Indyk, S., Paulsen, G., Bish, D., Gondet, B., Langevin, Y., Geffroy, C., Baratoux, D., Berger, G., Cros, A., d' Uston, C., Forni, O., Gasnault, O., Lasue, J., Lee, Q.-M., Meslin, P.-Y., Pallier, E., Parot, Y., Pinet, P., Schroder, S., Toplis, M., Lewin, E., Brunner, W., Heydari, E., Achilles, C., Sutter, B., Cabane, M., Coscia, D., Szopa, C., Robert, F., Sautter, V., Le Mouelic, S., Nachon, M., Buch, A., Stalport, F., Coll, P., Francois, P., Raulin, F., Teinturier, S., Cameron, J., Clegg, S., Cousin, A., DeLapp, D., Dingler, R., Jackson, R.S., Johnstone, S., Lanza, N., Little, C., Nelson, T., Williams, R.B., Jones, A., Kirkland, L., Baker, B., Cantor, B., Caplinger, M., Davis, S., Duston, B., Fay, D., Harker, D., Herrera, P., Jensen, E., Kennedy, M.R., Krezoski, G., Krysak, D., Lipkaman, L., McCartney, E., McNair, S., Nixon, B., Posiolova, L., Ravine, M., Salamon, A., Saper, L., Stoiber, K., Supulver, K., Van Beek, J., Van Beek, T., Zimdar, R., French, K.L., Iagnemma, K., Miller, K., Goesmann, F., Goetz, W., Hviid, S., Johnson, M., Lefavor, M., Lyness, E., Breves, E., Dyar, M.D., Fassett, C., Edwards, L., Haberle, R., Hoehler, T., Hollingsworth, J., Kahre, M., Keely, L., McKay, C., Bleacher, L., Brinckerhoff, W., Choi, D., Dworkin, J.P., Floyd, M., Freissinet, C., Garvin, J., Glavin, D., Harpold, D., Martin, D.K., McAdam, A., Pavlov, A., Raaen, E., Smith, M.D., Stern, J., Tan, F., Trainer, M., Posner, A., Voytek, M., Aubrey, A., Behar, A., Blaney, D., Brinza, D., Christensen, L., DeFlores, L., Feldman, J., Feldman, S., Flesch, G., Jun, I., Keymeulen, D., Mischna, M., Morookian, J.M., Pavri, B., Schoppers, M., Sengstacken, A., Simmonds, J.J., Spanovich, N., Juarez,

M. d. l. T., Webster, C.R., Yen, A., Archer, P.D., Cucinotta, F., Jones, J.H., Morris, R.V., Niles, P., Rampe, E., Nolan, T., Fisk, M., Radziemski, L., Barraclough, B., Bender, S., Berman, D., Dobrea, E.N., Tokar, R., Cleghorn, T., Huntress, W., Manhes, G., Hudgins, J., Olson, T., Stewart, N., Sarrazin, P., Vicenzi, E., Bullock, M., Ehresmann, B., Hamilton, V., Hassler, D., Peterson, J., Rafkin, S., Zeitlin, C., Fedosov, F., Golovin, D., Karpushkina, N., Kozyrev, A., Litvak, M., Malakhov, A., Mitrofanov, I., Mokrousov, M., Nikiforov, S., Prokhorov, V., Sanin, A., Tretyakov, V., Varenikov, A., Vostrukhin, A., Kuzmin, R., Clark, B., Wolff, M., Botta, O., Drake, D., Bean, K., Lemmon, M., Schwenzer, S.P., Lee, E.M., Sucharski, R., Hernandez, M.A. d. P., Avalos, J.J.B., Ramos, M., Kim, M.-H., Malespin, C., Plante, I., Muller, J.-P., Navarro-Gonzalez, R., Ewing, R., Boynton, W., Downs, R., Fitzgibbon, M., Harshman, K., Morrison, S., Kortmann, O., Williams, A., Lugmair, G., Wilson, M.A., Jakosky, B., Balic-Zunic, T., Frydenvang, J., Jensen, J.K., Kinch, K., Koefoed, A., Madsen, M.B., Stipp, S.L.S., Boyd, N., Campbell, J.L., Perrett, G., Pradler, I., VanBommel, S., Jacob, S., Owen, T., Savijarvi, H., Boehm, E., Bottcher, S., Burmeister, S., Guo, J., Kohler, J., Garcia, C.M., Mueller-Mellin, R., Wimmer-Schweingruber, R., Bridges, J.C., McConnochie, T., Benna, M., Franz, H., Bower, H., Brunner, A., Blau, H., Boucher, T., Carmosino, M., Atreya, S., Elliott, H., Halleaux, D., Renno, N., Wong, M., Pepin, R., Elliott, B., Spray, J., Thompson, L., Gordon, S., Ollila, A., Williams, J., Vasconcelos, P., Bentz, J., Nealson, K., Popa, R., Moersch, J., Tate, C., Day, M., Francis, R., McCullough, E., Cloutis, E., ten Kate, I.L., Scholes, D., Slavney, S., Stein, T., Ward, J., Berger, J., Moores, J.E., 2014. A Habitable Fluvio-Lacustrine Environment at Yellowknife Bay, Gale Crater, Mars. Science 343, 1242777. doi:10.1126/science.1242777

Hamilton, V.E., Osterloo, M.M., McGrane, B.S., 2007. THEMIS Decorrelation Stretched Infrared Mosaics of Candidate 2009 Mars Science Laboratory Landing Sites: Evidence for Significant Spectral Diversity. Lunar and Planetary Science Conference 1725.

Hartmann, W.K., 2007. Martian cratering 9: Toward resolution of the controversy about small craters. Icarus 189, 274–278. doi:10.1016/j.icarus.2007.02.011

Hartmann, W.K., 2005. Martian cratering 8: Isochron refinement and the chronology of Mars. Icarus 174, 294–320. doi:10.1016/j.icarus.2004.11.023

Hartmann, W.K., 1966. Early Lunar Cratering. Icarus 5, 406–418.

Hartmann, W.K., Neukum, G., 2001. Cratering chronology and the evolution of Mars. Space Science Reviews 96, 165–194.

Haughton, P., Davis, C., McCaffrey, W., Barker, S., 2009. Hybrid sediment gravity flow deposits – Classification, origin and significance. Marine and Petroleum Geology 26, 1900–1918. doi:10.1016/j.marpetgeo.2009.02.012

Hobbs, S.W., Paull, D.J., Bourke, M.C., 2010. Aeolian processes and dune morphology in Gale Crater. Icarus 210, 102–115. doi:10.1016/j.icarus.2010.06.006

Hon, K., Kauahikaua, J., Denlinger, R., Mackay, K., 1994a. Emplacement and inflation of pahoehoe sheet flows: Observations and measurements of active lava flows on Kilauea Volcano, Hawaii. Geological Society of America Bulletin 106, 351–370.

Hunter, R.E., 1977. Basic types of stratification in small eolian dunes. Sedimentology 24, 361–387.

Irwin, R.P., Howard, A.D., Craddock, R.A., Moore, J.M., 2005. An intense terminal epoch of widespread fluvial activity on early Mars: 2. Increased runoff and paleolake development. Journal of Geophysical Research 110. doi:10.1029/2005JE002460

Kite, E.S., Lewis, K.W., Lamb, M.P., Newman, C.E., Richardson, M.I., 2013. Growth and form of the mound in Gale Crater, Mars: Slope wind enhanced erosion and transport. Geology 41, 543–546. doi:10.1130/G33909.1

Kocurek, G., 1981. Significance of interdune deposits and bounding surfaces in aeolian dune sands. Sedimentology 28, 753–780.

Le Mouélic, S., Gasnault, O., Herkenhoff, K.E., Bridges, N.T., Langevin, Y., Mangold, N., Maurice, S., Wiens, R.C., Pinet, P., Newsom, H.E., Deen, R.G., Bell, J.F., Johnson, J.R., Rapin, W., Barraclough, B., Blaney, D.L., Deflores, L., Maki, J., Malin, M.C., Pérez, R., Saccoccio, M., 2014. The ChemCam Remote Micro-Imager at Gale crater: Review of the first year of operations on Mars. Icarus. doi:10.1016/j.icarus.2014.05.030

Malin, M.C., 1976. Nature and Origin of Intercrater Plains on Mars. California Institute of Technology, Pasadena, CA.

Malin, M.C., Bell, J.F., Cantor, B.A., Caplinger, M.A., Calvin, W.M., Clancy, R.T., Edgett, K.S., Edwards, L., Haberle, R.M., James, P.B., Lee, S.W., Ravine, M.A., Thomas, P.C., Wolff, M.J., 2007. Context Camera Investigation on board the Mars Reconnaissance Orbiter. Journal of Geophysical Research 112. doi:10.1029/2006JE002808

Malin, M.C., Edgett, K.S., 2000. Sedimentary Rocks of Early Mars. Science 290, 1927–1937. doi:10.1126/science.290.5498.1927

Malin, M.C., Edgett, K.S., Posiolova, L.V., McColley, S.M., Noe Dobrea, E.Z., 2006. Present-Day Impact Cratering Rate and Contemporary Gully Activity on Mars. Science 314, 1573–1577. doi:10.1126/science.1135156

McEwen, A., Preblich, B., Turtle, E., Artemieva, N., Golombek, M., Hurst, M., Kirk, R., Burr, D., Christensen, P., 2005. The rayed crater Zunil and interpretations of small impact craters on Mars. Icarus 176, 351–381. doi:10.1016/j.icarus.2005.02.009

McEwen, A.S., Bierhaus, E.B., 2006. The Importance of secondary cratering to age constraints on planetary surfaces. Annual Review of Earth and Planetary Sciences 34, 535–567.

McEwen, A.S., Eliason, E.M., Bergstrom, J.W., Bridges, N.T., Hansen, C.J., Delamere, W.A., Grant, J.A., Gulick, V.C., Herkenhoff, K.E., Keszthelyi, L., Kirk, R.L., Mellon, M.T., Squyres, S.W., Thomas, N., Weitz, C.M., 2007. Mars Reconnaissance Orbiter's High Resolution Imaging Science Experiment (HiRISE). Journal of Geophysical Research 112. doi:10.1029/2005JE002605

Michael, G.G., Neukum, G., 2010. Planetary surface dating from crater size–frequency distribution measurements: Partial resurfacing events and statistical age uncertainty. Earth and Planetary Science Letters 294, 223–229. doi:10.1016/j.epsl.2009.12.041

Michel, P., Morbidelli, A., 2013. Population of impactors and the impact cratering rate in the inner Solar System, in: Osinski, G.R., Pierazzo, E. (Eds.), Impact Cratering: Processes and Products. Wiley-Blackwell, Oxford, UK, pp. 21–31.

Milliken, R.E., Edgett, K.S., Swayze, G., Clark, R.N., Thomson, B.J., Anderson, R., Bell, J.F., 2009. Clay and Sulfate-Bearing Rocks in a Stratigraphic Sequence in Gale Crater. Presented at the Lunar and Planetary Science Conference.

Milliken, R.E., Grotzinger, J.P., Thomson, B.J., 2010. Paleoclimate of Mars as captured by the stratigraphic record in Gale Crater. Geophysical Research Letters 37. doi:10.1029/2009GL041870

Minitti, M.E., Kah, L.C., Yingst, R.A., Edgett, K.S., Anderson, R.C., Beegle, L.W., Carsten, J.L., Deen, R.G., Goetz, W., Hardgrove, C., Harker, D.E., Herkenhoff, K.E., Hurowitz, J.A., Jandura, L., Kennedy, M.R., Kocurek, G., Krezoski, G.M., Kuhn, S.R., Limonadi, D., Lipkaman, L., Madsen, M.B., Olson, T.S., Robinson, M.L., Rowland, S.K., Rubin, D.M., Seybold, C., Schieber, J., Schmidt, M., Sumner, D.Y., Tompkins, V.V., Van Beek, J.K., Van Beek, T., 2013. MAHLI at the Rocknest sand shadow: Science and science-enabling activities: MAHLI AT ROCKNEST. Journal of Geophysical Research: Planets 118, 2338–2360. doi:10.1002/2013JE004426

Moore, J.M., Howard, A.D., 2005. Large alluvial fans on Mars. Journal of Geophysical Research 110. doi:10.1029/2004JE002352

Mortimer, E., Gupta, S., Cowie, P., 2005. Clinoform nucleation and growth in coarse-grained deltas, Loreto basin, Baja California Sur, Mexico: a response to episodic accelerations in fault displacement. Basin Research 17, 337–359. doi:10.1111/j.1365-2117.2005.00273.x

Mulder, T., Alexander, J., 2001. The physical character of subaqueous sedimentary density flows and their deposits. Sedimentology 48, 269–299.

Palucis, M.C., Dietrich, W.E., Hayes, A.G., Williams, R.M.E., Gupta, S., Mangold, N., Newsom, H., Hardgrove, C., Calef, F., Sumner, D.Y., 2014. The origin and evolution of the Peace Vallis fan system that drains to the *Curiosity* landing area, Gale Crater, Mars. Journal of Geophysical Research: Planets 119, 705–728. doi:10.1002/2013JE004583

Pelkey, S.M., Jakosky, B.M., 2002. Surficial Geologic Surveys of Gale Crater and Melas Chasma, Mars: Integration of Remote-Sensing Data. Icarus 160, 228–257. doi:10.1006/icar.2002.6978

Rice, M.S., Bell, J.F., Cloutis, E.A., Wang, A., Ruff, S.W., Craig, M.A., Bailey, D.T., Johnson, J.R., de Souza Jr., P.A., Farrand, W.H., 2010. Silica-rich deposits and hydrated minerals at Gusev Crater, Mars: Vis-NIR spectral characterization and regional mapping. Icarus 205, 375–395. doi:10.1016/j.icarus.2009.03.035

Rice, M.S., Williams, J.M., Calef, F., Anderson, R.B., Edgar, L., Stack, K., Sumner, D.Y., Newsom, H.E., Grotzinger, J.P., King, P., 2013. Detailed Geologic Mapping Along the Mars Science Laboratory (MSL) Curiosity Traverse Path from Glenelg to Mount Sharp. Presented at the Lunar and Planetary Science Conference.

Rogers, A.D., Bandfield, J.L., 2009. Mineralogical characterization of Mars Science Laboratory candidate landing sites from THEMIS and TES data. Icarus 203, 437–453. doi:10.1016/j.icarus.2009.04.020

Saunders, R.S., Arvidson, R.E., Badhwar, G.D., Boynton, W.V., Christensen, P.R., Cucinotta, F.A., Feldman, W.C., Gibbs, R.G., Kloss Jr, C., Landano, M.R., Mase, R.A., Mcsmith, G.W., Meyer, M.A., Mitrofanov, I.G., Pace, G.D., Plaut, J.J., Sidney, W.P., Spencer, D.A., Thompson, T.W., Zeitlin, C.J., 2004. 2001 Mars Odyssey mission summary. Space Science Reviews 110, 1–36.

Scott, D.H., Carr, M.H., 1978. Geologic Map of Mars. IMAP.

Scott, D.H., Morris, E.C., West, M.N., 1978. Geologic Map of the Aeolis quadrangle of Mars.

Self, S., Keszthelyi, L., Thordarson, T., 1998. The importance of pahoehoe. Annual Review of Earth and Planetary Sciences 26, 81–110.

Shanmugam, G., 1997. The Bouma Sequence and the turbidite mind set. Earth-Science Reviews 42, 201–229.

Sharp, R.P., Malin, M.C., 1975. Channels on Mars. Geological Society of America Bulletin 86, 593–609. doi:10.1130/0016-7606(1975)86<593:COM>2.0.CO;2

Siebach, K.L., Grotzinger, J.P., Kah, L.C., Stack, K.M., Malin, M., Léveillé, R., Sumner, D.Y., 2014. Subaqueous shrinkage cracks in the Sheepbed mudstone: Implications for early fluid diagenesis, Gale crater, Mars. Journal of Geophysical Research: Planets 119, 1597–1613. doi:10.1002/2014JE004623

Silvestro, S., Vaz, D.A., Ewing, R.C., Rossi, A.P., Fenton, L.K., Michaels, T.I., Flahaut, J., Geissler, P.E., 2013. Pervasive aeolian activity along rover Curiosity's traverse in Gale Crater, Mars. Geology 41, 483–486. doi:10.1130/G34162.1

Smith, D.E., Zuber, M.T., Soloman, S.C., Phillips, R.J., Head, J.W., Garvin, J.B., Banerdt, W.B., Muhleman, D.O., Pettengill, G.H., Neumann, G.A., Lemoine, F.G., Abshire, J.B., Aharonson, O., Brown, C.D., Hauck, S.A., Ivanov, A.B., McGovern, P.J., Zwally, H.J., Duxbury, T.C., 1999. The Global Topography of Mars and Implications for Surface Evolution. Science 284, 1495–1503. doi:10.1126/science.284.5419.1495

Soderblom, L.A., Bell, J.F., 2008. Exploration of the Martian surface: 1992-2007, in: Bell, J.F. (Ed.), The Martian Surface: Composition, Mineralogy and Physical Properties. Cambridge University Press, New York, pp. 3–19.

Stack, K.M., Grotzinger, J.P., Kah, L.C., Schmidt, M.E., Mangold, N., Edgett, K.S., Sumner, D.Y., Siebach, K.L., Nachon, M., Lee, R., Blaney, D.L., Deflores, L.P., Edgar, L.A., Fairén, A.G., Leshin, L.A., Maurice, S., Oehler, D.Z., Rice, M.S., Wiens, R.C., 2014. Diagenetic origin of nodules in the Sheepbed member, Yellowknife Bay formation, Gale crater, Mars. Journal of Geophysical Research: Planets 119, 1637–1664. doi:10.1002/2014JE004617

Sumner, D.Y., Palucis, M., Dietrich, W.E., Calef, F., Stack, K.M., Ehlmann, B., Bridges, J., Dromart, G., Eigenbrode, J., Farmer, J., Grant, J., Grotzinger, J., Hamilton, V., Hardgrove, C., Kah, L., Leveille, R., Mangold, N., Rowland, S., Williams, R., MSL Science Team, 2013. Preliminary Geological Map of the Peace Vallis Fan Integrated with In Situ Mosaics From the Curiosity Rover, Gale Crater, Mars. Presented at the Lunar and Planetary Science Conference.

Tanaka, K.L., 1986. The Stratigraphy of Mars. Proceedings of the 17th Lunar and Planetary Science Conference, Journal of Geophysical Research 91, 139–158.

Thomson, B.J., Bridges, N.T., Milliken, R., Baldridge, A., Hook, S.J., Crowley, J.K., Marion, G.M., de Souza Filho, C.R., Brown, A.J., Weitz, C.M., 2011. Constraints on the origin and evolution of the layered mound in Gale Crater, Mars using Mars Reconnaissance Orbiter data. Icarus 214, 413–432. doi:10.1016/j.icarus.2011.05.002

Vasavada, A.R., Grotzinger, J.P., Arvidson, R.E., Calef, F.J., Crisp, J.A., Gupta, S., Hurowitz, J., Mangold, N., Maurice, S., Schmidt, M.E., Wiens, R.C., Williams, R.M.E., Yingst, R.A., 2014. Overview of the Mars Science Laboratory mission: Bradbury Landing to Yellowknife Bay and beyond. Journal of Geophysical Research: Planets 119, 1134–1161. doi:10.1002/2014JE004622

Wiens, R.C., Maurice, S., Barraclough, B., Saccoccio, M., Barkley, W.C., Bell, J.F., Bender, S., Bernardin, J., Blaney, D., Blank, J., Bouyé, M., Bridges, N., Bultman, N., Caïs, P., Clanton, R.C., Clark, B., Clegg, S., Cousin, A., Cremers, D., Cros, A., DeFlores, L.,

Delapp, D., Dingler, R., D'Uston, C., Darby Dyar, M., Elliott, T., Enemark, D., Fabre, C., Flores, M., Forni, O., Gasnault, O., Hale, T., Hays, C., Herkenhoff, K., Kan, E., Kirkland, L., Kouach, D., Landis, D., Langevin, Y., Lanza, N., LaRocca, F., Lasue, J., Latino, J., Limonadi, D., Lindensmith, C., Little, C., Mangold, N., Manhes, G., Mauchien, P., McKay, C., Miller, E., Mooney, J., Morris, R.V., Morrison, L., Nelson, T., Newsom, H., Ollila, A., Ott, M., Pares, L., Perez, R., Poitrasson, F., Provost, C., Reiter, J.W., Roberts, T., Romero, F., Sautter, V., Salazar, S., Simmonds, J.J., Stiglich, R., Storms, S., Striebig, N., Thocaven, J.-J., Trujillo, T., Ulibarri, M., Vaniman, D., Warner, N., Waterbury, R., Whitaker, R., Witt, J., Wong-Swanson, B., 2012. The ChemCam Instrument Suite on the Mars Science Laboratory (MSL) Rover: Body Unit and Combined System Tests. Space Science Reviews 170, 167–227. doi:10.1007/s11214-012-9902-4

Williams, R.M.E., Grotzinger, J.P., Dietrich, W.E., Gupta, S., Sumner, D.Y., Wiens, R.C., Mangold, N., Malin, M.C., Edgett, K.S., Maurice, S., Forni, O., Gasnault, O., Ollila, A., Newsom, H.E., Dromart, G., Palucis, M.C., Yingst, R.A., Anderson, R.B., Herkenhoff, K.E., Le Mouelic, S., Goetz, W., Madsen, M.B., Koefoed, A., Jensen, J.K., Bridges, J.C., Schwenzer, S.P., Lewis, K.W., Stack, K.M., Rubin, D., Kah, L.C., Bell, J.F., Farmer, J.D., Sullivan, R., Van Beek, T., Blaney, D.L., Pariser, O., Deen, R.G., MSL Science Team, Kemppinen, O., Bridges, N., Johnson, J.R., Minitti, M., Cremers, D., Edgar, L., Godber, A., Wadhwa, M., Wellington, D., McEwan, I., Newman, C., Richardson, M., Charpentier, A., Peret, L., King, P., Blank, J., Weigle, G., Schmidt, M., Li, S., Milliken, R., Robertson, K., Sun, V., Baker, M., Edwards, C., Ehlmann, B., Farley, K., Griffes, J., Miller, H., Newcombe, M., Pilorget, C., Rice, M., Siebach, K., Stolper, E., Brunet, C., Hipkin, V., Leveille, R., Marchand, G., Sobron Sanchez, P., Favot, L., Cody, G., Steele, A., Fluckiger, L., Lees, D., Nefian, A., Martin, M., Gailhanou, M., Westall, F., Israel, G., Agard, C., Baroukh, J., Donny, C., Gaboriaud, A., Guillemot, P., Lafaille, V., Lorigny, E., Paillet, A., Perez, R., Saccoccio, M., Yana, C., Aparicio, C.A., Caride Rodriguez, J., Carrasco Blazquez, I., Gomez Gomez, F., Elvira, J.G., Hettrich, S., Lepinette Malvitte, A., Marin Jimenez, M., Frias, J.M., Soler, J.M., Torres, F.J.M., Molina Jurado, A., Sotomayor, L.M., Munoz Caro, G., Navarro Lopez, S., Gonzalez, V.P., Garcia, J.P., Rodriguez Manfredi, J.A., Planello, J.J.R., Alejandra Sans Fuentes, S., Sebastian Martinez, E., Torres Redondo, J., O'Callaghan, R.U., Zorzano Mier, M.-P., Chipera, S., Lacour, J.-L., Mauchien, P., Sirven, J.-B., Manning, H., Fairen, A., Hayes, A., Joseph, J., Squyres, S., Thomas, P., Dupont, A., Lundberg, A., Melikechi, N., Mezzacappa, A., DeMarines, J., Grinspoon, D., Reitz, G., Prats, B., Atlaskin, E., Genzer, M., Harri, A.-M., Haukka, H., Kahanpaa, H., Kauhanen, J., Paton, M., Polkko, J., Schmidt, W., Siili, T., Fabre, C., Wray, J., Wilhelm, M.B., Poitrasson, F., Patel, K., Gorevan, S., Indyk, S., Paulsen, G., Bish, D., Schieber, J., Gondet, B., Langevin, Y., Geffroy, C., Baratoux, D., Berger, G., Cros, A., Uston, C. d., Lasue, J., Lee, Q.-M., Meslin, P.-Y., Pallier, E., Parot, Y., Pinet, P., Schroder, S., Toplis, M., Lewin, E., Brunner, W., Heydari, E., Achilles, C., Oehler, D., Sutter, B., Cabane, M., Coscia, D., Szopa, C., Robert, F., Sautter, V., Nachon, M., Buch, A., Stalport, F., Coll, P., Francois, P., Raulin, F., Teinturier, S., Cameron, J., Clegg, S., Cousin, A., DeLapp, D., Dingler, R., Jackson, R.S., Johnstone, S., Lanza, N., Little, C., Nelson, T., Williams, R.B., Jones, A., Kirkland, L., Treiman, A., Baker, B., Cantor, B., Caplinger, M., Davis, S., Duston, B., Fay, D., Hardgrove, C., Harker, D., Herrera, P., Jensen, E., Kennedy, M.R., Krezoski, G., Krysak, D., Lipkaman, L.,

McCartney, E., McNair, S., Nixon, B., Posiolova, L., Ravine, M., Salamon, A., Saper, L., Stoiber, K., Supulver, K., Van Beek, J., Zimdar, R., French, K.L., Iagnemma, K., Miller, K., Summons, R., Goesmann, F., Hviid, S., Johnson, M., Lefavor, M., Lyness, E., Breves, E., Dyar, M.D., Fassett, C., Blake, D.F., Bristow, T., DesMarais, D., Edwards, L., Haberle, R., Hoehler, T., Hollingsworth, J., Kahre, M., Keely, L., McKay, C., Bleacher, L., Brinckerhoff, W., Choi, D., Conrad, P., Dworkin, J.P., Eigenbrode, J., Floyd, M., Freissinet, C., Garvin, J., Glavin, D., Harpold, D., Mahaffy, P., Martin, D.K., McAdam, A., Pavlov, A., Raaen, E., Smith, M.D., Stern, J., Tan, F., Trainer, M., Meyer, M., Posner, A., Voytek, M., Anderson, R.C., Aubrey, A., Beegle, L.W., Behar, A., Brinza, D., Calef, F., Christensen, L., Crisp, J.A., DeFlores, L., Feldman, J., Feldman, S., Flesch, G., Hurowitz, J., Jun, I., Keymeulen, D., Maki, J., Mischna, M., Morookian, J.M., Parker, T., Pavri, B., Schoppers, M., Sengstacken, A., Simmonds, J.J., Spanovich, N., de la Torre Juarez, M., Vasavada, A.R., Webster, C.R., Yen, A., Archer, P.D., Cucinotta, F., Jones, J.H., Ming, D., Morris, R.V., Niles, P., Rampe, E., Nolan, T., Fisk, M., Radziemski, L., Barraclough, B., Bender, S., Berman, D., Dobrea, E.N., Tokar, R., Vaniman, D., Leshin, L., Cleghorn, T., Huntress, W., Manhes, G., Hudgins, J., Olson, T., Stewart, N., Sarrazin, P., Grant, J., Vicenzi, E., Wilson, S.A., Bullock, M., Ehresmann, B., Hamilton, V., Hassler, D., Peterson, J., Rafkin, S., Zeitlin, C., Fedosov, F., Golovin, D., Karpushkina, N., Kozyrev, A., Litvak, M., Malakhov, A., Mitrofanov, I., Mokrousov, M., Nikiforov, S., Prokhorov, V., Sanin, A., Tretyakov, V., Varenikov, A., Vostrukhin, A., Kuzmin, R., Clark, B., Wolff, M., McLennan, S., Botta, O., Drake, D., Bean, K., Lemmon, M., Lee, E.M., Sucharski, R., Hernandez, M.A. d. P., Blanco Avalos, J.J., Ramos, M., Kim, M.-H., Malespin, C., Plante, I., Muller, J.-P., Gonzalez, R.N., Ewing, R., Boynton, W., Downs, R., Fitzgibbon, M., Harshman, K., Morrison, S., Kortmann, O., Williams, A., Lugmair, G., Wilson, M.A., Jakosky, B., Zunic, T.B., Frydenvang, J., Kinch, K., Stipp, S.L.S., Boyd, N., Campbell, J.L., Gellert, R., Perrett, G., Pradler, I., VanBommel, S., Jacob, S., Owen, T., Rowland, S., Savijarvi, H., Boehm, E., Bottcher, S., Burmeister, S., Guo, J., Kohler, J., Garcia, C.M., Mellin, R.M., Schweingruber, R.W., McConnochie, T., Benna, M., Franz, H., Bower, H., Brunner, A., Blau, H., Boucher, T., Carmosino, M., Atreya, S., Elliott, H., Halleaux, D., Renno, N., Wong, M., Pepin, R., Elliott, B., Spray, J., Thompson, L., Gordon, S., Williams, J., Vasconcelos, P., Bentz, J., Nealson, K., Popa, R., Moersch, J., Tate, C., Day, M., Kocurek, G., Hallet, B., Sletten, R., Francis, R., McCullough, E., Cloutis, E., ten Kate, I.L., Arvidson, R., Fraeman, A., Scholes, D., Slavney, S., Stein, T., Ward, J., Berger, J., Moores, J.E., 2013. Martian Fluvial Conglomerates at Gale Crater. Science 340, 1068–1072. doi:10.1126/science.1237317

Wood, L.J., 2006. Quantitative geomorphology of the Mars Eberswalde delta. Geological Society of America Bulletin 118, 557–566. doi:10.1130/B25822.1

Zurek, R.W., Smrekar, S.E., 2007. An overview of the Mars Reconnaissance Orbiter (MRO) science mission. Journal of Geophysical Research 112. doi:10.1029/2006JE002701